

Copyright  
by  
Brady Leigh Stoll  
2015

The Dissertation Committee for Brady Leigh Stoll  
certifies that this is the approved version of the following dissertation:

**Coupling photovoltaics and grid-scale energy storage:  
performance and sitability**

Committee:

---

Mark Deinert, Supervisor

---

Ross Baldick

---

Thomas Edgar

---

John Howell

---

Li Shi

---

Michael Webber

**Coupling photovoltaics and grid-scale energy storage:  
performance and sitability**

by

**Brady Leigh Stoll, B.A., B.S.Phy., M.S.E.**

**DISSERTATION**

Presented to the Faculty of the Graduate School of  
The University of Texas at Austin  
in Partial Fulfillment  
of the Requirements  
for the Degree of

**DOCTOR OF PHILOSOPHY**

The University of Texas at Austin

May 2015

I would like to dedicate my dissertation to both my family and to those who are practically family to me. My family has been incredibly supportive of me both in undergrad and grad school. I am so appreciative of my parents and siblings for listening to me talk through ideas and feelings, as well as providing food and entertainment for much needed distractions. I will miss you all in Colorado, but hope you come visit me often. Blobby, my almost-family, has helped me through grad school in so many ways. I appreciate the life advice, random discussions, and the knowledge that you all are there for me and for each other for anything. I am grateful for your relationships and the past 9 years.

## Acknowledgments

I would like to thank my advisor, Mark Deinert, for his guidance and support in this work. He has provided me with an incredible amount of feedback and advice in regards to not only the research process and the work done, but also on how to be a better scientist. I appreciate the time and effort that you have put in to teaching me how to present, how to write, and how to research to the highest degree.

I would also like to thank Dr. Ross Baldick, Dr. Thomas Edgar, Dr. John Howell, Dr. Li Shi and Dr. Michael Webber. From providing mentorship and guidance in my research questions to teaching me the basic subjects of mechanical engineering in core classes, these professors have each provided me with valuable guidance throughout my graduate education. I am extremely grateful for both your feedback and your guidance.

I would like to particularly thank those who have directly helped me with my research, Dr. Andrew Osborne, Dr. Geoffrey Recktenwald, David Harding and Timothy Smith. You have each taught me so many things about research and coding. I am grateful for all of the time and effort you have invested in me and my research.

The Women in Mechanical Engineering group as well as the staff of the Women in Engineering Program office have provided so much support outside of research my entire tenure in grad school. I appreciate all of the work that you do, as well as all of the friendships I have established through these groups.

Finally, I would like to thank my family and for all of their support and love for me. I would also like to thank my boyfriend Peter for his faith in me and all of the encouragement.

# Coupling photovoltaics and grid-scale energy storage: performance and sitability

Brady Leigh Stoll, Ph.D.  
The University of Texas at Austin, 2015

Supervisor: Mark Deinert

The Fifth Assessment of the International Panel on Climate Change has called for a four fold increase in the use of low-carbon sources of electricity to help stabilize climate change by mid century. Many people look to solar power systems to help reduce carbon intensity, but cost and variability have been significant obstacles to their widespread deployment. However, the cost of photovoltaics has dropped significantly in recent years, and grid-scale energy storage technologies are available to allow for production of dispatchable electricity from photovoltaics. In particular, compressed-air energy storage is both low-cost and can be built in a wide variety of geologies as well as above ground. I show that coupling large-scale photovoltaic arrays and grid-scale storage allows for dispatchable electricity production at costs that are comparable to other low carbon electricity sources. I examine four load curves: base-load generation, on-peak generation, and averaged load curves for the Electric Reliability Council of Texas (ERCOT) and PJM Independent System Operators. I found that on-peak and ERCOT loads typically required the lowest amount of storage, up to 2000  $MWh_e$  less than that for base-load generation. However, in some regions, and for some storage amounts, baseload output actually provided the lowest cost of electricity. I also show that such coupled systems could provide base-load electricity for  $\leq 0.08/kWh_e$

on more than 40% of global land surface, with a capacity factor equivalent to that of the US nuclear fleet. Importantly, this is below the projected cost of electricity from new nuclear power systems. While cost is a major factor, also of importance is where systems of photovoltaics and grid-scale storage would provide the most benefit. Locations expected to provide energy at the lowest cost do not necessarily correspond to load and population centers, where the electricity is most needed. I use multi-criteria decision analysis techniques to perform a global study of the optimal locations for siting these coupled systems to maximize their social benefit. I found that the most ideal locations are generally located in Africa, Iraq, and southeast Asia, as these locations have both high irradiance levels as well as expanding populations and low grid connectivity.

# Table of Contents

<b>Acknowledgments</b>	<b>v</b>
<b>Abstract</b>	<b>vi</b>
<b>List of Tables</b>	<b>xi</b>
<b>List of Figures</b>	<b>xii</b>
<b>Chapter 1. Introduction</b>	<b>1</b>
1.1 Motivation . . . . .	1
1.2 Renewable Energy . . . . .	4
1.2.1 Capacity Growth . . . . .	6
1.2.2 Policy . . . . .	7
1.2.2.1 Policy Measures . . . . .	7
1.2.2.2 Policy of selected countries . . . . .	9
1.2.3 Grid Integration . . . . .	13
1.3 Photovoltaic Market . . . . .	14
1.3.1 Historical Costs . . . . .	15
1.3.2 Learning Curves . . . . .	16
1.4 Grid-scale Storage . . . . .	18
1.4.1 Pumped Hydro Storage . . . . .	19
1.4.2 Compressed Air Energy Storage . . . . .	20
1.4.3 Batteries . . . . .	23
<b>Chapter 2. Irradiance Calculation</b>	<b>25</b>
2.1 Algorithm . . . . .	25
2.2 ISCCP Data . . . . .	26
2.3 Comparison to Ground-based Data . . . . .	31
2.3.1 Biowatt II . . . . .	32
2.3.2 MLML . . . . .	33
2.3.3 FIRE/SRB . . . . .	35
2.3.4 BSRN . . . . .	40



2.4	Comparison of Transmission Formulation . . . . .	50
2.4.1	Single value, 0.6 $\mu\text{m}$ . . . . .	51
2.4.2	Integration over Wavelength . . . . .	52
2.5	Visibility Correction . . . . .	54
2.5.1	Biowatt II . . . . .	55
2.5.2	MLML . . . . .	56
2.5.3	FIRE/SRB . . . . .	58
2.5.4	BSRN . . . . .	60
<b>Chapter 3. Coupling photovoltaics and grid-scale energy storage</b>		<b>64</b>
3.1	Base-load Energy flow model . . . . .	64
3.2	Levelized Cost of Electricity . . . . .	72
3.2.1	Cost Model . . . . .	72
3.2.1.1	Battery Costs . . . . .	76
3.2.1.2	CAES Geology . . . . .	77
3.2.1.3	Array Construction Time . . . . .	77
3.2.1.4	Natural Gas Prices . . . . .	79
3.2.2	Life-cycle Electricity Cost . . . . .	80
3.2.2.1	Cost Comparison . . . . .	84
3.2.3	Variance in the levelized cost of electricity. . . . .	85
3.2.4	Sensitivity Analysis . . . . .	88
3.3	Carbon intensity of the coupled system. . . . .	90
3.4	Global Analysis . . . . .	92
3.4.1	Feasible land fraction . . . . .	92
3.4.2	Population with access to feasible land . . . . .	95
3.5	Excess Energy . . . . .	98
<b>Chapter 4. Load Following with Photovoltaics</b>		<b>105</b>
4.1	Load Data . . . . .	107
4.2	Methods . . . . .	111
4.3	Results . . . . .	113
<b>Chapter 5. GIS Multi-criteria Decision Analysis</b>		<b>117</b>
5.1	Background . . . . .	118
5.2	Methods . . . . .	120
5.3	Data Description . . . . .	122
5.3.1	Geology . . . . .	122

5.3.2	Land Slope . . . . .	124
5.3.3	Population Density . . . . .	125
5.3.4	Wetland Areas and Flood Plains . . . . .	125
5.3.5	Population . . . . .	126
5.3.6	Growth in Electricity Consumption . . . . .	127
5.3.7	Access to Electricity . . . . .	129
5.3.8	Cost of Electricity . . . . .	130
5.4	Multi-Criteria Decision Analysis . . . . .	131
<b>Chapter 6. Conclusions</b>		<b>135</b>
6.1	Conclusions from Irradiance Calculations . . . . .	135
6.2	Conclusions from PV-CAES Model . . . . .	136
6.3	Conclusions from Load Following Model . . . . .	137
6.4	Conclusions from GIS Analysis . . . . .	137
6.5	Suggestions for future work . . . . .	138
<b>Bibliography</b>		<b>139</b>
<b>Vita</b>		<b>161</b>

# List of Tables

1.1	CO <sub>2</sub> equivalent emissions from various energy technologies . . . . .	5
1.2	Learning Rates for various technologies. . . . .	18
2.1	Coefficients used in Eq. (2.2) . . . . .	26
2.2	Biowatt Statistics . . . . .	33
2.3	MLML Statistics . . . . .	34
2.4	FIRE/SRB locations . . . . .	36
2.5	FIRE/SRB locations . . . . .	39
2.6	FIRE/SRB pixel correlation . . . . .	40
2.7	BSRB locations . . . . .	42
2.8	BSRB Correlations . . . . .	46
2.9	Biowatt Visibility Comparison . . . . .	56
2.10	MLML Visibility Comparison . . . . .	57
2.11	BSRB Correlations, including visibility . . . . .	62
3.1	Discount Model Inputs, PV. . . . .	75
3.2	Discount Model Inputs, CAES. . . . .	75
3.3	Discount Model Inputs, Battery. . . . .	76
3.4	Utility Scale photovoltaic array construction times. . . . .	78
3.5	Land Fraction with energy cost < \$0.08/kWh <sub>e</sub> . . . . .	95
3.6	Population Fraction with energy cost < \$0.08/kWh <sub>e</sub> . . . . .	98
5.1	MCDA Criteria . . . . .	121

## List of Figures

1.1	Total worldwide installed capacity of photovoltaics . . . . .	6
1.2	Price of photovoltaic modules, by year . . . . .	16
1.3	Price of photovoltaic modules, by installed capacity . . . . .	17
1.4	CAES facility . . . . .	21
2.1	Surface Solar Irradiance Diagram . . . . .	27
2.2	Example Irradiance Data. . . . .	30
2.3	Example Irradiance Data. . . . .	31
2.4	Comparison of ISCCP with BioWATT datasets . . . . .	32
2.5	Correlation between ISCCP and BioWATT datasets . . . . .	33
2.6	Comparison of ISCCP with MLML datasets . . . . .	34
2.7	Correlation between ISCCP and MLML datasets . . . . .	35
2.8	FIRE/SRB site locations . . . . .	36
2.9	Comparison of ISCCP with FIRE/SRB datasets . . . . .	37
2.10	Correlation between ISCCP and FIRE/SRB datasets . . . . .	38
2.11	Map of the locations of each BSRN site. . . . .	41
2.12	24 hour average reconstructed irradiances -vs- ground level measurements. . . . .	44
2.13	672 hour average reconstructed irradiances -vs- ground level measurements. . . . .	45
2.14	Frequency distribution of difference between derived 24 hour average irradiances and surface measurements. . . . .	48
2.15	Frequency distribution of difference between derived 672 hour average irradiances and surface measurements. . . . .	49
2.16	Phase Function for several wavelengths . . . . .	51
2.17	Difference in Irradiance, $0.6 \mu m - 0.78 \mu m$ . . . . .	52
2.18	Solar Spectrum at Surface . . . . .	53
2.19	Difference in Irradiance, averaged over solar spectrum - $0.78 \mu m$ . . . . .	53
2.20	Surface Visibility. . . . .	55
2.21	Irradiance error comparison of visibility in Biowatt dataset . . . . .	57
2.22	Irradiance error comparison of visibility in MLML dataset . . . . .	58
2.23	Irradiance error comparison of visibility in FIRE/SRB dataset . . . . .	59
2.24	Correlation comparison of visibility, FIRE/SRB . . . . .	60

2.25	Irradiance error comparison, including visibility in BSRN dataset . . .	61
3.1	PV-Storage system diagram . . . . .	65
3.2	Global geology suitable for CAES. . . . .	71
3.3	Timing of cash flows. . . . .	73
3.4	Timing of cash flows, battery. . . . .	74
3.5	Geographical distribution of salt deposits. . . . .	77
3.6	Construction times for grid-scale photovoltaics. . . . .	79
3.7	Gas Prices by country. . . . .	80
3.8	Array Size, $MW_e$ . . . . .	81
3.9	Storage Capacity, $MWh_e$ . . . . .	82
3.10	Electricity cost with below-ground CAES, $$/kWh_e$ . . . . .	83
3.11	Electricity cost with above-ground CAES, $$/kWh_e$ . . . . .	83
3.12	Electricity cost with battery storage, $$/kWh_e$ . . . . .	84
3.13	Standard deviation of levelized electricity cost, below-ground CAES. .	87
3.14	Standard deviation of levelized electricity cost, above-ground CAES. .	87
3.15	Sensitivity of levelized cost to unit costs. . . . .	89
3.16	GHG Emissions . . . . .	91
3.17	Fraction of land with cost $< \$0.08/kWh_e$ . . . . .	93
3.18	Percentage of Land Area with Cost $< LCOE$ . . . . .	94
3.19	Population within areas with low-cost photovoltaic energy . . . . .	96
3.20	Percentage of global population with access to energy at a cost $< LCOE$	97
3.21	Ratio of excess energy . . . . .	99
3.22	Example Daily Prices. . . . .	101
3.23	Excess Revenue. . . . .	104
4.1	Typical Daily Load Curve. . . . .	106
4.2	Map of U.S. ISOs . . . . .	107
4.3	Variation in daily demand profile, by ISO . . . . .	108
4.4	Average Yearly Load, ERCOT and PJM . . . . .	109
4.5	Example Daily Load. . . . .	110
4.6	Lowest Cost Load Profile. . . . .	114
4.7	Storage Requirement, by Load Profile. . . . .	115
4.8	Carbon reduction for Load Following . . . . .	116
5.1	MCDA process overview. . . . .	122
5.2	Distribution of geology suitable for CAES. . . . .	123

5.3	Estimated land slope. . . . .	124
5.4	Global population density. . . . .	125
5.5	Global wetlands. . . . .	126
5.6	Population per pixel. . . . .	127
5.7	Estimated Growth in Electricity Consumption from 2012 to 2020 . . .	128
5.8	Access to Electricity . . . . .	129
5.9	Energy cost with below-ground CAES, $\$/kWh_e$ . . . . .	130
5.10	Number of Exclusions per Location . . . . .	131
5.11	MCDA Excluded Locations . . . . .	132
5.12	MCDA Excluded Locations, electricity access . . . . .	133

# Chapter 1

## Introduction

### 1.1 Motivation

Rising population and improving quality of life, particularly in developing countries and China, are contributing to a large growth in electricity usage [1]. Global electricity generation is expected to grow by 93% by the year 2040 to 39 trillion kWh<sub>e</sub> per year [1]. The electric power sector is currently the largest carbon producing sector, accounting for over 25% of global emissions [2,3]. As electricity production continues to rise, carbon emissions will increase if the current dominant technologies, coal and natural gas, continue to be used to a high degree [4]. The Intergovernmental Panel on Climate Change has called for a drastic increase in the use of low-carbon sources of electricity to help reduce carbon emissions and stabilize climate change by mid-century [2, 5].

While low-carbon technologies exist in the energy sector, [6–9], none of them are currently ideal. While nuclear power is capable of providing dependable, low-carbon base-load capacity [9, 10], its use evokes geopolitical concerns including storage of nuclear waste and proliferation of nuclear technologies [11]. Further, systems with carbon capture and storage are another option, but these technologies are predicted to be more expensive than nuclear power, and are still largely in development [5]. Solar and wind generation could satisfy the entire worlds electricity demand several times over [7], however, their cost and variability have traditionally posed significant obstacles to their widespread use [12, 13].

Photovoltaics are able to contribute to energy demand, especially in sunny locations with high afternoon energy demand [12–14]. Their use is becoming increasingly widespread in the industrialized world, and they are well suited to regions with little or no grid connectivity [15]. An increase in incentive programs has contributed to the drastic rise in photovoltaic installations, particularly in California [16] and Germany [17]. These incentive programs include feed in tariffs, direct subsidies or tax credits [18–21]. Many countries have also set renewable energy standards, some particularly for solar power [20–25]. Many developing countries are also looking to incorporate renewable energy policies in their future plans for electricity market development and growth [18, 26, 27]. As more policy initiatives are put in place to encourage clean energy installations and as costs of photovoltaic modules drop [28–30], an even further increase in photovoltaic installations can be expected [20].

As the amount of solar power on the electric grid increases, so do concerns about grid reliability [31–33]. Higher percentages of renewable sources, which can be highly volatile and difficult to predict, may potentially lead to grid stability issues or flexibility concerns for traditional generators [34–37]. Because of this, dispatchable energy provision from renewable sources would provide a premium for grid operators. Dispatchable energy would also provide a large benefit for developing countries, where electrification and lighting are known to increase the quality of life.

Large-scale energy storage systems would be one option for smoothing diurnal, seasonal, and weather-based fluctuations [13, 38–41]. Coupling photovoltaics to large-scale storage technologies could allow solar power to provide dependable, low-carbon, base-load electricity to the grid [42]. Pumped hydroelectric storage and compressed air energy storage have both been demonstrated at grid scale, and have been shown to be cost effective [40, 41, 43–45]. As such, they are prime candidates for coupling with



photovoltaics to provide base-load power [38, 46, 47]. In particular, compressed air energy storage has a high potential for world-wide use due to its siting flexibility [48, 49]. Batteries could also be used for grid-scale storage, however they are currently either not commercially feasible, or are very expensive [22, 38, 45, 50].

The ability of a storage facility to smooth variability in solar resources, and the storage capacity required, is highly dependent on the local solar resources. Locations with high seasonal variations, such as northern Europe, have different storage requirements than locations with high hourly variation, such as the equatorial tropics. In order to accurately model the ability of a coupled photovoltaic array and grid-scale storage facility to provide base-load electricity, it is necessary to understand the variability of solar irradiance itself. High-resolution satellite data can be used to do this, which is particularly useful for the analysis of solar resources in developing countries, where long histories of weather data collection are rare.

The International Satellite Cloud Climatology Project (ISCCP) provides an ideal data set with 25-years of satellite-based atmospheric data at a  $0.5^\circ \times 0.5^\circ$  spatial resolution and 3-hr temporal resolution [51–53]. I have processed these data using a critically evaluated algorithm to obtain surface solar irradiance measurements from July 1983 through June 2008 [54, 55]. The resulting global horizontal irradiances encompassed seasonal and diurnal variations, as well as the effects of clouds, surface reflection, ozone, and aerosols, providing unprecedented information about the solar resources available across the planet.

These data are then utilized to perform an analysis of the ability for locations across the planet to provide dispatchable solar energy when coupled to compressed air energy storage facilities. In addition I analyze the use of battery storage as costs are expected to drop and these technologies become more feasible. Understanding

the abilities and limitations of coupling solar power and storage facilities will be key as renewable energy is used to a higher degree worldwide. In addition, I present an analysis of the ideal locations to site these facilities such that they are optimally located in regions with low-cost, high population, and high need for energy generation.

## 1.2 Renewable Energy

Renewable energy technologies are growing rapidly in response to both price drops and governmental mandates on their installation. In particular, the International Panel on Climate Change (IPCC) has indicated that green-house gas emissions are a global challenge, likely leading to a changing climate with potentially dramatic consequences for humanity [2]. The IPCC recommends an increase in low-carbon resources to be used for power generation. Currently the most commonly used energy sources include coal and natural gas, followed by hydroelectric and nuclear power. Together, coal and natural gas made up 62.9% of global electricity production in 2012 [4]. Hydroelectric provided 16.2%, and nuclear 10.9% of global electricity in the same year. Oil provided 5% of electricity, as did the “other” energy category, which includes all renewables [4].

In addition to contributing to global warming, traditional fossil fuel energy sources also have negative environmental impacts such as air and water pollution, mining and the land-use impacts associated with it, as well as potential impacts from leaking pipelines and other transportation of fuel issues [3]. While green-house gas emissions are a large global focus, these impacts have strong local impacts which are also avoided with renewable energy use.

The combined emissions from coal and natural gas contribute significantly total global emissions. Petroleum based generators, while a smaller fraction of total

electricity production, also have a high emission rate. Table 1.1 lists greenhouse gas emissions and costs of several energy technologies, including both traditional and renewable sources. Carbon is the most common green-house gas, however emissions of methane, nitrous oxide, and particulate matter also have implications for both climate change and health. Emissions of these gases have been combined in the table based on their carbon equivalent emission rate for simplicity [9].

Energy Technology	Emissions ( $gCO_2eq/kWh_e$ )	Avg. Cost (\$/kWh)
Coal, present day	950-1250	0.078
Natural Gas	440-780	0.079
CCS		
Pulverized Coal	92-145	0.13
IGCC	65-152	0.12
Nuclear	2.8-24	0.099
Photovoltaic	43-73	0.16
Wind		
On-shore	8-30	0.084
Off-shore	9-19	0.17
Hydro	1-34	0.035
Compressed Air Energy Storage	19 ( $gCO_2eq/kWh_{e,storage}$ )	
Pumped Hydro Storage	36 ( $gCO_2eq/kWh_{e,storage}$ )	
Battery Storage	125-161 ( $gCO_2eq/kWh_{e,storage}$ )	

Table 1.1: Includes all lifecycle emissions, including upstream, downstream, and operation. All emissions values from review article [9], all cost values from [5]. The emissions from storage facilities are based on the storage capacity of the facilities.

In order to reduce the emissions from traditional sources, technologies such as carbon capture and sequestration (CCS) have been suggested as mitigation strategies [5, 56]. These technologies collect the carbon emitted from combustion of fossil fuels and store it in a location, such as an underground cavern or the deep ocean, so it does not reach the atmosphere [57, 58]. It has been estimated that CCS could reduce the emissions from energy production by 20% [57]. However, this technology is still in the demonstration phase and while costs are expected to drop, they remain high with a

wide band of uncertainty [58].

Renewable energy sources could provide an alternative low-carbon energy source. While these sources typically are not-dispatchable and are more expensive to build, their energy has no fuel costs and low operation and maintenance costs. Historically, high capital costs prevented these technologies from being installed in large quantities. However, photovoltaics also have seen a high increase in global installations, Fig. 1.1, as their costs have dropped and policies have been implemented to support their growth.

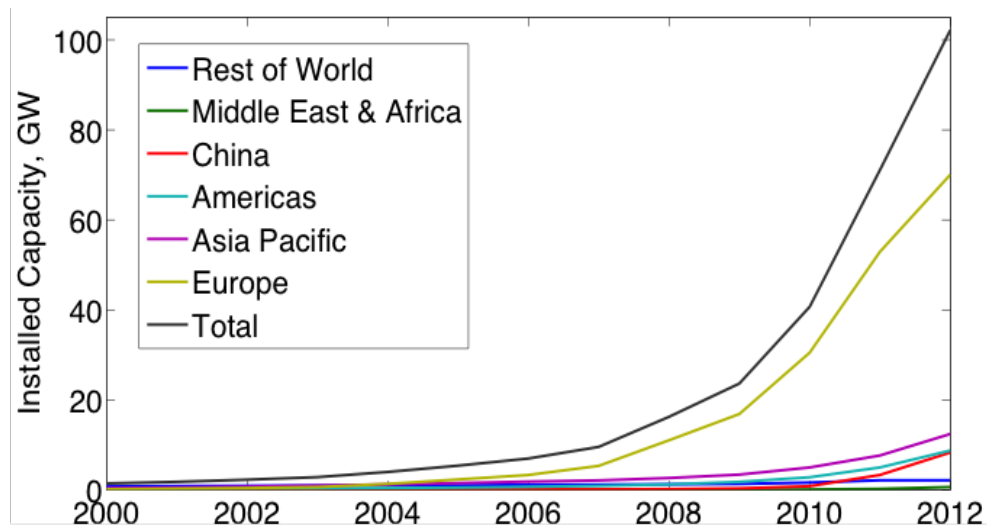


Figure 1.1: The photovoltaic industry has experienced rapid growth in recent years, particularly in Europe. Data from [15].

### 1.2.1 Capacity Growth

Solar energy has seen a high growth rate in the recent past, with the global installed capacity growing an average of nearly 55%/year annually between 2007 and 2013 [18]. In 2013 56% of all global power capacity installations came from renewable sources, with solar power exceeding the yearly installed capacity of wind power for the first time [18]. The cumulative installed capacity of photovoltaics across the globe

was 139 GW at the end of 2013, up from 100GW in 2012 [18].

At a country level, Germany has the highest installed capacity of photovoltaics, with nearly 36 GW [18]. It is followed by China, Italy, Japan and the United States for the top five countries with the most installed capacity as of 2013 [18]. China installed the most capacity of any country in 2013, with a total of 12.9 GW just in that year [18]. Also of note, Italy was able to meet 7.8% of electricity demand with solar power in 2013 [18].

In the manufacturing sector, China leads the world in most produced photovoltaic modules [59]. China produced two-thirds of all modules in 2013 [18]. Other Asian countries provided 20% of panels, European countries 9%, and the United States 2.6% [18]. While oversupply led to a brief drop in prices and market consolidation, the photovoltaic market began to pick up in 2013 [18].

## **1.2.2 Policy**

In order to encourage the expansion of renewable energy, particularly solar power, many governments world-wide have implemented policies or set specific goals to encourage constituents to install photovoltaics. The most common methods utilized are feed-in tariffs, renewable portfolio standards, direct subsidies, and tax credits [18–21,60]. Stable policies in support of solar energy have contributed globally to the rapid growth of photovoltaic installations in recent years [21,61,62].

### **1.2.2.1 Policy Measures**

Subsidies are one of the most widely utilized mechanism to support solar growth globally [61]. These policies include direct grants or rebates for installation costs or low-interest loans for particular technologies [21,61,62]. They have been effectively used in several states, notably California [16], and many countries, notably

Australia [62] and developing countries.

Feed in tariffs (FITs) have been very effective at increasing renewable energy installations currently in use [61, 63–65]. Feed-in tariffs most basically provide a form of payment for each kWh of electricity produced during a set time period. This provides a dependable revenue stream to help offset the high installation costs of solar power [18, 63]. Many countries world-wide, over 75 jurisdictions as of 2010, have utilized feed-in tariffs with a high degree of success [18, 19, 61, 63].

Many different implementations are possible, including flat rates, front-loaded rates to encourage initial growth, or market-driven measures. Whichever rate structure is utilized, a key factor for feed-in tariffs is stability and predictability of the program [63]. A downside of FITs is that they have the potential to support uneconomical technologies or pose a high cost to consumers if implemented poorly [60, 64]. Additionally, while the FIT provides a stable expected payout over the system lifetime, it does not affect the high up-front costs of installation, which can still be a barrier [61].

Net metering policies are similar to FITs in that they involve selling electricity by customers who have installed PV arrays, however they only account for the net difference in generation and consumption [60, 61]. These policies calculate the total difference in energy produced and consumed at the end of a billing cycle, and either pay the consumer or charge the consumer for the difference at a standard rate. Net-metering policies have been used by several states in the U.S. [66, 67], as well as in several countries [61], as a means to encourage renewable growth.

Renewable Portfolio Standards (RPSs) encourage renewable energy generation without directly subsidizing the energy or capacity. These policies require that a country, state, or other administrative unit produce or purchase at least a given percentage of electricity from renewable sources [3, 20, 61]. Similar policies are also

referred to as tradable green certificate (TGC) programs in Europe, which can be traded between entities to reach the required goal renewable generation [3,65]. These policies are more common in developed countries [61].

Some RPSs require specific technologies to provide a portion of the required fraction whereas others allow any within the “renewable energy” category to be counted. This has led to concerns that RPS policies disincentivize diversity of technologies in favor of the current lowest cost technologies [20]. In order to combat this, many states have implemented modified RPS policies to specifically require or incentivize higher cost technologies, such as solar power, to meet the RPS requirements [20]. Renewable portfolio standards are common at the state-level in the United States, but are also used by several countries including Italy and the United Kingdom [20,65,67].

Tax credits are a means by which a government can provide an incentive based on either installation costs or produced energy. One of the issues with tax credits is the lack of stability in these directives and ease with which the program amounts or time-lines can be changed on political whims [3]. They also can have a high impact on governmental income, potentially reducing the tax revenue for governments by hundreds of millions of dollars [61].

### **1.2.2.2 Policy of selected countries**

European countries have implemented a wide variety of policies to encourage renewable growth in general, as well as solar power specifically. These policies include feed in tariffs, tradable green certificates, subsidies, tax credits, as well as net metering [68]. The European Union collectively has implemented the Europe 2020 initiative, a set of five goals for the EU to reach by the year 2020, including to provide 20% of energy from renewable sources [25]. In addition to this EU wide goal, individual countries have utilized a wide variety of policies to encourage renewable

and specifically solar growth.

Germany has by far the most installed capacity of photovoltaics, with 36 GW [18]. By the end of 2007, the country generated 4% of electricity from photovoltaics [3], and 5% of electricity in 2013 [18]. Germany implemented a feed-in tariff in 1990 with the Electricity Feed Act which was later replaced with the Renewable Energy Sources Act [17,68]. These policies provided the framework for a stable market for solar power, which has been vastly effective [17,68]. The FITs used in Germany have a fixed duration of 20 years, providing stability for investors. There are different levels of FIT payments based on the size and type of a particular PV system [3,61]. In 2008, the FIT was amended to reduce the FIT rate in accordance with the reduction in photovoltaic prices seen [3,59]. Other policies utilized in Germany at by national or local governments include grants and tax incentives [3,59].

Spain also instituted feed-in tariffs under Royal Decrees in both 2004 and 2008 [21]. These policies initially targeted large scale solar power facilities and were later amended to improve incentives for rooftop PV [3]. A cap on the size of systems was introduced in 2007, leading to nearly 5 times as much capacity installed in 2008 than 2007 before this went into effect [21]. Subsequent Royal Decrees limited the amount of installed capacity each year under the feed-in tariff. This change reduced the growth Spain had seen in previous years [21].

France provided subsidies for photovoltaics beginning in the 1990's, and tax incentives in 2005 [21]. France later began a feed-in tariff in 2002, which was modified in 2006 and 2009 [3,21]. These policies lead to a total installed capacity of 2500 MW in 2011 [21].

In Asia, Japan and China are leaders in the photovoltaic industry. Japan has a long history of supporting solar power, beginning with research and development



support in the 1970's [21] and a residential subsidy program in 1994 to cover the cost of modules, equipment, and installation costs [24]. The Japanese government invested over 125 billion Yen in research and development between 1999 and 2002 to further develop photovoltaic technologies and to field test PV units [24]. Zhang et. al. [69] found that the regional subsidy policies in Japan had a significant impact on PV system diffusion. In 2004, Japan developed the PV Roadmap Towards 2030 (PV2030) with a goal of improving the efficiency of solar panels as well as lowering their cost [23]. More recently, the Ministry of Economy, Trade and Industry (METI) approved the Japan Photovoltaic Energy Association in 2008 to provide subsidies for residential PV installations, and a feed-in-tariff was established in 2012 to help reduce carbon emissions by 2020 [18, 19]. The FIT has contributed significantly to a large increase in installations, including 6.9 GW installed in 2013 [18].

China's history of strong support of solar power is more recent. The Renewable Energy Law was passed in 2005 encouraging support of renewable technologies and set up grants and subsidized loans for renewable projects [3]. The Golden Sun program began in 2009, which subsidizes the installation cost for photovoltaic units with the goal of reaching 500 MW of PV modules installed [59]. Feed-in tariffs were also instituted for large-scale projects in 2007 [59].

The United States has a high variety of policies in support of solar power [61]. U.S. support of solar power began with an incentives program in 1978, the Public Utility Regulatory Policies Act, which provided payments based on the cost of traditional generation avoided. However, this was not extremely effective at encouraging solar installations [3]. Federally, tax credits have been used since 1978 to offset high installation costs. Initially investment tax credits of up to 30% of installation costs were used, and in 1992 a production tax credit (PTC) was started [3, 61]. The

investment tax credit (ITC) for residential and businesses was raised in 2005, leading to a large increase of PV units in the U.S. [3].

Many states have independent renewable portfolio standards (RPSs) to require certain percentages of renewable energy. These include renewable portfolio standards (RPSs) in 29 states of up to 40% renewables, energy efficiency measures in 20 states, and net metering policies in 43 states [67]. It is estimated that 23 GW of renewable power installed in the U.S. between 1998 and 2009 was due to RPS requirements [20]. In addition, the U.S. solar installations increased 41% from 2012 to 2013, installing 4.75 GW in 2013 to bring the total U.S. PV capacity to 12.1 GW [28].

California has proposed several incentive programs for solar power, and currently has the highest installed capacity of solar power in the United States [28] with 8,544 MW installed [70]. California's California Solar Initiative (CSI) has led to the installation of over 1900 MW of rooftop solar panels since its inception [71]. CSI is a rebate program which subsidizes system costs based on several levels of system performance [61]. These rebates decrease with time under distinct levels [16]. Net metering policies were also effective at reducing consumers' electricity rates and encouraging installations [66].

New Jersey has also seen a high growth in solar power, motivated by a range of policies including state-level RPS, tax credits and subsidies [61]. Its RPS, which went into effect in 2001, had a specific solar energy provision which was later combined with rebates and net metering programs [72]. It had the second most installed capacity of photovoltaics in 2010, however funding issues led to the close of the rebate program in 2007 and subsequent policy were less effective at encouraging growth [72]. The market as begun to recover and grow, however New Jersey has dropped in rank for total installed capacity in the U.S. [28].

Developing countries, including India, Brazil, Kenya and many others, are also incorporating renewable energy policies in their future plans for electricity market development and growth [18, 26, 27, 73]. These countries tend to favor subsidies and feed-in tariffs over RPS's or TGC's [26]. Of the 31 developing countries with renewable energy policies, 28 have some form of FIT [26]. These developing markets also have a higher percentage of off-grid PV installations, which allow electricity to be provided to locations not served by traditional power facilities [61, 73]. Another policy utilized by developing countries is micro-financing of solar installations, allowing for low interest loans for small PV systems [61].

### **1.2.3 Grid Integration**

As the fraction of renewable energy sources incorporated in the electric grid increases, so do concerns about reliability [31–33]. Wind and solar energy in particular are not dispatchable resources and can vary on time scales as small as minutes to seconds. Particularly if a balancing area has limited flexibility this can present problems for grid reliability operators, who must provide an adequate supply of energy to meet demand even as renewable sources vary [34, 35]. If traditional generators, such as coal and natural gas plants, cannot meet rapidly changing net loads, significant curtailment of renewable generation could occur [36, 37]. Grid operators are also interested in whether the variability of renewable sources may lead to different use patterns for traditional power sources, and whether these use patterns negatively impact the efficiencies and maintenance costs of traditional facilities [37].

Many studies have been performed to analyze the operational challenges of renewable integration in order to determine the potential impacts on existing or future electric grids, as well as to identify potential benefits of such integration [74]. Challenges can include grid stability, lack of reserves, high cycling of traditional power

plants, and curtailment of renewable energy. These challenges are balanced by benefits which may include reducing the production costs for the overall system due to lower fuel and operational costs, as well as reduction in greenhouse gas emissions. Integration studies have been done for a range of system sizes, including all of Europe [75], the U.S. interconnections [37, 76–78] and local areas [36, 79–81]. While many of these studies focus more specifically on wind power, solar integration faces similar challenges due to its variable nature. In some cases the challenges of generator ramping are more extreme due to a reduction in solar panel output as the typical evening peak load increases [36].

While suggestions for addressing this issue have been raised [82, 83], the integration of renewable energy is an ongoing question. Particularly as the amount of renewable generation increases, the ability to provide dispatchable energy from these sources will become more valuable.

### 1.3 Photovoltaic Market

Cost has historically been a strongly limiting factor for solar power installations, which were considered to be cost prohibitive except in very specific applications. However, current technologies have improved and costs dropped such that photovoltaics are becoming more affordable. Since their initial use in the 1950's, module costs have dropped from over  $\$100/W_p$  to less than  $\$1/W_p$  [29], and between 2010 and 2013 costs dropped by over 50% [30]. Large, sudden increases in demand fueled by governmental policies exceeded production briefly in the early 2000's, leading to a small increase in price [59]. However, the overall trend has been a steady decrease in price. In addition, while module costs increased slightly in 2013, the total system costs decreased 9% for residential and 14% for utility-scale installations, in large part due to dropping

inverter and balance of system costs [28].

The PV market is largely dominated by crystalline silicon, accounting for 80-85% of the global market in recent years [61, 84], followed by thin-film technologies. Crystalline silicon has the advantage of being more efficient, typically 12-15%, and has a lower degradation rate [84, 85]. However, these technologies also requires more silicon than other photovoltaic types [59]. Thin-film on the other hand requires less silicon or other conducting materials, but currently have efficiencies less than 10% [59, 86]. The costs of crystalline silicon modules are expected to be cost competitive without subsidies at a manufacturing cost of  $\$0.75 - 0.50/W_p$ , which could feasibly be reached by 2030 based on improvements in manufacturing and module efficiency [84]. Thin film presents a promising alternative, however is currently at a more developmental stage [87]. For this analysis, crystalline silicon modules will be considered as the dominant technology.

### 1.3.1 Historical Costs

The cost of photovoltaic modules have dropped drastically in the past several years. In 2010, the cost of a PV module was  $1.85 \$/W_p$ , whereas in 2013 it had fallen to  $0.72 \$/W_p$  [30]. Figure 1.2 shows the module price from 1975 through 2013. In addition to dropping module costs, installation and balance of system costs are also dropping as experience increases [88].

Some of the cost decrease in recent years was due to over-supply in an expanding market, however much of the decrease is due to falling material costs, improvements in efficiency, advances in manufacturing processes, and reaching economies of scale [18, 88, 90, 91]. There is also speculation that Chinese manufacturers are dumping PV modules into the market, further contributing to the drop in prices [88].

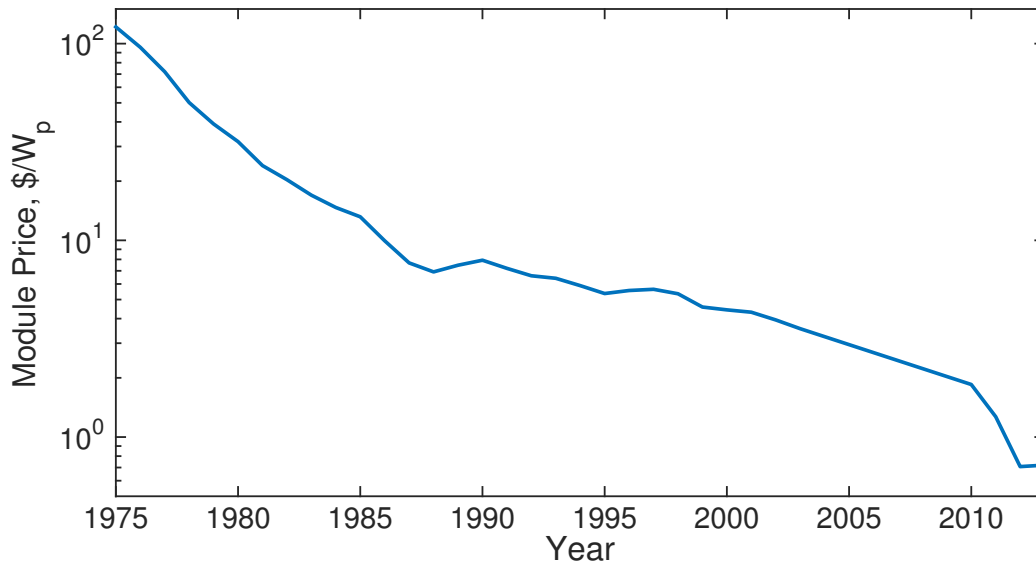


Figure 1.2: The price of photovoltaic modules has been dropping since the 1970's, showing significant cost reduction in the technology. The data is shown on a log scale for clarity. Data from [29, 89]

The cost of photovoltaics has dropped such that PV systems may be cost competitive without subsidies in 15 countries [18]. System costs are expected to continue dropping in cost, potentially reaching  $\$1/W_p$  by 2022 [92, 93]. This price is widely seen as the installed system price at which solar power would reach grid parity [22, 88, 94, 95]. Many countries also have set goals to encourage continued reduction in cost of PV modules and total system costs [22].

### 1.3.2 Learning Curves

Part of the recent drop in module prices may be attributable to the concurrent rise in photovoltaic installations [88]. The price of photovoltaics has been found to follow a learning curve, which describes a drop in price that scales with the number of units produced [29, 89, 90, 94, 96–98]. Specifically, the learning curve relationship is a power-law relating the cumulative number of units produced to the cost of producing

those units, Eq. (1.1).

$$c = c_0 \left( \frac{n}{n_0} \right)^\alpha \quad (1.1)$$

where  $c$  is the cost at a particular time  $t$ ,  $c_0$  is the initial cost,  $n$  is the cumulative production also at time  $t$ ,  $n_0$  is the initial produced capacity, and  $\alpha$  is related to the learning rate,  $LR$ , of the technology as

$$LR = (1 - 2^\alpha) \quad (1.2)$$

Figure 1.3 shows the price of photovoltaic modules as a function of cumulative production, including a line of best fit. This figure clearly shows the log-linear relationship between price and cumulative production of photovoltaic modules. The module price is frequently used as a proxy for manufacturing cost due to the difficulty in acquiring proprietary manufacturing cost data, however likely introduces some error into the analysis due to non-constant margins [29].

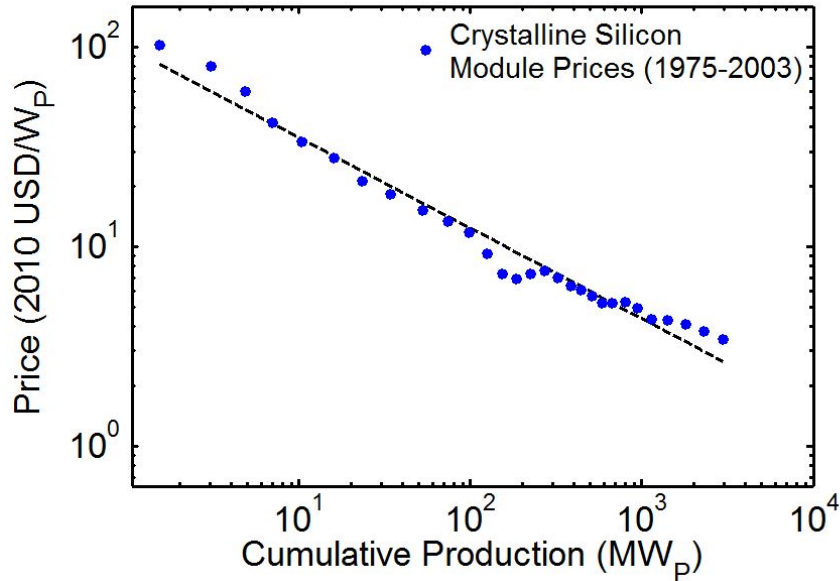


Figure 1.3: The price of photovoltaic modules has been dropping as production of modules increases, in a power law trend. Data from [29, 89]

Photovoltaics have the highest learning rate of any energy technology, approximately 0.20, indicating that photovoltaics show a higher cost response to production increases than other technologies. Table 1.2 shows learning rates for PV, wind and nuclear power [96, 99]. In particular, the learning rate for PV is nearly twice that for wind, indicating a higher rate of cost reduction. Experience curves and projected learning rates have been used to predict the total investment required to bring photovoltaic costs to grid competitive levels, and to estimate the effectiveness of different policies [98, 100, 101]. Because of the learning relationship, policies encouraging installations of photovoltaics also tend to drive reductions in cost.

Technology	Average Learning Rate	Learning Rate Range
Photovoltaic	0.20	0.10 – 0.47
Wind	0.11	0 – 0.17
Nuclear	0.0	<0 – 0.0

Table 1.2: The learning rate indicates the cost reduction expected with a doubling of cumulative production of that technology. Data from [99].

This has important implications, particularly for developing countries, as photovoltaics are now reaching much lower costs than considered in previous analyses and are likely to continue dropping [73, 102]. At current prices, photovoltaics are cost effective in many regions of the world, including developing regions such as Africa and southeast Asia [42]. As additional policies are put in place encouraging installations of photovoltaics, the rise in production is likely to lead to further drops in cost, making photovoltaics more advantageous for developing countries with high irradiance levels.

## 1.4 Grid-scale Storage

Storage facilities are greatly important for renewable technologies such as solar power to be able to provide dispatchable power. These resources are not inherently dispatchable, and so must be able to store excess energy from times when it is plentiful



for use when it is not. For solar power, this is predominantly a diurnal cycle between day and night. Additionally, seasonal variability exists with more solar energy available in the summer than the winter. This variability is more difficult to account for with storage due to the long storage times required.

There are currently several technologies available for grid scale storage: pumped hydroelectric storage (PHS), compressed air energy storage (CAES), and grid-scale batteries. Other storage technologies exist, such as flywheels, capacitors, superconducting magnetic storage and others, however these technologies are limited by the storage capacity required for grid-scale operation, by the storage time to meet the needs of a diurnal cycle, or by cost [38, 41].

#### **1.4.1 Pumped Hydro Storage**

Pumped hydroelectric storage (PHS) is a large-scale storage medium with a high round-trip efficiency, 65 - 85% [38, 41, 44]. It is well suited for use with intermittent renewable sources such as solar power due to long storage times and high efficiencies [38]. Water is stored in the lower reservoir, and when energy is available this water is pumped to the upper reservoir where it is stored until energy is needed. It then flows back to the lower reservoir, producing energy in the process.

This storage medium can have capacities of 100s to 1000s MW, with storage times up to months (or even years) [38] and is capable of discharging energy on hourly or daily time scales [38, 41]. Such long-term, large-scale storage capability allows for daily and even seasonal variations to be accounted for via storage. It has also been shown specifically that solar power is capable of providing a reliable stream of electricity when an appropriately sized array and storage facility are coupled [103].

This is a mature technology, with plants installed as early as the 1940's [43].

As of 2010 there was a global installed capacity of pumped hydro storage of over 95 GW. Japan and the United States lead the world in PHS, with 24.6 GW and 21.9 GW, respectively [43].

The downsides of pumped hydro storage are the requirements for siting such a facility. Large amounts of water are required to provide sufficient energy from the facility. These systems have reservoirs potentially in excess of 10,000,000  $m^3$  for a large facility [104]. In addition, a height differential is required between two separate reservoirs. This height differential allows for the storage of energy, rather than just production as in a traditional dam. New pumped hydro facilities have been found to be difficult to site or expensive to build in available locations [43].

#### 1.4.2 Compressed Air Energy Storage

Compressed air energy storage (CAES) is a large-scale storage medium with the capability of storing energy for 10's of hours and up to 100's or even 1000's of MW [49]. It operates by decoupling the compressor and turbine in a traditional natural gas plant, Fig. 1.4. The compressor is run at times of low energy prices, compressing air into a reservoir until it is needed to drive the turbine. When energy is required or electricity prices are high, the compressed air is preheated then used to drive a turbine providing energy. The use of fuel, typically natural gas, for preheating leads to an energy ratio of (electricity in):(electricity out) less than 1. The energy ratio is typically between 0.56 and 0.84 [47–49]. In addition, the turbine of a CAES facility is able to provide more energy than a comparable single-cycle combustion turbine, as much as 2-3 times more power, as the full output is directed towards energy production and not compression [48, 49].

The compressed air can be stored in underground caverns, most feasibly in salt domes but also potentially in aquifers and other porous rock, or excavated hard rock

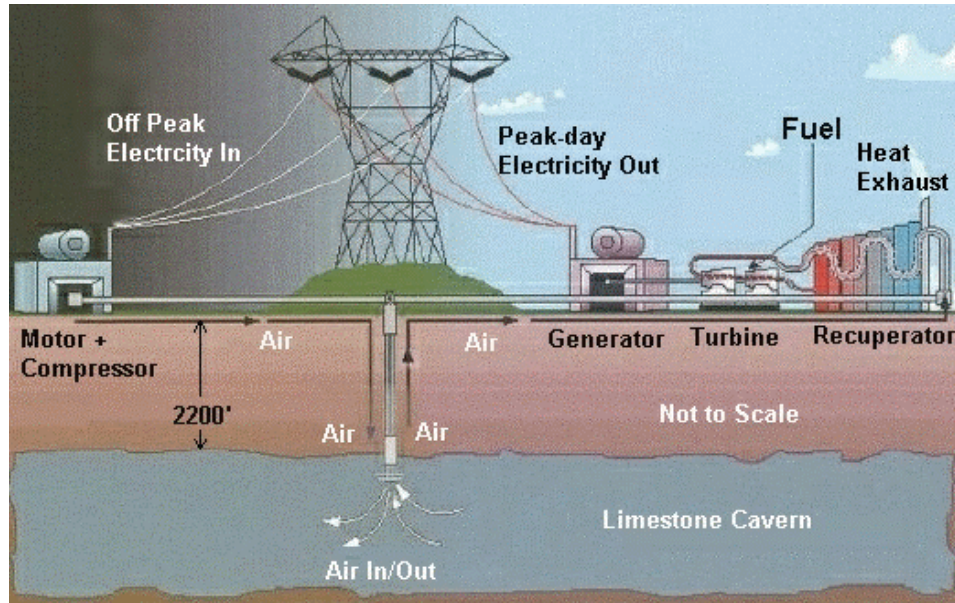


Figure 1.4: Graphical representation of a CAES facility operating in a limestone cavern. This image was taken from [48], showing the proposed plant in Norton, Ohio.

caverns. Salt domes present the most likely candidates for CAES siting; currently the only two operating CAES facilities use salt domes for their storage [49]. These geologies are beneficial because they are easy and cheap to excavate, and also are not likely to leak air [49]. Hard rock caverns would prove to be a much more expensive option for CAES facilities due to the additional excavation costs. However, it has been proposed that existing mines could potentially be used, reducing some of this cost [48, 49]. Porous rock, most notably aquifers, provide another solution for CAES reservoirs. These storage facilities could potentially be even cheaper to build than cavities in salt domes, however their costs are largely unknown until a detailed analysis is performed [49, 105].

CAES is considered to be a mature technology, however only two facilities have been built. The first CAES facility was built in Huntorf, Germany in 1978 [41, 49]. Its capacity is 290 MW, and while it was built with 2 hours of storage, it has since

been expanded to 3 hours of storage [49]. It was built in two salt caverns with a total volume of  $310,000 \text{ m}^3$  [49]. It is still operational today, providing both black start capabilities as well as smoothing output from wind farms in the North Sea.

The second CAES facility was built in MacIntosh, Alabama in 1991 [41, 49]. Its capacity is 110 MW and includes 25 hours of storage [49]. It is located in a single salt cavern with a total volume of  $560,000 \text{ m}^3$ . It is also still operational, providing load management, peak power, ramping capability, and reserves for the local electric grid [48]. Several other CAES facilities have been proposed in locations such as in Norton, Ohio [49] and Des Moines, Iowa [105], or have been investigated in states such as Texas and New Mexico [106]. However none of these projects have yet been built.

Similar technologies as below-ground CAES can be used for above-ground, or small-scale, CAES. Instead of utilizing underground caverns for storage, high-pressure tanks or gas pipes are used [48]. These facilities have lower potential storage capacities than underground CAES, however operate on the same principles. They typically have capacity for roughly 5 hours of storage, and capacities of approximately  $10 \text{ MW}_e$  [48, 107]. Above-ground CAES could be ideal for smaller-scale operations, or several facilities could be coupled to provide energy on a similar scale to below-ground CAES.

The main challenge for compressed air energy storage facilities is siting, due to the need for a large underground storage facility. Unlike pumped hydroelectric storage however, these required geologies are more widely available. While salt domes provide the most ideal and tested geology, there are many other potential geologies available. It is estimated that over 75% of the United States has geology that would be acceptable for CAES facilities [108]. This makes CAES a much more widely site-able technology. It also has a much smaller surface foot-print, impacting a smaller portion

of the above-ground area than PHS [49]. Another challenge for CAES is the lack of experience, with only two facilities currently in operation.

### 1.4.3 Batteries

There are several means by which energy can be stored electrochemically, including batteries, which store energy based on charge transfer reactions between an anode and cathode, and redox-flow batteries, which store energy in an external electrolyte that flows through the cell [38, 45]. There are many different battery technologies for a variety of different applications, including power quality regulation, load shifting, and back up power provision [45, 50, 109]. These range from time scales of seconds to hours and capacities of kilowatts to 10's of megawatts [45, 109]. For this analysis, I will focus on the large-scale systems for use with load-shifting and renewable integration.

Battery types vary based on the materials and chemicals used for the electrode and electrolyte [109]. Common types of batteries include lead-acid, lithium-ion, sodium-sulfur (NaS), Nickel-metal hydride, and vanadium redox flow batteries. Sodium-sulfur and lead-acid batteries are both mature technologies, whereas large-scale lithium-ion and vanadium redox batteries are in demonstration phases [38, 109]. There are also many other battery varieties currently being investigated for improvements in life cycle, efficiency, or cost.

The efficiencies of batteries vary widely by type of battery, and also among the same battery chemistries. The lowest reported efficiencies are seen for vanadium redox flow batteries, 70%, while lithium ion batteries claim the highest efficiencies of up to 95% [109].

Batteries have been used for grid-scale applications, particularly lead-acid

batteries of up to 10 MW systems in California [50] and sodium-sulfur systems in Japan [45]. Flow batteries are beginning to be demonstrated at large scale, and lithium-ion batteries are being used at scales of a few MW [110]. Redox flow batteries are currently in demonstration with capacities up to a few MW, and have the benefit of decoupling the power and energy storage aspects of the battery to allow for variable storage capacities [45, 50].

Cost is the most common concern for all types of batteries. Most battery technologies are still too costly to be widely deployed [38, 50]. In addition, environmental concerns exist for some battery types, such as nickel-metal hydride batteries [50, 109]. However, batteries have very limited siting concerns, with no geographical requirements such as CAES and PHS, and could be ideal in the future as the technologies continue to improve.

## Chapter 2

### Irradiance Calculation

#### 2.1 Algorithm

Creation of a global solar irradiance dataset was of foremost importance for the research in this dissertation. I utilized a standard algorithm [54] to create surface solar irradiance values using satellite data from the International Satellite Cloud and Climatology Project (ISCCP) [51]. This data set will be discussed in detail in Section 2.2, I here discuss the methodology of creating the irradiance values.

The total surface irradiance was computed by first determining the total irradiance transmitted through just the atmosphere. This value is then used to compute clear sky and cloudy sky components. The total transmitted irradiance,  $Q_{dir}$ , is computed as

$$Q_{dir} = f(I_0, d, \mu_0, O_3, H_2O, V, P_s) \quad (2.1)$$

where  $I_0$  is the solar constant [ $W/m^2$ ],  $f$  is clear sky transmission, Eq. (2.2),  $d$  is the earth-sun distance [km],  $\mu_0$  is the cosine of the solar zenith angle [dimensionless],  $O_3$  is the ozone content [Dobson Units],  $H_2O$  is the amount of water vapor in the atmosphere [ $gcm^{-2}$ ],  $R_s$  is the surface reflectance [dimensionless],  $V$  is the visibility [km], and  $P_s$  is the surface pressure [millibars].

The function  $f$  used in Eq. (2.1) represents the formula provided in [55]:

$$f(I_0, d, \mu_0, O_3, H_2O, R_s, V, P_s) = I_0 * \left(\frac{d_0}{d}\right)^2 * \mu_0 * \frac{e^{-\frac{(a+b/V)*P_s}{\mu_0}}}{(1 - R_s * \frac{a'+b'}{V})} * e^{-a_v \left(\frac{H_2O}{\mu_0}\right)^{b_v}} * e^{-a_o \left(\frac{O_3}{\mu_0}\right)^{b_o}} \quad (2.2)$$

Here  $d_0$  is the mean earth-sun distance, and  $a$ ,  $b$ ,  $a_v$ ,  $b_v$ ,  $a_o$ , and  $b_o$  are regression coefficients given in Frouin et. al. (1987) [55] for land and water at different wavelength intervals. For the present study I use the coefficients for the full range of solar radiation, 250-4000 nm, Table 2.1.

unit	a millibar <sup>-1</sup>	b $\frac{km}{millibar}$	a	b	av $(\frac{cm^2}{g})^{-b_v}$	bv	ao DU <sup>-b_o</sup>	bo
Maritime	0.059	0.359	0.089	0.503	0.102	0.29	0.041	0.57
Continental	0.066	0.704	0.088	0.456	0.102	0.29	0.041	0.57

Table 2.1: Coefficients used in Eq. (2.2), given in Frouin et al. (1989) [55]. DU denotes Dobson units.

Once the transmitted irradiance is computed, Equation (2.1) is used to compute the clear sky irradiance,  $Q_{clr}$ , and cloudy sky irradiance,  $Q_{cld}$ :

$$Q_{clr} = (1 - CF) * Q_{dir} \quad (2.3)$$

$$Q_{cld} = (CF * Q_{dir}) * (1 - A_z) * (1 + A_s R_s + (A_s R_s)^2) \quad (2.4)$$

where  $CF$  is the cloud fraction [dimensionless],  $A_z$  is the cloud albedo [dimensionless] and  $A_s$  is the spherical albedo [dimensionless]. The terms in  $Q_{cld}$  represent transmission through the atmosphere to the top of a cloud, transmission through the cloud, and reflection between the Earth's surface and the bottom of the cloud, respectively. Figure 2.1 shows the relationship between  $Q_{dir}$ ,  $Q_{clr}$ ,  $Q_{cld}$ ,  $A_s$ ,  $A_z$ , potential cloud layers, and the Earth's surface. The total irradiance is then computed as:

$$Q_{tot} = Q_{clr} + Q_{cld} \quad (2.5)$$

## 2.2 ISCCP Data

The data used to compute these irradiance values were taken from the International Satellite Cloud Climatology Project (ISCCP). The ISCCP has been recording



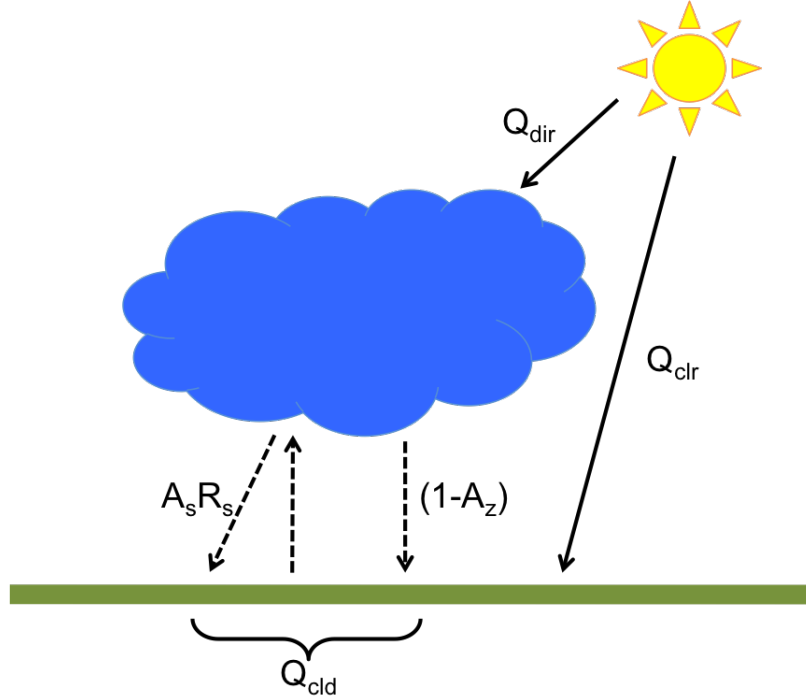


Figure 2.1: The figure shows visually how surface solar irradiance is calculated as a sum of clear sky solar radiation and the fraction of radiation transmitted through a cloud and then reflected from the Earth's surface.

weather data from geostationary and polar orbiting satellites since 1983. These data were gathered from 46 different satellites throughout this time span, the details of which are available at <http://isccp.giss.nasa.gov/docs/sathist.html#default> [111]. An extensive calibration effort was undertaken to put these data on an even footing [112] and they are available in 3-hr time steps from July 1983 through June 2008 via ftp at <ftp://eclipse.ncdc.noaa.gov/pub/isccp/dx>. The ISCCP data consists of two data sets, DX and D1, both of which were used in this study. The DX data have a 3-hour temporal and  $0.5^\circ \times 0.5^\circ$  angular resolution. These data were processed and combined to create a lower resolution product, the D1 data set, which consists of a 280-km equal-angle grid and also a 3-hour temporal resolution. The D1 data include spatial averages of the DX data set as well as statistical summaries of the variables [51].

Data for  $O_3$ ,  $H_2O$ , and  $P_s$  were taken from the ISCCP D1 data set [53] as these variables were not available in the DX data. Data for  $R_s$ ,  $CF$ , and cloud optical thickness,  $\tau$ , are taken from the ISCCP DX data set [52]. DX data were preferred due to the higher resolution of this data. I used a fully benchmarked in-house implementation, [113], of the doubling method to compute  $A_z$  and  $A_s$  using the cloud optical thickness values from the ISCCP DX data set. Surface visibility,  $V$ , was assumed to be 25 km [55], and the mean earth-sun distance,  $d/d_0$ , was computed using:

$$\frac{d}{d_0} = \frac{1 - E^2}{1 + E * \cos(\theta)} \quad (2.6)$$

$$\theta = \frac{2\pi x}{Y} \quad (2.7)$$

where  $E$  is the earths eccentricity, 0.01671,  $Y$  is the length of a year, 365.25 days, and  $x$  is the number of days since the perihelion. The solar zenith angle,  $\mu_0$ , was computed using the formulas given in the National Ocean and Atmospheric Administrations Solar Calculator [114].

The ISCCP uses two types of satellites: polar orbiting and geostationary. The geostationary satellites collect data for particular regions of the planet while the polar orbiting satellites encircle the globe throughout a day and are generally used to acquire data over the polar regions, as well as to supplement the geostationary satellites when they are unavailable or record faulty data.

The data from all of these satellites must be combined in order to create a world-wide data set. To accomplish this, I followed the algorithm of Bishop et al 1997 [54]. A minimal filling scheme was used to account for locations for which data are missing, either because they were not observed by satellites at a particular time of day, or because available data for that location has an error flag. For a particular 3 hour period, the worldwide filled data set was generated as follows:

1) Data for  $O_3$ ,  $H_2O$ ,  $R_s$ ,  $P_s$ , optical thickness and cloud fraction from each satellite are put into a  $0.5^\circ \times 0.5^\circ$  equal angle grid, mapped according to latitude and longitude.

2) If multiple satellites report data for the same location, data was taken from the satellite with the solar zenith angle closest to normal incidence, with a preference for geostationary satellites over polar orbiting satellites.

3) If data for a particular location was missing, it was filled in the following order:

i) at the equator it was assumed to have the same value as a directly adjacent location. The filling was done longitudinally where the location directly to the East was used to fill the missing data, if this too was absent, the location directly to the West was used. Away from the equator the number of bins, East and West, used for filling was increased to account for the fact that  $0.5^\circ$  of longitude corresponds to a shorter distance as one moves toward the poles. The number of bins, East and West, from which data was taken for filling was increased by one as  $1/\cos(\text{latitude})$  incrementally increased from 1 to 57. If the East-West neighbors were absent, the location directly to the north was used, and if that was absent, the location directly to the south.

ii) If data for a particular location was still missing, it was assumed to have the average value over all daylight hours for that particular day. Several variables, solar zenith angle, cloud optical thickness, and surface reflectance, are reported only during the daylight hours, and so only can be filled from these hours of the day.

iii) If data was still missing, and for variables that are recorded during both day and night, the 24-hr average is used to fill.

iv) If any of the variables for a particular location was still missing, the 24

hour average irradiance for a particular day was filled in a post processing step with the historical average irradiance for that day.

Equations (2.1)-(2.7) were used to determine the surface solar irradiance for each 3 hour time stamp and location for all 25 years. I use a Riemann sum to integrate over  $\mu_0$  to compute the average irradiance within each 3 hour period. All ISCCP variables are given a single value for each period, whereas the solar angle  $\mu_0$  was calculated at 12 minute intervals. Twenty-four hour irradiances were computed by a Riemann sum of all 12-minute intervals within the 24-hour period.

Irradiances were also computed at sub steps of 1-hour to allow for finer resolution analysis. These irradiances were computed by holding all variables fixed over each three-hour time step except for the solar zenith angle  $\mu_0$ . This was computed again at every 12-minute interval within the 1-hr period and averaged to determine 1-hour temporal resolution irradiance values. Figures 2.2 and 2.3 show the hourly irradiance for the whole globe for two days in January and June, respectively.

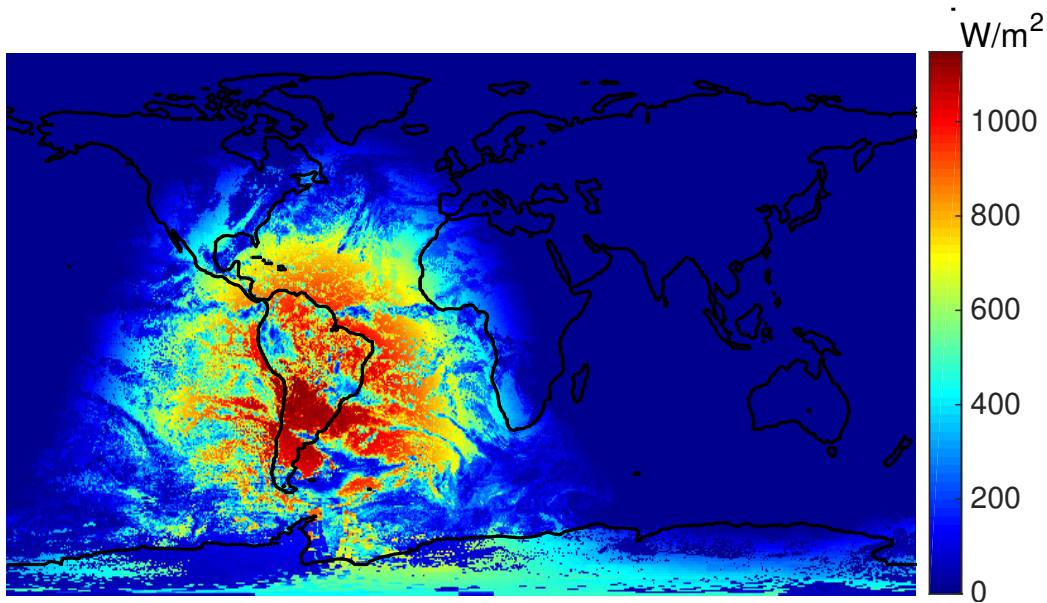


Figure 2.2: Example map of irradiance values for one time stamp of the analysis. This example is for Jan 1, 1700 GMT, 2007.

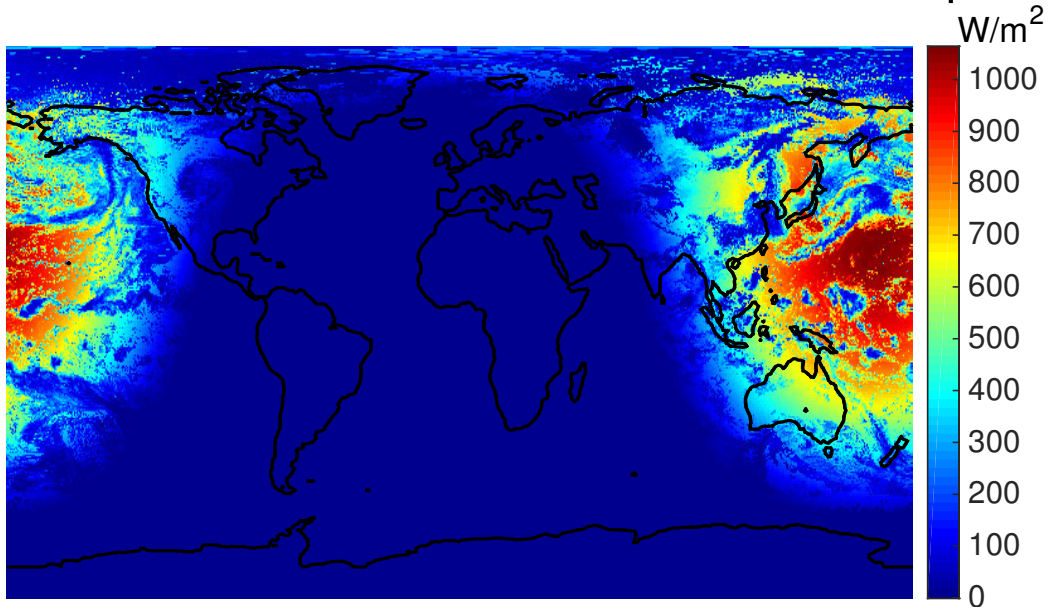


Figure 2.3: Example map of irradiance values for one time stamp of the analysis. This example is for June 1, 300 GMT, 2007.

### 2.3 Comparison to Ground-based Data

In order to validate the computed irradiance values, I identified four databases containing ground-based irradiance measurements overlapping in time with the ISCCP data for specific locations. I assume that the comparisons at these locations are similar to all other global locations and provide sufficient validation of the above algorithm for the entire data set. I computed 24-hour averages for each of these data sets and compared these values with the corresponding 24-hour averages of the computed irradiance values from the ISCCP data. The data sets used for comparison include the Biowatt [115], Marine Light Mixed-Layer (MLML) [116] and First ISCCP Regional Experiment and Cirrus 1 Surface Radiation Budget (FIRE/SRB) [117] experiments as well as data from the Baseline Surface Radiation Network (BSRN) [118].

### 2.3.1 Biowatt II

The Biowatt II experiment consists of three separate deployments of instruments in 1987 to measure oceanic and meteorological data in the Sargasso Sea. A buoy was attached to the ocean floor at  $34^{\circ}\text{N}$ ,  $70^{\circ}\text{W}$ . Data were collected from February 28 to May 11 for the first experiment, May 13 to August 30 for the second experiment, and August 31 to November 23 for the final experiment [115].

Figure 2.4 shows the 24-hour averaged irradiance values for both the Biowatt experiment data and the computed irradiance values from the ISCCP data set. The values show good agreement for all three experiments, though not an exact match.

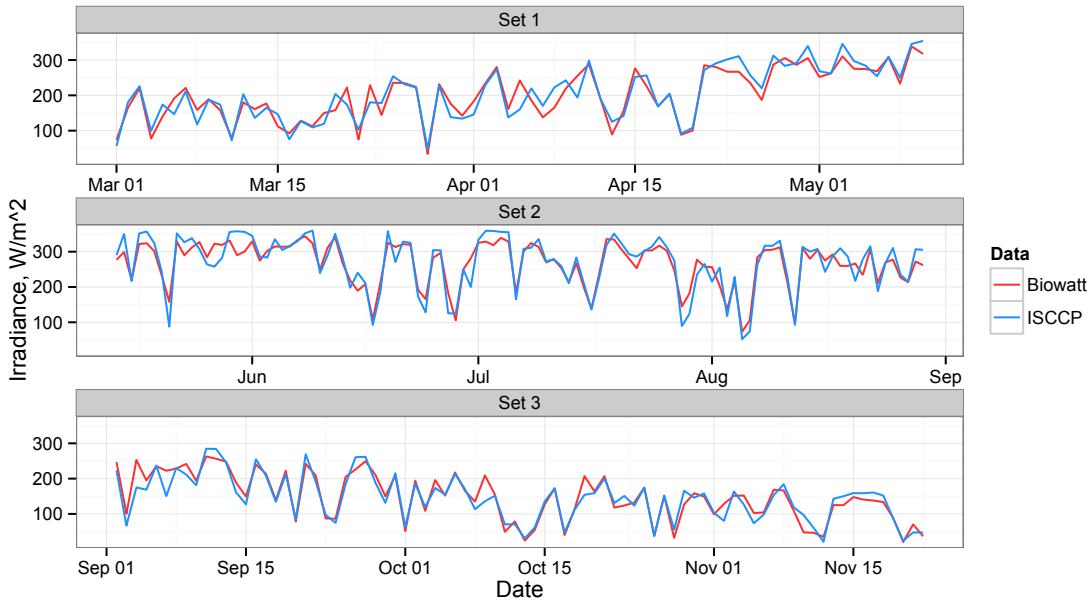


Figure 2.4: The Biowatt dataset consists of data from the same location at three different time periods within 1987.

In order to determine the degree to which the computed irradiance values correspond to the measured irradiance values, I computed correlation coefficients between the two measurements for each Biowatt experiment. The correlation values

can be seen in Table 2.2, and are shown graphically in Fig. 2.5. Table 2.2 also shows the mean error and standard deviation in error for each of the experiments. This error represents 1.5%, 1.3%, and 2.0% of the Biowatt irradiance values for experiments 1, 2, and 3 respectively.

	Correlation Coefficient	Mean Error	$\sigma_{error}$
Set 1	0.93	-3.0	27.6
Set 2	0.93	-3.4	28.7
Set 3	0.94	2.9	23.5

Table 2.2: Correlation and error measurements for the Biowatt data set compared to computed ISCCP values. Error was computed as  $IR_{Biowatt} - IR_{ISCCP}$ .

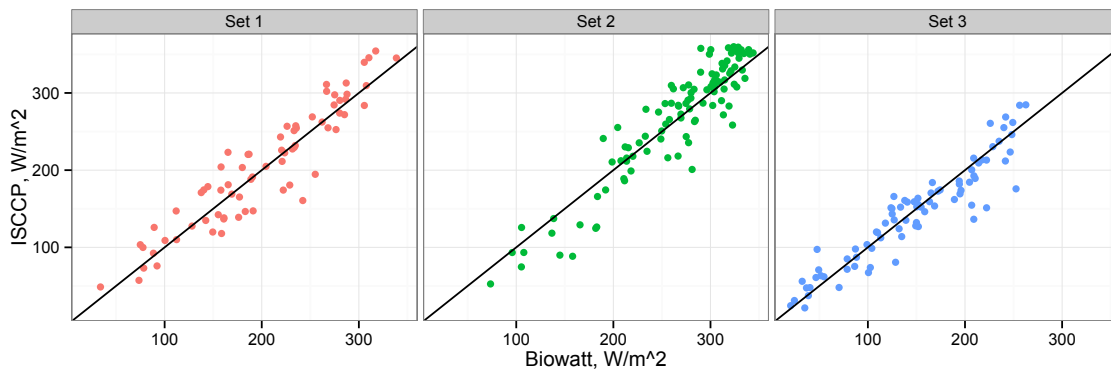


Figure 2.5: The Biowatt dataset consists of data from similar locations at two different years.

### 2.3.2 MLML

The Marine Light Mixed-Layer (MLML) experiment consists of data from a buoy anchored in the subarctic North Atlantic Ocean. Two separate experiments were performed at the same site. The first experiment was from April 14 through June 10, 1989 and the second from April 30 through September 6, 1991 [116]. While the intent of these experiments was to examine the mixing of ocean layers, irradiance values were collected and made available for download. The buoy used to collect data was anchored at 59°35.61'N, 20°57.85'W, approximately 275 miles south of Iceland.

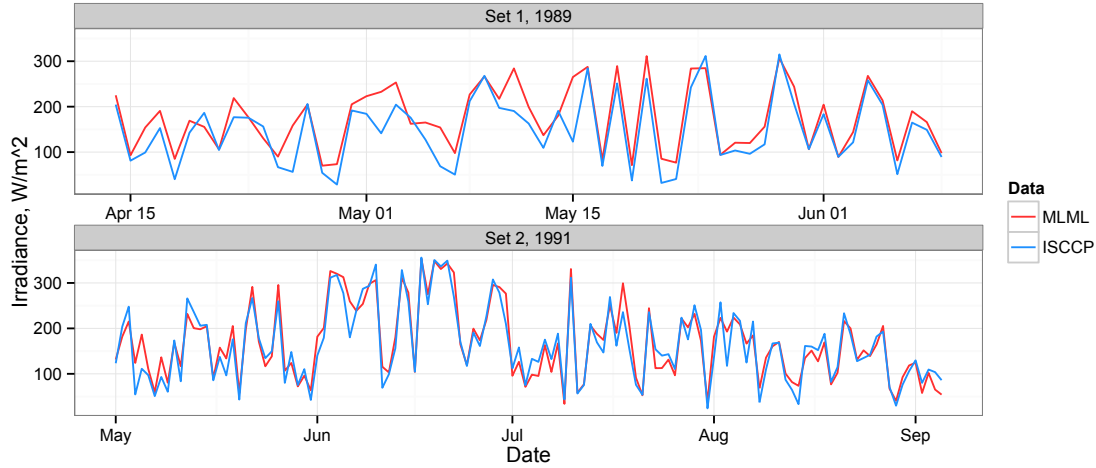


Figure 2.6: The MLML dataset consists of data from similar locations at two different years.

Figure 2.6 shows the irradiance data for each of the two experiments compared to the computed values using the ISCCP data. The data can be seen to follow the same general trends of high and low irradiance in both cases.

In order to directly compare the two data sets, I computed correlations between the paired measurements, Fig. 2.7. The correlation and mean error values can be seen in Table 2.3. The error in irradiance represents 15.4% and 2.6% of the MLML average irradiance values for the 1989 and 1991 data sets, respectively.

	Correlation Coefficient	Mean Error	$\sigma_{error}$
Set 1, 1989	0.91	26.9	31.9
Set 2, 1991	0.95	4.4	26.4

Table 2.3: Correlation and error measurements for the MLML data set compared to computed ISCCP values. Error was computed as  $IR_{MLML} - IR_{ISCCP}$ .

The first data set has a skewness value of 1.1, indicating a positive skewness in error, computed as  $IR_{MLML} - IR_{ISCCP}$ . This shows that the ISCCP data tends to under-predict rather than over-predict the irradiance values. The error values are also significantly leptokurtotic, showing a higher peak around 0 and larger tails than a



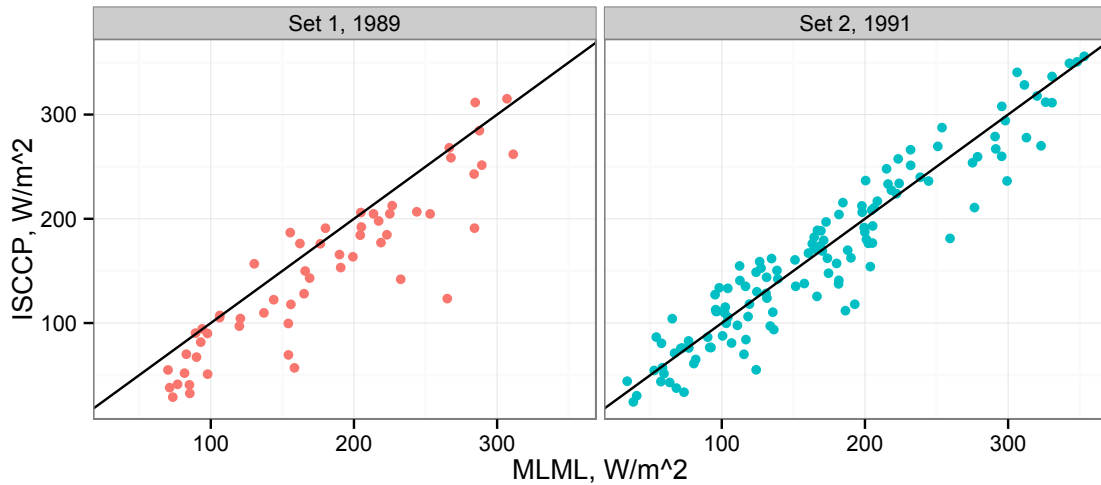


Figure 2.7: The MLML dataset consists of data from similar locations at two different years.

normal distribution. This indicates that the error is more likely to congregate around zero, but also has a higher probability of being large. As such, my algorithm tends to generally provide a good approximation but will at times have a large error. This can be seen in the behavior of Fig. 2.6.

### 2.3.3 FIRE/SRB

The First ISCCP Regional Experiment (FIRE) and Cirrus 1 Surface Radiation Budget (SRB) projects were two experiments performed simultaneously at several locations. They will be referred to together as the FIRE/SRB data set. The experiments were performed in Wisconsin from October 12 through November 2, 1986 in order to determine cirrus cloud measurements and to validate the SRB algorithm [117]. Seventeen sites were identified in Wisconsin; their locations are given in Table 2.4.

These seventeen data collection sites fall within the boundaries of only 9 pixels of the ISCCP data set, such that several of the ground-based locations are compared to the same computed irradiance values. Figure 2.8 shows the locations of all FIRE/SRB

Location	Latitude (deg N)	Longitude (deg W)
Plain	43.28	90.04
Portage	43.56	89.48
Tri-County	43.21	90.19
Reedsburg	43.53	89.97
Dodgeville	42.99	90.15
Mt. Horeb	43.00	89.74
Arena	43.16	89.91
Sauk City	43.30	89.74
Middleton	43.11	89.53
Ft. McCoy	43.96	90.76
Stevens Point	44.55	89.53
Baraboo	43.52	89.77
Adams County	43.97	89.80
Wautoma	44.04	89.30
Wausau	44.92	89.62
Arlington	43.33	89.37

Table 2.4: FIRE/SRB Locations. List of seventeen site locations for data collection during the FIRE/SRB experiment

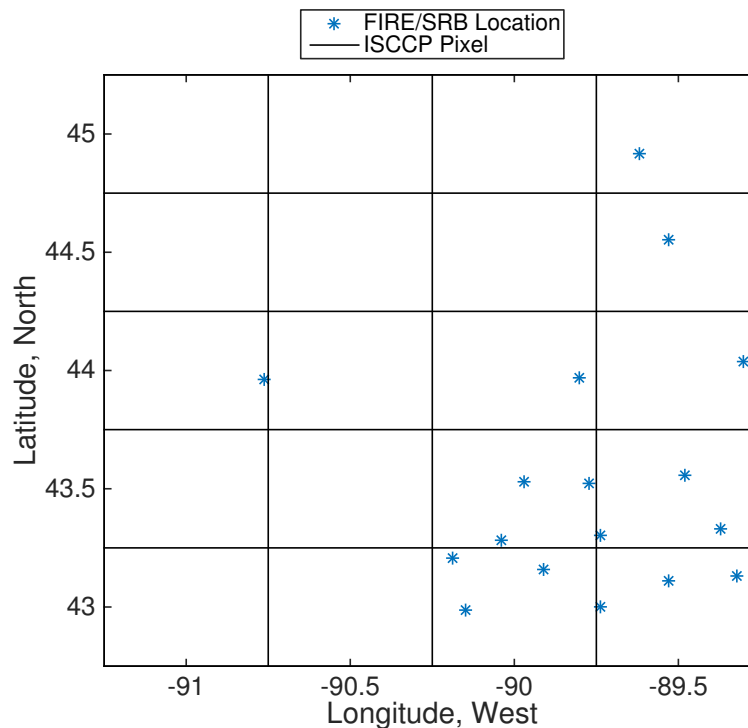


Figure 2.8: The FIRE/SRB dataset contains data from 17 sites. For some of the ISCCP pixel locations, multiple sites of the FIRE/SRB dataset fell within that pixel. The ISCCP pixels are outlined in black, with each site of the FIRE/SRB experiment marked with a \*.

locations and the ISCCP pixel boundaries. Five of the FIRE/SRB locations correspond to unique ISCCP pixels, and the remaining 12 locations are clustered within four ISCCP pixels. Comparisons of the computed irradiance values for each pixel and the corresponding measured values for all FIRE/SRB locations within that pixel can be seen in Fig. 2.9. Missing data values are omitted from the figure.

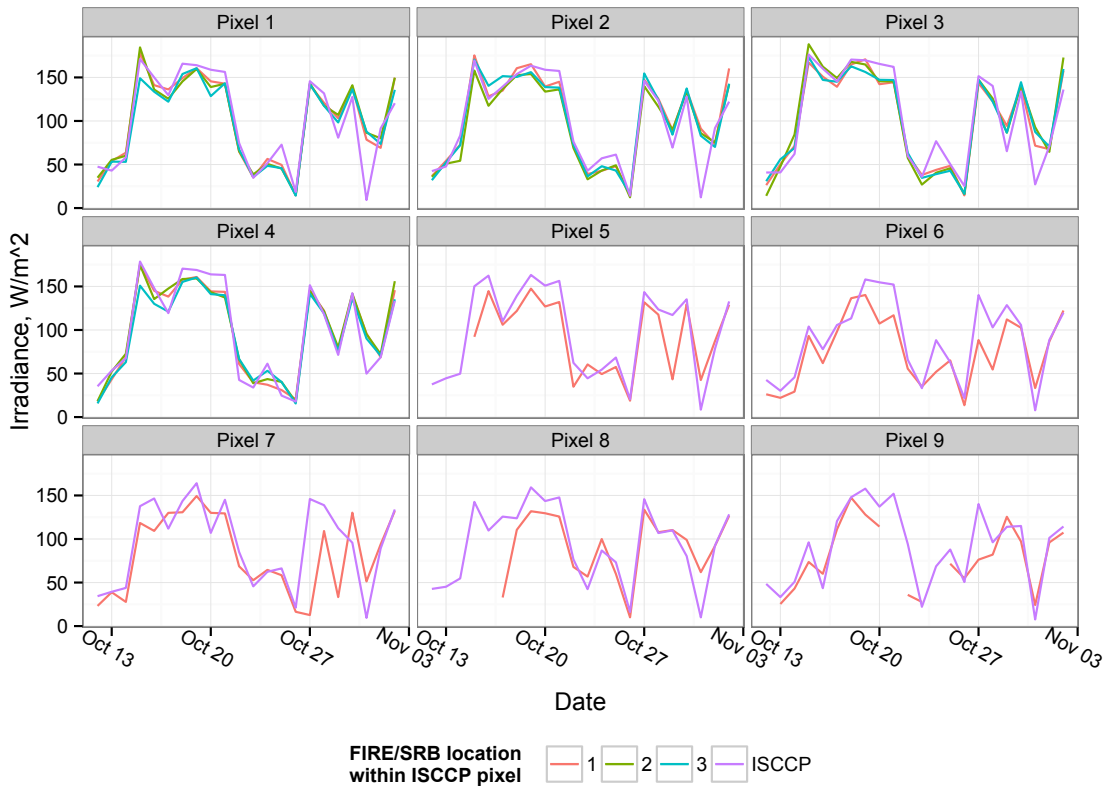


Figure 2.9: The FIRE/SRB dataset consists of data from similar locations at two different years. For some of the ISCCP pixel locations, multiple sites of the FIRE/SRB dataset fell within that pixel. As such, four of the 9 ISCCP pixels are compared to multiple FIRE/SRB locations

I determined the correlation between each location and its corresponding ISCCP irradiance values. These correlations can be seen by pixel number in Figure 2.10, and are listed in Table 2.5. The correlation values range from 0.69 to 0.96. The mean error, also shown in Table 2.5, is between 0.8% and 15.0% of the average irradiance at each FIRE/SRB site.

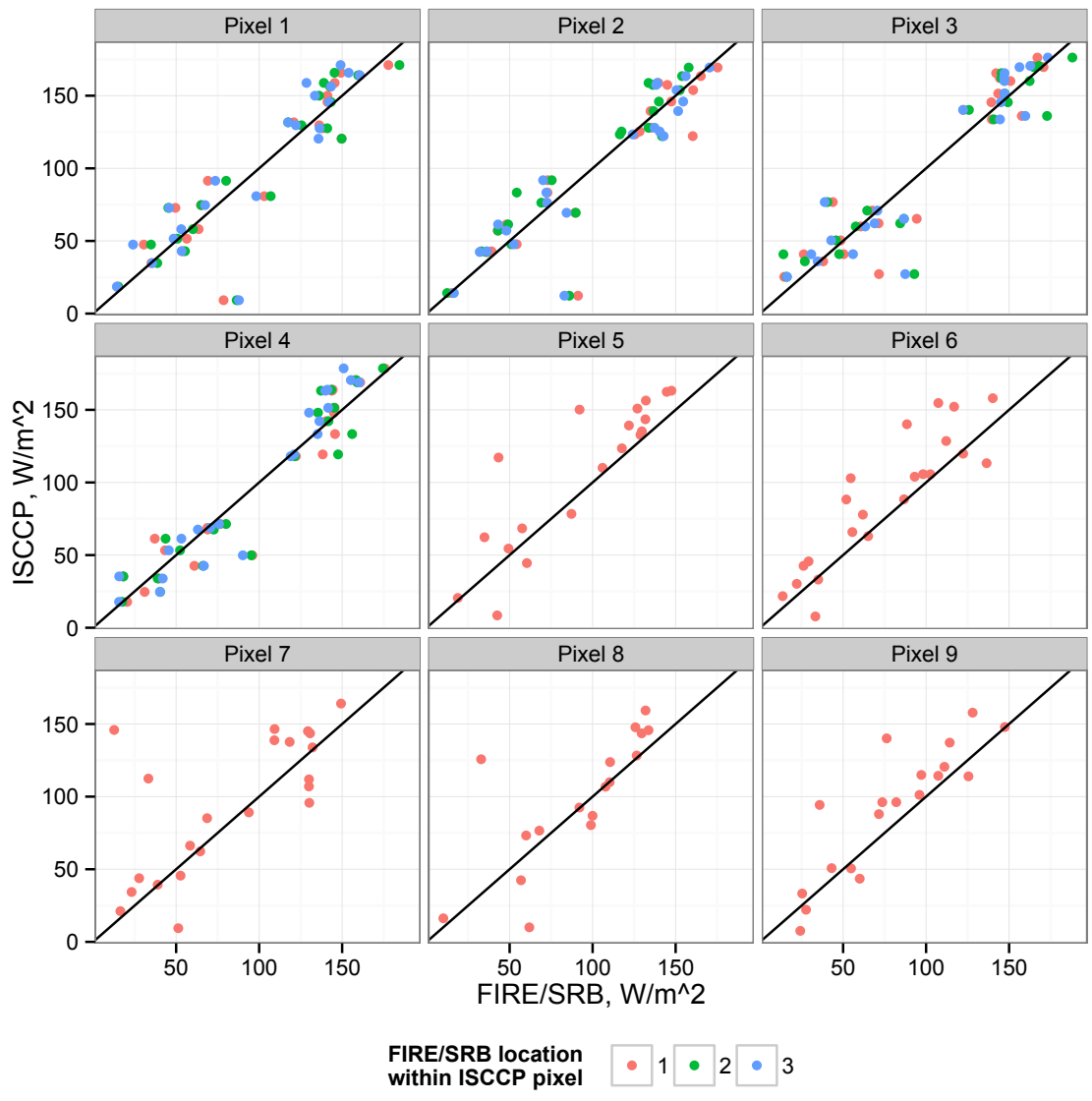


Figure 2.10: The FIRE/SRB data set is plotted against the ISCCP data at each corresponding location to show the correlation between the data sets.

Location	Correlation Coefficient	Mean Error	$\sigma_{error}$
Plain	0.92	0.9	20.5
Portage	0.69	-12.2	36.9
Tri-County	0.95	-1.7	17.4
Reedsburg	0.77	-6.6	28.9
Dodgeville	0.93	0.9	21.9
Mt. Horeb	0.87	-12.1	21.7
Arena	0.96	-0.2	15.6
Sauk City	0.91	3.0	21.3
Middleton	0.94	-0.8	19.5
Madison (Truax)	0.91	-3.0	20.9
Ft. McCoy	0.92	1.3	19.7
Stevens Point	0.91	0.9	22.5
Baraboo	0.95	1.5	17.5
Adams County	0.96	-3.4	16.1
Wautoma	0.88	-13.1	23.8
Wausau	0.89	-13.5	20.5
Arlington	0.91	-3.6	22.5

Table 2.5: FIRE/SRB Locations. List of seventeen site locations for data collection during the FIRE/SRB experiment

The FIRE/SRB data set provides a unique opportunity to compare multiple ground-based locations against a single ISCCP computed irradiance set, allowing us to determine if locational effects are important in correlating the computed and ground-based data. Ground-based values are collected from a single point location, whereas the satellite values are sub-sampled from a data set of finer resolution. The satellite instruments have a resolution greater than the  $0.5^\circ$  resolution of the DX data, however the data from each satellite has been randomly sub-sampled to provide the DX data [51]. As such, the exact location that is being reported may change with time.

The four pixels containing multiple FIRE/SRB locations are further examined to analyze potential differences in the correlation of all data within a pixel compared to correlations for each individual FIRE/SRB location. Table 2.6 shows for each ISCCP pixel the correlations between individual FIRE/SRB data sets and the corresponding

ISCCP irradiance values, as well as the correlation of all data within a single pixel.

Pixel	Individual Correlation	Pixel Correlation
Plain	0.92	0.91
Stevens Point	0.91	
Arlington	0.91	
Sauk City	0.91	0.91
Madison (Truax)	0.91	
Ft. McCoy	0.92	
Tri-County	0.95	0.94
Dodgeville	0.93	
Middleton	0.94	
Arena	0.96	0.96
Baraboo	0.95	
Adams County	0.96	

Table 2.6: Correlation of FIRE/SRB data compared to each location and the correlation of all data within each ISCCP pixel area.

For each pixel, one of the FIRE/SRB locations has a higher correlation than the other locations, and also higher than the overall correlation. However, according to a paired t-test there was no statistically significant difference between any of the individual FIRE/SRB locations and the ISCCP data for any of the pixels containing multiple FIRE/SRB locations. This is consistent with random sub-sampling of the data from a higher resolution dataset. The overall correlation is approximately an average of the correlations of each individual data set, as might be expected.

### 2.3.4 BSRN

The Base-line Surface Radiation Network (BSRN) is part of the World Radiation Monitoring Center, which has been archiving solar radiation values beginning in 1992 and continuing through today. It is a part of the Data Assimilation Panel from the Global Energy and Water Cycle Experiment, with a goal of monitoring changes in surface radiation and potential effects of climate change. Stations are distributed throughout the globe collecting data, the earliest began in 1992 with

stations entering or leaving the database each year. There are 46 stations that overlap in time with the ISCCP DX data set [118]. These data provide continuous, long time series measurements covering a wide range of geographical areas and surface types. Collectively this data set provides an ideal long-term comparison for the global irradiance values as computed from the ISCCP data.

The locations used for comparison can be seen in Fig. 2.11. The exact latitude and longitude of each location as well as the dates for which that location reported data can be seen in Table 2.7

For each location I compared the twenty-four hour averaged surface irradiance values between the BSRN and computed data from the ISCCP to validate the computational methods used. The correlation between the measured and the computed irradiance values was computed for each BSRN location. Due to the long time series

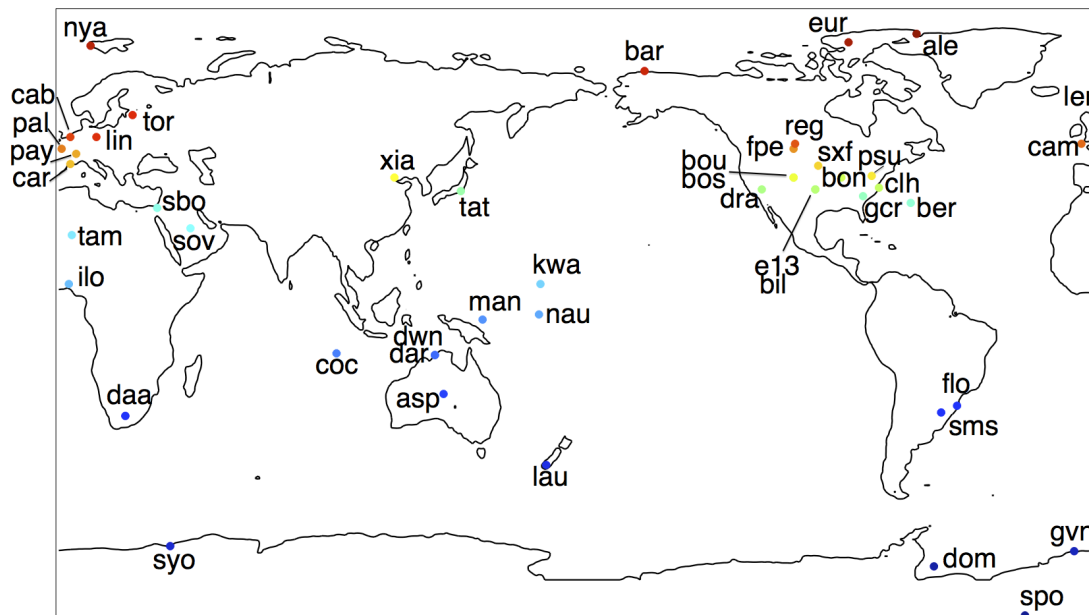


Figure 2.11: Each location is labeled with their 3-letter code assigned by the BSRN [118]. These locations were used for comparison with the ISCCP derived values. As can be seen the locations represent a wide variety of environments and locations across the planet.

Table 2.7: BSRN location information, including latitude and longitude of the collection site, dates for the beginning and ending of the overlap between the BSRN collection and ISCCP DX data set, as well as the number of days in the time series. The locations are ordered by latitude.

BSRN Code	Latitude	Longitude	Start Date	End Date	Number of Points
ale	82.49	-62.42	2004-08-17	2008-06-29	1373
eur	79.98	-85.93	2007-09-02	2008-06-29	302
nya	78.93	11.95	1992-08-02	2008-06-29	5703
bar	71.32	-156.61	1992-01-01	1994-12-31	1056
ler	60.13	-1.18	2001-01-01	2007-04-30	2240
tor	58.25	26.46	1999-04-06	2008-06-29	3364
lin	52.21	14.12	1994-10-01	2007-02-28	4484
cab	51.97	4.93	2005-02-01	2008-06-29	1192
cam	50.22	-5.32	2001-01-01	2007-06-30	2338
reg	50.21	-104.71	1995-01-01	2008-06-29	4746
pal	48.71	2.21	2005-10-01	2007-08-31	673
fpe	48.31	-105.10	1995-01-28	2008-06-29	4402
pay	46.82	6.94	1992-10-01	2008-06-29	5615
car	44.08	5.06	1996-09-01	2008-06-29	4188
sxf	43.73	-96.62	2003-06-16	2008-06-29	1630
psu	40.72	-77.93	1998-06-29	2008-06-29	3353
bos	40.13	-105.24	1995-08-01	2008-06-29	4418
bon	40.06	-88.37	1995-01-01	2008-06-29	4472
bou	40.05	-105.01	1992-01-07	2008-06-29	5653
xia	39.75	116.96	2005-01-01	2008-06-29	1265
clh	36.91	-75.71	2000-05-01	2008-06-29	2578
dra	36.63	-116.02	1998-03-17	2008-06-17	3377
e13	36.61	-97.49	1994-01-12	2008-06-29	4773
bil	36.61	-97.52	1993-09-01	2008-06-29	5073
tat	36.05	140.13	1997-07-02	2008-06-29	3881
gcr	34.25	-80.87	1995-01-01	2008-06-29	4724
ber	32.27	-64.67	1992-01-11	2008-06-29	5703
sbo	30.91	34.78	2003-01-01	2008-06-29	1791
sov	24.91	46.41	1998-09-14	2002-12-31	1491
tam	22.78	5.51	2000-03-08	2008-06-29	2942
kwa	8.72	167.73	1992-04-23	2008-06-29	5691
ilo	8.53	4.57	1992-09-01	2005-07-12	3708
nau	-0.52	166.92	1998-11-01	2008-06-29	3407
man	-2.06	147.43	1996-10-10	2008-06-29	4132
coc	-12.19	96.84	2004-10-04	2008-06-29	983

Continued on next page



**Table 2.7 – continued from previous page**

BSRN Code	Latitude	Longitude	Start Date	End Date	Number of Points
dwn	-12.42	130.89	2008-01-03	2008-06-29	179
dar	-12.43	130.89	2002-03-15	2008-06-29	2281
asp	-23.80	133.89	1995-01-01	2008-06-29	4667
flo	-27.53	-48.52	1994-07-01	1999-08-31	1552
sms	-29.42	-53.82	2006-04-01	2008-03-31	731
daa	-30.67	23.99	2000-06-01	2005-01-31	1476
lau	-45.04	169.69	1999-08-11	2008-06-28	3140
syo	-69.01	39.59	1994-01-01	2008-06-29	4887
gyn	-70.65	-8.25	1992-04-01	2008-06-29	5609
dom	-75.10	-56.62	2006-01-11	2008-06-29	773
spo	-89.98	-24.80	1992-01-01	2008-06-29	5702

provided by the BSRN data set, I was able to compare both 24-hour averages as well as monthly averages. Monthly averages help to show whether or not the computed irradiance values tend to compare well over longer time periods and if they follow the same trends as the ground-based sources. Figures 2.12 and 2.13 show the BSRN data plotted against the ISCCP irradiances for 24 and 672 hour averages (i.e. day and month), respectively.

As can be seen, when averages are taken over longer time periods the derived and ground-based data converge, showing much closer correlation at monthly averages than at daily averages. Table 2.8 shows the correlations for each location for daily, weekly, and monthly averages. Daily correlations range from 0.66 to 0.97, with only 4 locations lower than 0.80. For monthly averages range from 0.62 to 1.00, with only a single location with a correlation less than 0.90.

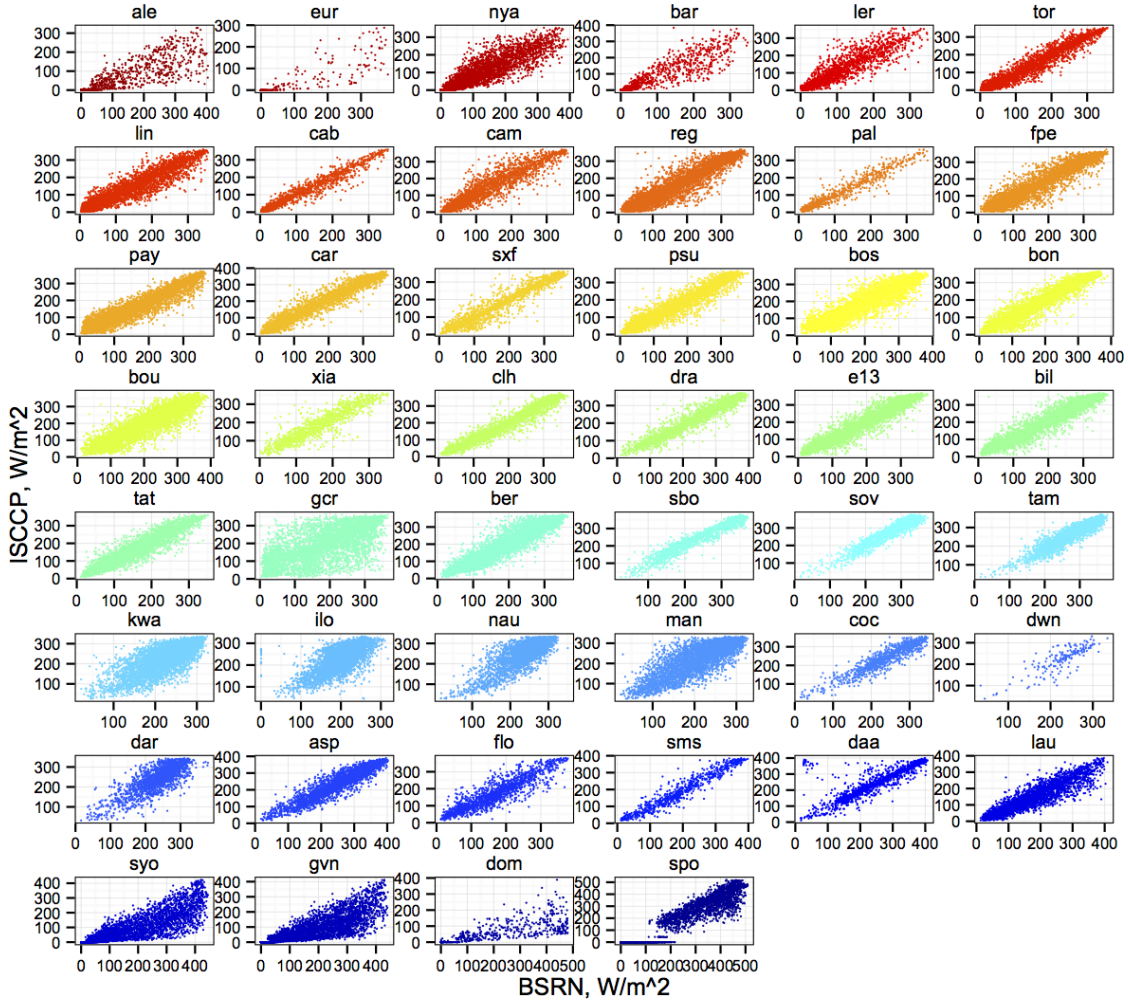


Figure 2.12: Reconstructed values on the vertical axis against ground level measurements from the Baseline Radiation Network. The locations are ordered, and color coded, according to their latitude with dark red being the North pole and dark blue the South pole. The results compare well except over locations with ice cover. This phenomena has previously been observed and results from satellite measurements making inaccurate measurements of cloud cover over ice [112].

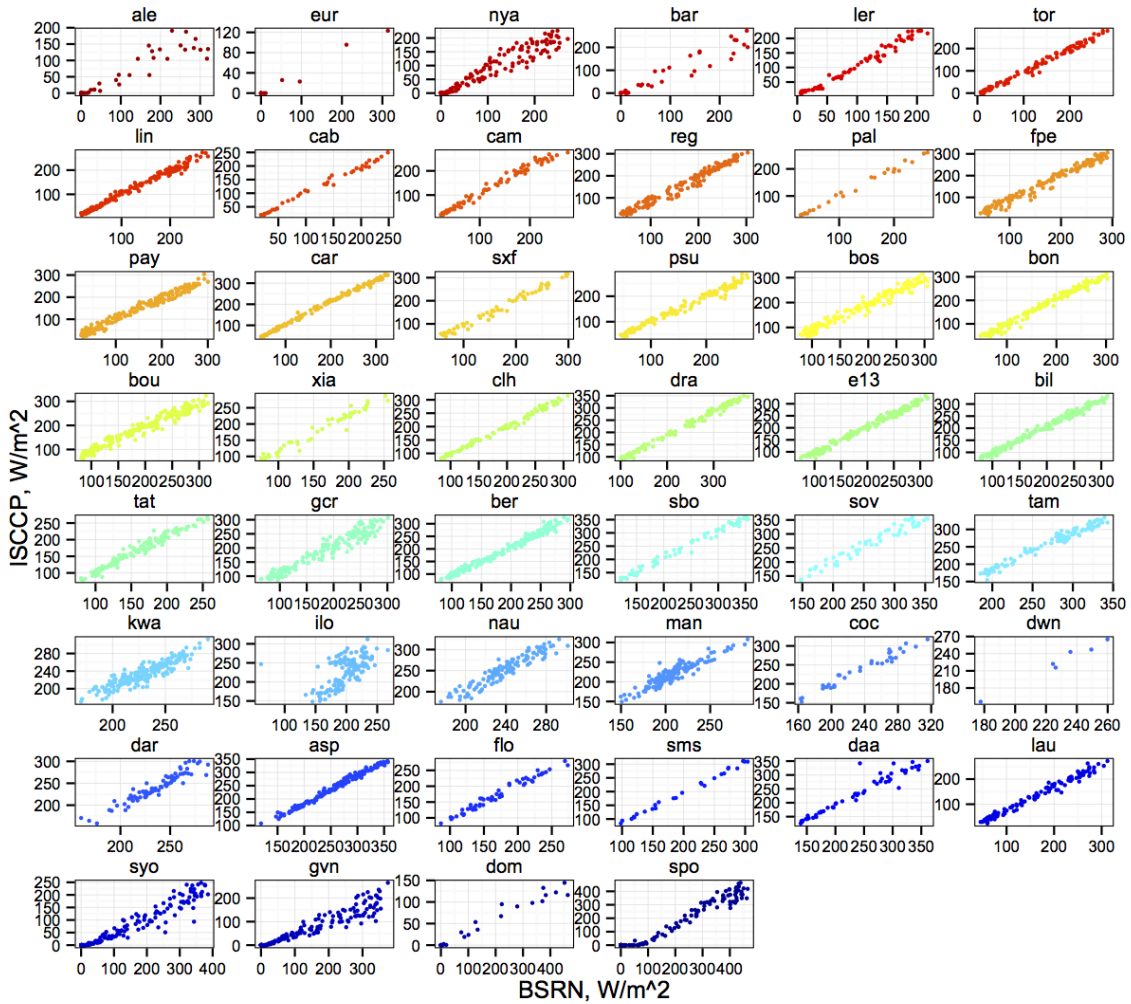


Figure 2.13: Reconstructed values on the vertical axis against ground level measurements from the Baseline Radiation Network. The locations are ordered, and color coded, according to their latitude with dark red being the North pole and dark blue the South pole. As with the 24 hour average, the results here compare well except over locations with ice cover.

Table 2.8: Correlations for each BSRN location compared to the ISCCP computed irradiance. Correlations were performed for daily, weekly, and monthly averages of irradiance values.

<b>BSRN Code</b>	<b>Daily Correlation</b>	<b>Weekly Correlation</b>	<b>Monthly Correlation</b>
ale	0.86	0.92	0.94
eur	0.85	0.94	0.99
nya	0.92	0.96	0.97
bar	0.90	0.94	0.96
ler	0.92	0.98	0.99
tor	0.97	0.99	0.99
lin	0.94	0.99	0.99
cab	0.96	0.99	1.00
cam	0.93	0.98	0.99
reg	0.93	0.97	0.99
pal	0.96	0.99	1.00
fpe	0.94	0.98	0.99
pay	0.95	0.98	0.99
car	0.97	0.99	1.00
sxf	0.94	0.98	0.99
psu	0.95	0.98	0.99
bos	0.89	0.96	0.98
bon	0.95	0.98	0.99
bou	0.90	0.96	0.98
xia	0.90	0.95	0.98
clh	0.96	0.99	1.00
dra	0.97	0.99	1.00
e13	0.96	0.99	0.99
bil	0.96	0.99	0.99
tat	0.93	0.97	0.98
gcr	0.66	0.89	0.97
ber	0.93	0.98	0.99
sbo	0.97	0.99	0.99
sov	0.95	0.97	0.97
tam	0.93	0.97	0.98
kwa	0.77	0.89	0.90
ilo	0.65	0.62	0.62
nau	0.82	0.92	0.95
man	0.81	0.90	0.93
coc	0.92	0.97	0.98
dwn	0.83	0.92	0.99

Continued on next page

**Table 2.8 – continued from previous page**

<b>BSRN Code</b>	<b>Daily Correlation</b>	<b>Weekly Correlation</b>	<b>Monthly Correlation</b>
dar	0.80	0.91	0.95
asp	0.95	0.98	0.99
flo	0.90	0.96	0.99
sms	0.96	0.99	1.00
daa	0.85	0.89	0.96
lau	0.92	0.98	0.99
syo	0.87	0.95	0.96
gyn	0.87	0.94	0.96
dom	0.79	0.93	0.98
spo	0.96	0.97	0.98

As noted above, the ISCCP DX data set is sub-sampled from a finer-resolution data set and is likely to not be the exact same location as the stationary ground-based data from BSRN sites. I would expect that over longer time periods the ISCCP data would provide a closer resemblance to a point location, both due to the random nature of the location observed by the satellite and also due to the random nature of weather patterns smoothing out as longer time periods are considered.

Importantly, Figs. 2.12 - 2.13 show that in locations where reconstructed and ground based measurements do not match well, the reconstructions underestimate surface irradiance, which results in conservative estimates for the performance of solar power facilities. The locations with the largest underestimates are all in icy locations near one of the poles. A known issue with the ISCCP data set includes polar, icy locations where reflection from the ice leads to overestimation of cloud-cover values [112], and therefore reduces the irradiance computed through my algorithm. This is consistent with the poor correlation noted in my analysis for polar locations of the BSRN data set, as well as the MLML data sets described in sub-section 2.3.2.

Figures 2.14 and 2.15 show histograms of the difference between computed and ground based measurements. As can be seen, the distributions are approximately symmetric about 0, indicating for the majority of locations tested, the derived data are equally likely to over predict as to under predict the surface irradiance. All non polar locations except for the location “daa” have a skewness value less than 1, indicating

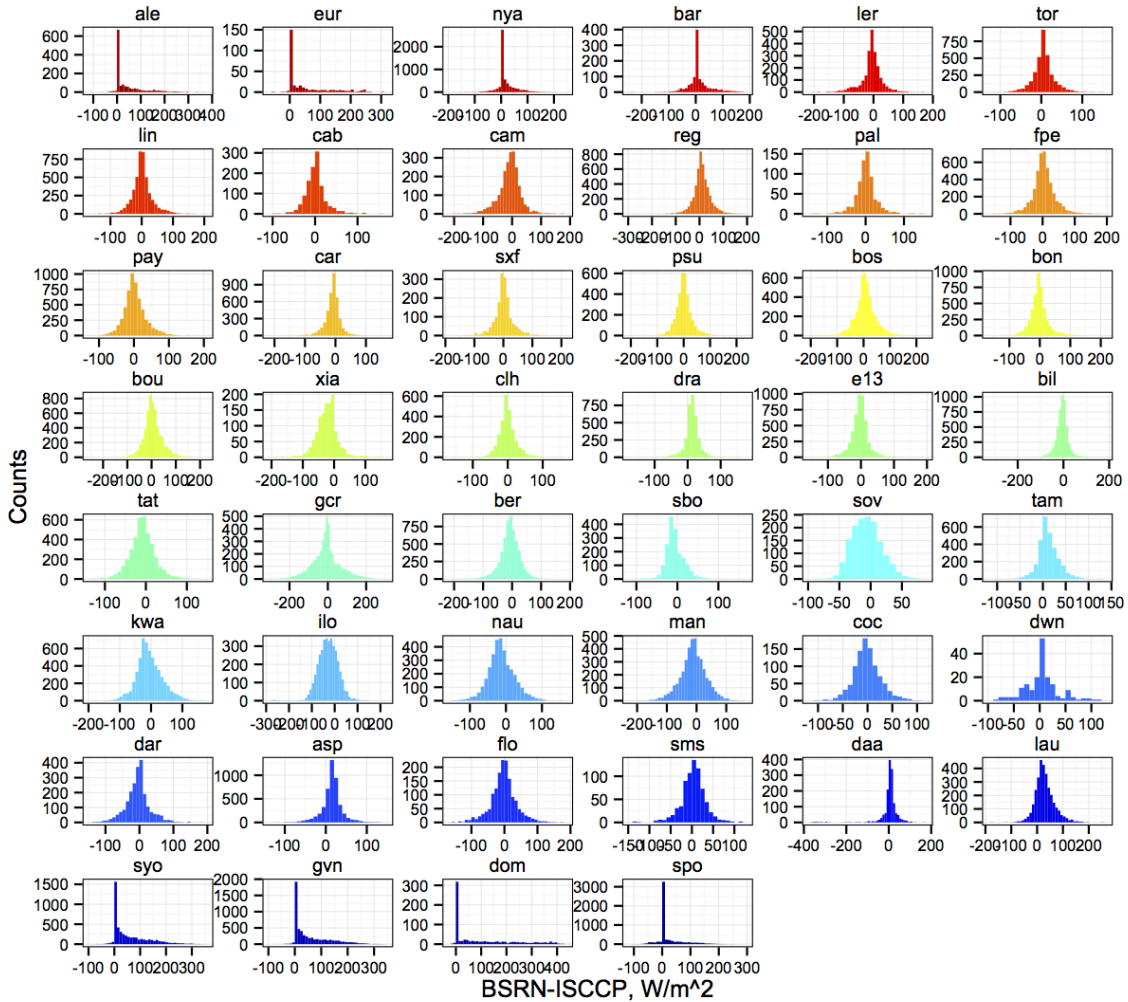


Figure 2.14: For each BSRN location, the irradiance measured at the surface was compared to the derived value. These differences were then plotted as a histogram. As can be seen, in almost all locations the distribution is symmetric about 0, the exceptions being at ice covered locations at or near the poles.

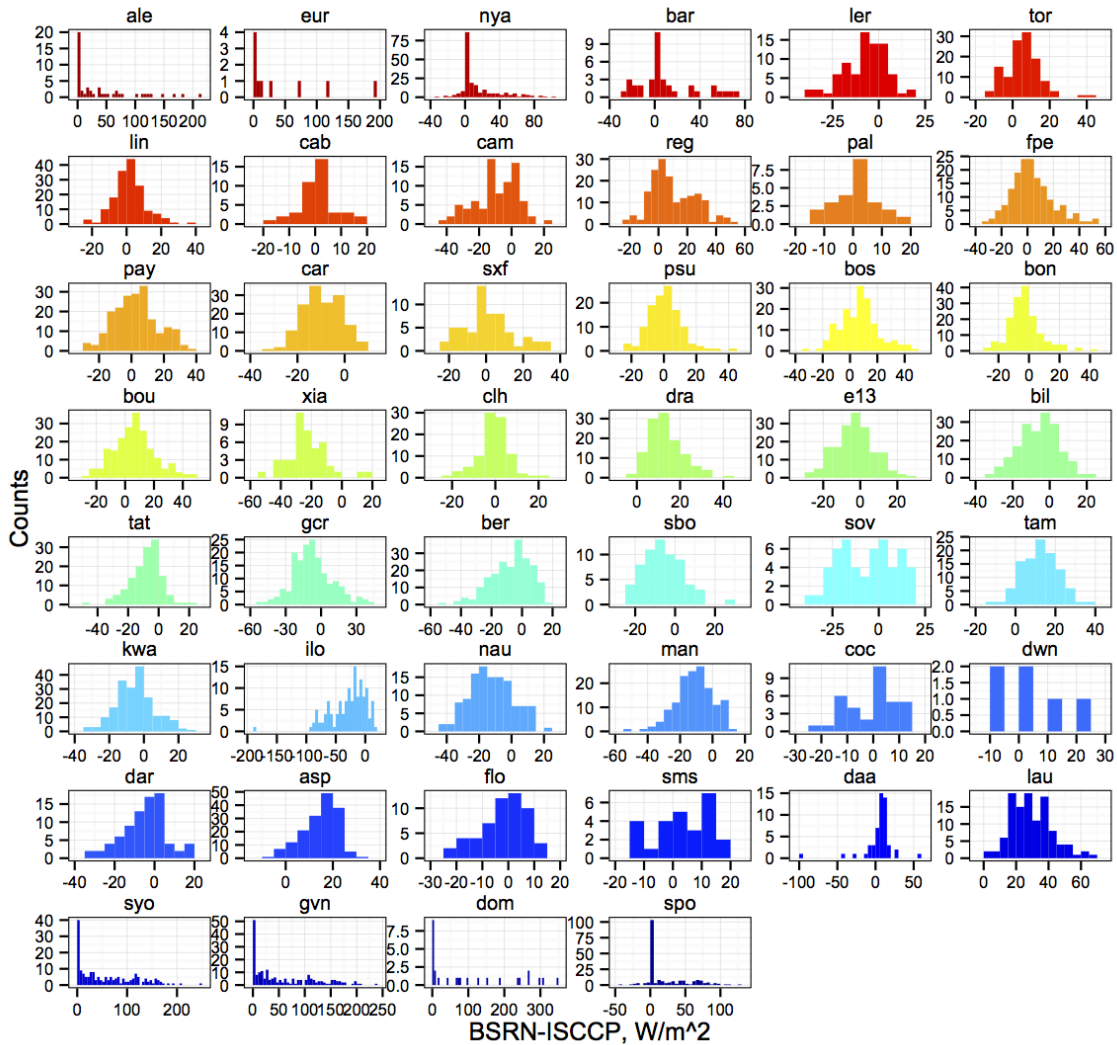


Figure 2.15: For each BSRN location, the irradiance measured at the surface was compared to the derived value. These differences were then plotted as a histogram. As can be seen, in almost all locations the distribution is symmetric about 0, the exceptions being at ice covered locations at or near the poles.

no significant skewness. This is important because over and under prediction can be expected to balance out over the 25 year data set. Again, this is not true for polar locations, where derived irradiances tend to under-predict measured values. However, these locations are not ideal for solar power due to extended periods with low or no irradiance during polar winters, and so are not of concern for subsequent analyses.

For non polar locations the mean error ranges from  $-28.2 W/m^2$  to  $29.6 W/m^2$ . Twenty-nine of the 38 non polar locations have a mean error of less than  $10 W/m^2$ , which is an average percent error of less than 8% of the average irradiance at all except for two of these locations. For these locations this error is 14% of the average irradiance.

## 2.4 Comparison of Transmission Formulation

The ISCCP instruments are calibrated to a specific wavelength,  $0.6 \mu m$ , and measurements of cloud optical thickness as well as other measured parameters are for this specific wavelength. However, surface solar irradiance values actually encompass a broad range of wavelengths. The analysis of solar irradiance presented in Sections 2.1 - 2.2 was re-performed with three modified wavelengths in order to identify the most accurate wavelength representation for ground-based measurements. The initial analysis was performed using a wavelength of  $0.78 \mu m$ .

The specific wavelength used affects the irradiance value through the transmission through clouds, specifically  $A_s$  and  $A_z$  in Equation (2.4). Both variables are functions of wavelength and cloud optical thickness. The details of the computation of  $A_s$  and  $A_z$  can be seen in [113]. In particular, the phase function, which determines the direction light scatters, is affected by the wavelength of incident radiation, Figure 2.16, which then impacts the total transmission through a cloud.

Three different approaches were investigated to determine the optimal wavelength to compute  $A_s$  and  $A_z$ . These included use of a different single wavelength value, calculating irradiance values using a range of wavelengths and averaging these values over the solar spectrum, and computing band-averaged transmission values for use in the irradiance computation. For each approach, I compared the new and original



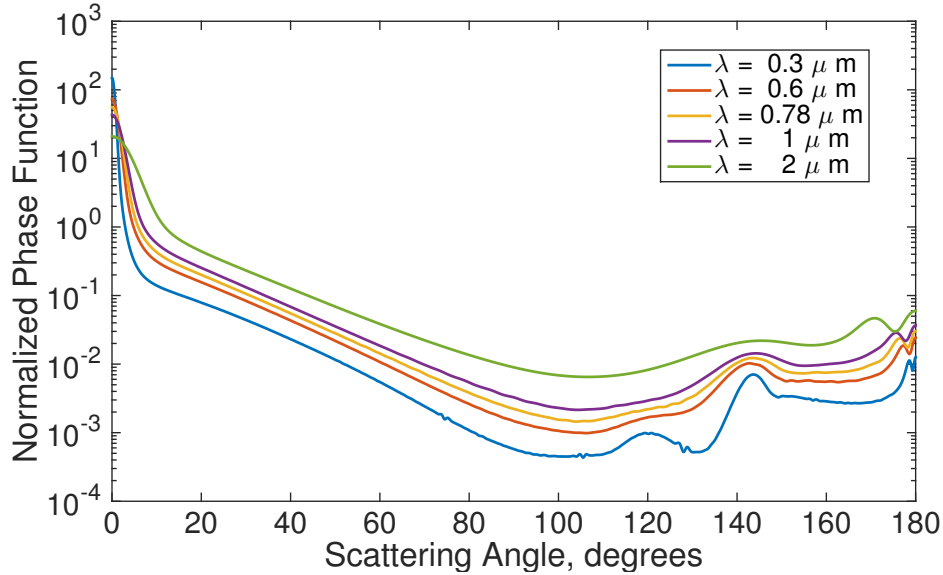


Figure 2.16: The phase function is shown here for several incident wavelengths. In particular, the phase function is computed for the wavelength used in the initial analysis,  $0.78 \mu m$ , the wavelength used to calibrate the ISCCP instruments,  $0.6 \mu m$ , and several additional wavelengths used in the wavelength averaged irradiance calculation.

irradiance values at the locations of the 46 BSRN sites reported in sub-section 2.3.4 for consistency with previous analysis.

#### 2.4.1 Single value, $0.6 \mu m$

First, a second single value,  $0.6 \mu m$ , was used to compute the transmission values. This value was chosen as it is the wavelength used to calibrate the ISCCP instruments [51]. As such, this wavelength will be the most accurate wavelength for the reported cloud optical thicknesses measurements.

The results for this wavelength are not statistically different from those of the  $0.78 \mu m$  results. I calculated the average difference between irradiance values computed with  $0.6 \mu m$  and  $0.78 \mu m$  wavelengths, as  $I(0.6\mu m) - I(0.78\mu m)$ . The difference ranged from  $-3.6 W/m^2$  to  $0.99 W/m^2$ . Figure 2.17 shows a histogram of the average difference between irradiance values for each compared site.

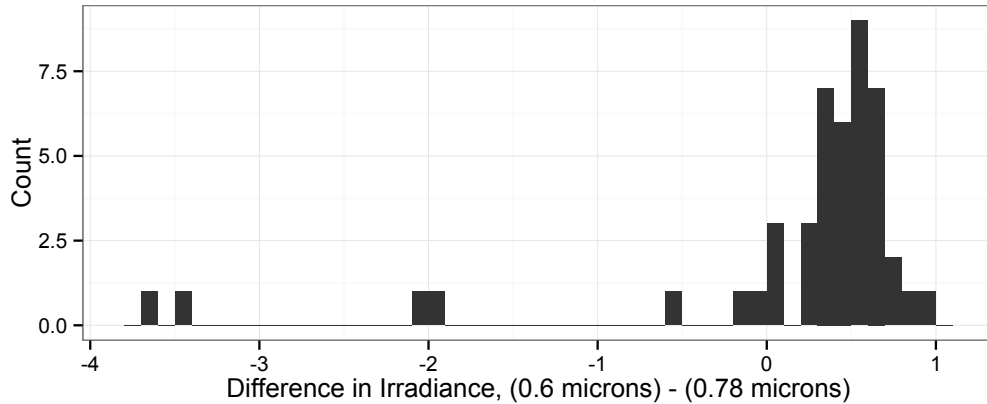


Figure 2.17: Difference in irradiance values as measured as  $0.6 \mu m - 0.78 \mu m$ , in  $W/m^2$ .

A paired t-test was performed on the 24-hour average irradiance values computed with  $0.6 \mu m$  and  $0.78 \mu m$  wavelengths. This test had a null hypothesis of the difference in means not being equal, and I was not able to reject this null hypothesis with a p-value of 0.17.

#### 2.4.2 Integration over Wavelength

The second test to determine an ideal wavelength was to compute an averaged irradiance, utilizing wavelengths over the entire solar spectrum. Such an analysis takes into account the impact of all wavelengths reaching the earth's surface. For this analysis,  $A_s$  and  $A_z$  were calculated at 35 wavelengths between  $0.3 \mu m$  and  $2.695 \mu m$ , and were then used to compute 35 separate irradiance data sets. These computed irradiance values were averaged over the solar spectrum, Fig. 2.18, as

$$IR_{avg} = \frac{\int_{\lambda_1}^{\lambda_2} IR_{\lambda} S_{\lambda} d\lambda}{\int_{\lambda_1}^{\lambda_2} S_{\lambda} d\lambda} \quad (2.8)$$

where  $IR_{\lambda}$  is the irradiance computed at a particular wavelength,  $S_{\lambda}$  is the fraction of solar radiation reaching the earth's surface at that wavelength, and  $IR_{avg}$  is the averaged irradiance value.

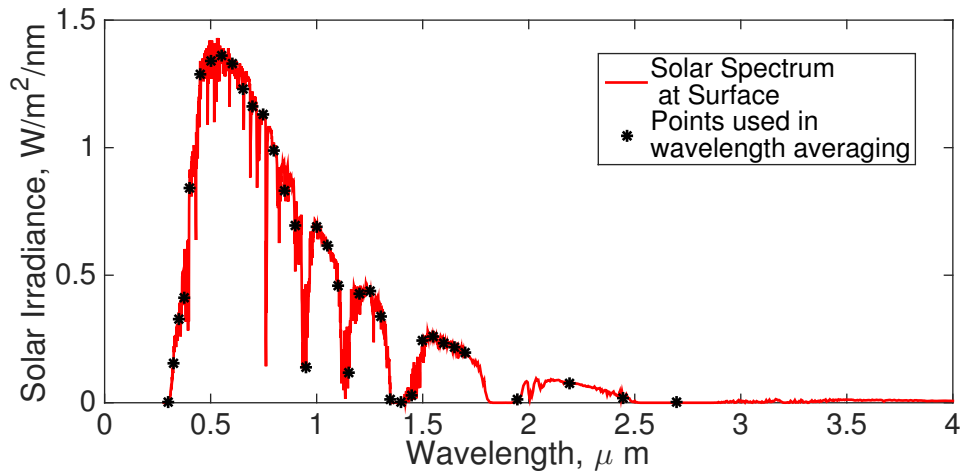


Figure 2.18: Surface solar irradiance values for wavelengths in the range  $0.28 \mu\text{m}$  to  $4.0 \mu\text{m}$ . The stars indicate wavelengths used to compute the wavelength-averaged irradiance values.

The differences between the wavelength-averaged irradiance values and the original irradiance values ranged from  $-3.9 \text{ W/m}^2$  to  $-0.12 \text{ W/m}^2$ . Figure 2.19 shows a histogram of the average difference between irradiance data sets for each of the locations of the BSRN, subsection 2.3.4.

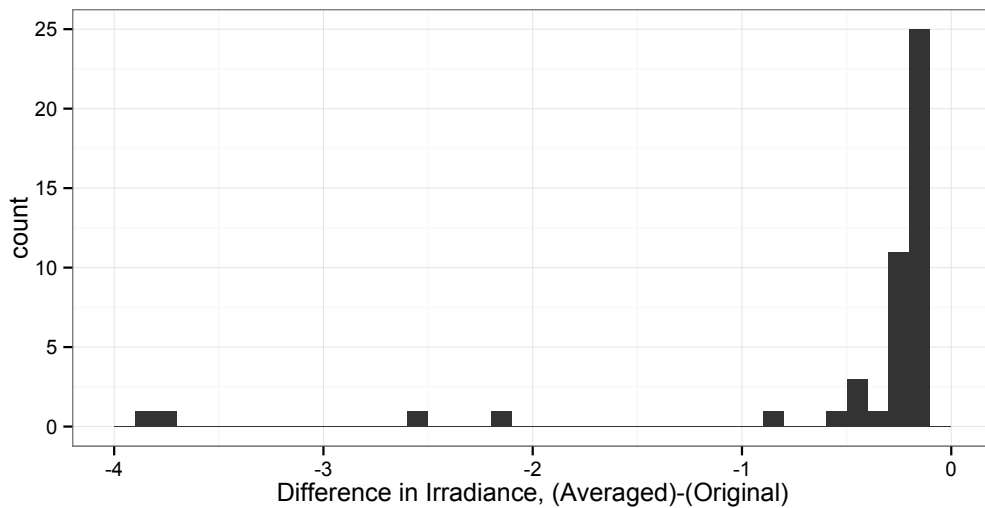


Figure 2.19: Difference in irradiance values as measured as (irradiance averaged over the solar spectrum) - (original), in  $\text{W/m}^2$ . Differences reported for each of the 46 BSRN locations described in sub-section 2.3.4

A paired t-test was performed on the 24-hour averages of the wavelength-averaged and original data sets. This test had a null hypothesis of the difference in means not equal to 0. I was able to reject this null hypothesis with a p-value less than 0.01. I also tested the difference in correlation coefficients between the measured irradiances at each of the 46 BSRN locations and either the wavelength-averaged or original ISCCP data with a wilcoxon signed rank test. This test was also significant at a p-value less than 0.01. However, the irradiance computed with averaged wavelengths has a lower correlation than the original data. The range of the difference between the correlations of BSRN data and wavelength averaged data or data computed with a wavelength of  $0.78 \mu m$  was -0.01 to 0.003.

## 2.5 Visibility Correction

I next investigating improving the algorithm presented in [54] by incorporating ground-based visibility measurements from the Integrated Surface Database produced by the National Climatic Data Center (NCDC). This data set includes visibility measurements taken from approximately 10,000 weather stations world-wide [119]. These stations include both land-based data collection stations and also ships collecting data during their voyages. The stations provide surface visibility measurements at time intervals ranging from one to twenty-four hours; where multiple stations or time points exist for each time and pixel location of the ISCCP data, the NCDC data were averaged. Figure 2.20 shows one time point of visibility data, for December 1, 1986, 0000 GMT. At this time point, there were 6162 locations reporting visibility values.

Where the NCDC values exist, I used the reported values for visibility measurements. Where no NCDC data exists, I continued to assume a constant visibility of 25 km as in [54]. In order to determine the impact of visibility on the computed irradiance

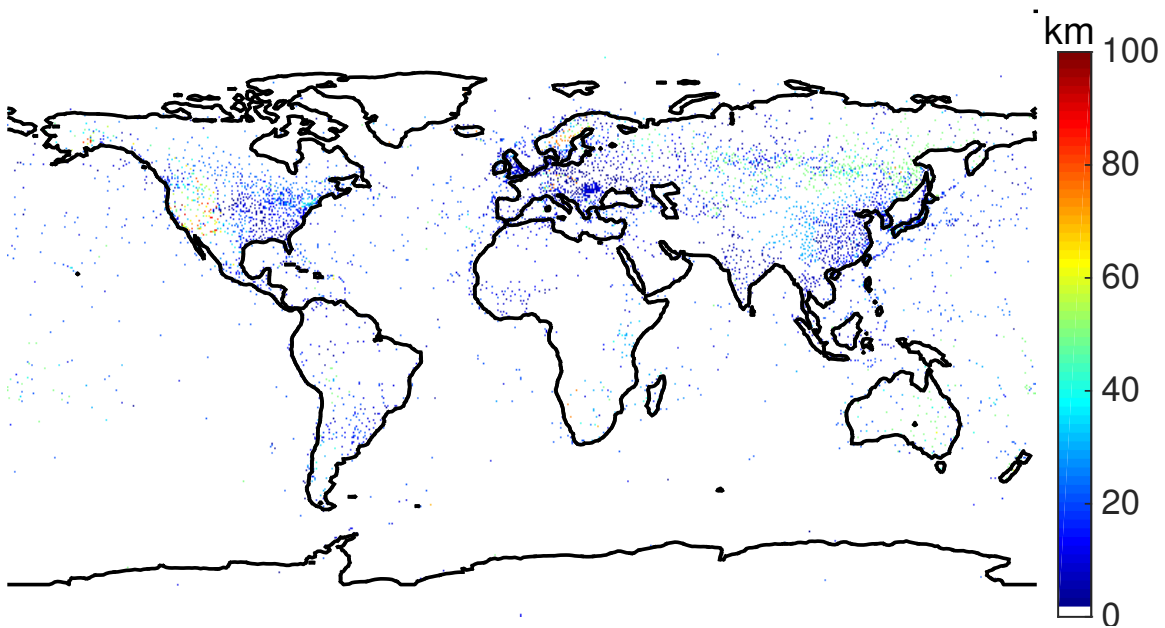


Figure 2.20: Visibility measurements, in kilometers, from 6179 stations of the National Climatic Data Center. Using NCDC data, I incorporated visibility at all locations for which there was available data. This map shows one time point of visibility data, for December 1, 1986 at 0000 GMT.

values, I compared the error with respect to ground-based measurements for locations with reported visibility measurements and locations without visibility measurements. This was done for each of the ground-based data sets described in Section 2.3. For these comparisons, hourly irradiance values were used instead of 24-hour averages to more directly compare the effect of incorporating visibility measurements.

### 2.5.1 Biowatt II

The Biowatt experiment had minimal overlap with the NCDC data set, largely because visibility data were only available if ships traveled near the experiment. There were 15, 27, and 18 hours that had visibility measurements for the first, second, and third Biowatt experiments, respectively. These experiments had 1689, 2565, and 1950 hours without visibility measurements, respectively. Table 2.9 shows the correlation coefficient and mean error for locations with and without visibility measurements for

each Biowatt experiment.

<b>Set 1</b>			
Visibility	Correlation Coefficient	Mean Error	$\sigma_{error}$
No	0.94	-3.5	104.2
Yes	0.88	51.2	101.2
<b>Set 2</b>			
Visibility	Correlation Coefficient	Mean Error	$\sigma_{error}$
No	0.96	-3.0	99.3
Yes	0.99	-30.8	65.9
<b>Set 3</b>			
Visibility	Correlation Coefficient	Mean Error	$\sigma_{error}$
No	0.94	3.0	78.3
Yes	0.96	-9.8	59.2

Table 2.9: Correlation and error measurements for the Biowatt data set for time points with and without corresponding visibility measurements from the NCDC data set. There were 15 hours in which the first data set had visibility measurements, 27 hours in which the second data set had visibility measurements, and 18 hours in which the third data set had visibility measurements.

The absolute value of the mean error increased in all cases, indicating that inclusion of the visibility values did not improve the irradiance computation. A Wilcoxon rank sum test was performed on the error between values with and without visibility measurements with a null hypothesis that the populations were the same. This test was used instead of a student’s t-test because the populations are not normally distributed. The test was found to be significant for only the second Biowatt experiment, with a p-value of 0.01. The p-value of the test for the first Biowatt data set was 0.06, and for the third data set was 0.51. Figure 2.21 shows a density plot of the error values for each of the three experiments.

### 2.5.2 MLML

The MLML data set also had minimal overlap with the NCDC data set, for similar reasons. For the first MLML experiment, 24 of the hourly irradiance

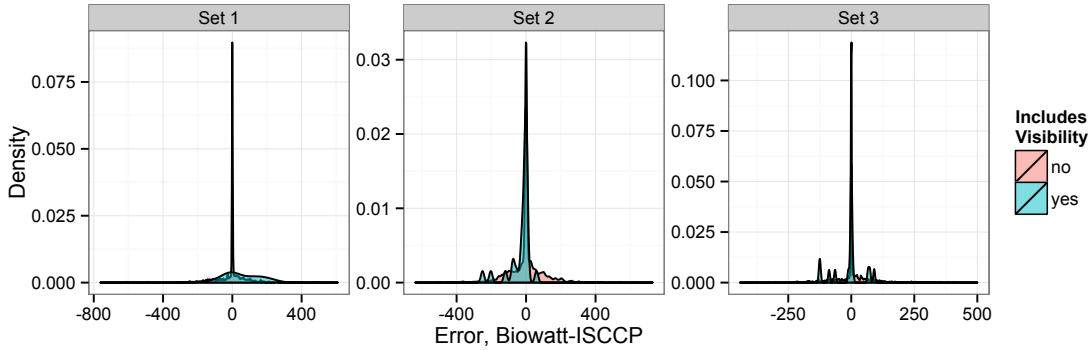


Figure 2.21: Density plot of the error between the Biowatt data set and computed ISCCP values, comparing hourly time points with and without visibility data in the NCDC data set. There was a significant difference between these data sets only for the second experiment.

values had a corresponding visibility measurement, compared to 1344 hours without a visibility measurement. The second MLML experiment had 39 hours with visibility measurements and 3009 hours without visibility measurements. Table 2.10 shows the mean error between the MLML and ISCCP hourly data and the correlation between the MLML and ISCCP data for each of the MLML experiments.

Set 1, 1989			
Visibility	Correlation Coefficient	Mean Error	$\sigma_{error}$
No	0.89	27.3	98.3
Yes	0.88	28.5	80.9
Set 2, 1991			
Visibility	Correlation Coefficient	Mean Error	$\sigma_{error}$
No	0.92	4.4	84.4
Yes	0.92	36.2	93.5

Table 2.10: Correlation and error measurements for the MLML data set for time points which did and did not have corresponding visibility measurements from the NCDC data set. There were 24 hours in which the first data set had visibility measurements and 39 hours in which the second data set had visibility measurements.

Again a Wilcoxon rank sum test was performed on the error between values with visibility measurements and values without visibility measurements. The test showed no significant difference for either data set. The first data set had a p-value of

0.36 and the second data set had a p-value of 0.66. Figure 2.22 shows a density plot of the error as MLML-ISCCP irradiance values, colored based on if the data included or did not include visibility measurements from the NCDC database.

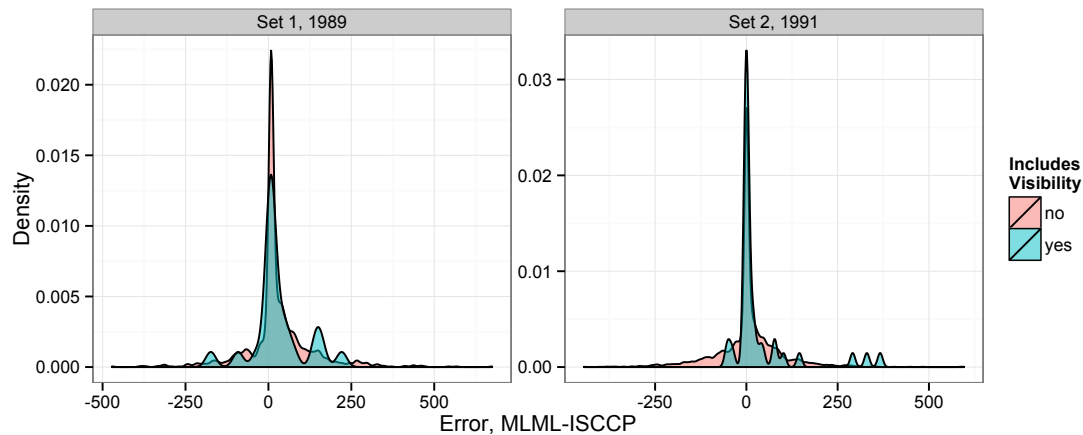


Figure 2.22: Density plot of the error between the MLML data set and computed ISCCP values, for hourly time points that do and do not include visibility data as from the NCDC data set. There was no significant difference between the error for locations that included visibility and those that did not.

### 2.5.3 FIRE/SRB

The FIRE/SRB experiment included a larger number of corresponding visibility data than the Biowatt or MLML data sets. Of the nine pixel locations, four had corresponding visibility data. Three pixels had visibility measurements for all hours and one pixel had visibility measurements for approximately half of the hours. Due to the clustering of FIRE/SRB locations within some pixels, 5 FIRE/SRB locations had complete visibility data, 3 FIRE/SRB locations had partial visibility data, and 9 FIRE/SRB locations had no visibility data.

A Wilcoxon rank sum test was performed for each of the 3 FIRE/SRB locations with partial visibility data. The test compared the error with respect to ground-based data between time points including or not including visibility. The error was computed



as FIRE/SRB irradiance - ISCCP irradiance. In each of these 3 instances the test showed a significant difference between the errors, each with a p-value less than 0.01. Figure 2.23 shows a density plot of the error values for each of the three locations and time points which do and do not include visibility data.

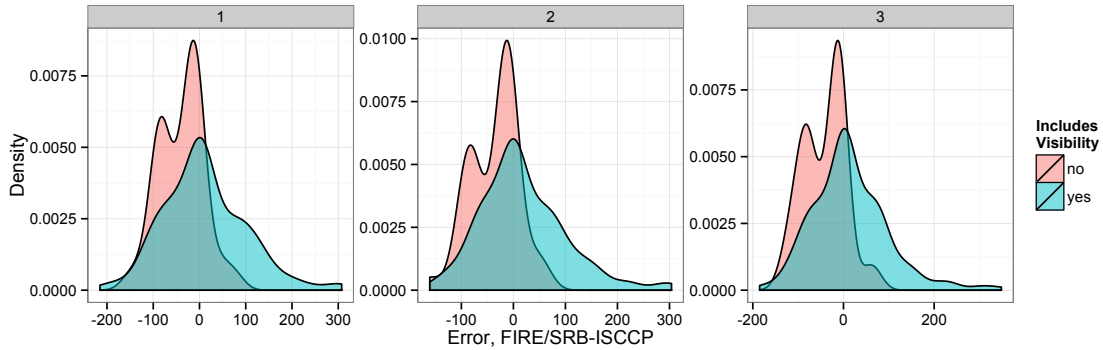


Figure 2.23: Density plot of the error between the FIRE/SRB data set and computed ISCCP values, showing a comparison between hourly time points that do and do not include visibility data from the NCDC data set. The figure shows three FIRE/SRB locations for which there was both time points with and without visibility measurements for a direct comparison. There was a significant difference between the error of time points with and without visibility measurements for all three locations as tested with a Wilcoxon rank sum test.

I also combined data from all locations of the FIRE/SRB experiment to further examine the impact of visibility measurements, as several locations either only had visibility data or only did not have visibility data and therefore could not be compared within their own data sets. The correlation between all the FIRE/SRB data and ISCCP data with visibility was 0.92, and the correlation between all data points without visibility was 0.91, Figure 2.24.

The mean error for all time points including visibility data was  $7.6 \text{ W/m}^2$  with a standard deviation of  $80.9 \text{ W/m}^2$ , and for all time points not including visibility data was  $-3.5 \text{ W/m}^2$  with a standard deviation of  $81.8 \text{ W/m}^2$ . These populations were found to be statistically different under a student's t-test, with a p-value less than 0.01.

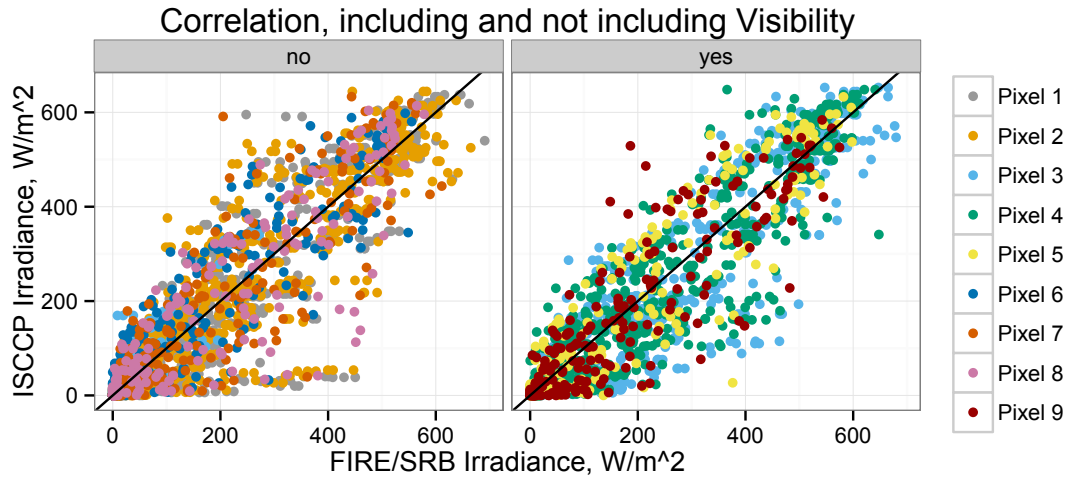


Figure 2.24: Correlation plot for data points including visibility measurements and not including visibility measurements. Data were combined for all locations in the FIRE/SRB experiment as most locations either fully included visibility measurements or had no visibility measurements.

The FIRE/SRB data set shows a less skewed error distribution for points that include measured visibility, with a skewness of 0.50, compared to a skewness of 0.70 for all points not including visibility measurements. The correlation between the data sets increases when including visibility, however the absolute value of the error also increases.

#### 2.5.4 BSRN

Thirty-one of the forty-six BSRN sites include time points with corresponding visibility data. Here I specifically compared time points during the daytime, as in some cases visibility was only reported during the day and never at night. This resulted in a correlation of 1 for time points without visibility, all of which reported an irradiance of 0. This was not useful for the current comparison.

Figure 2.25 shows density plots for 30 of the 31 locations that included hours both with and without visibility. This allows for direct comparison of visibility data at

the same locations. One location which had only 18 points with visibility measurements was excluded from the figure, however was included in subsequent analyses.

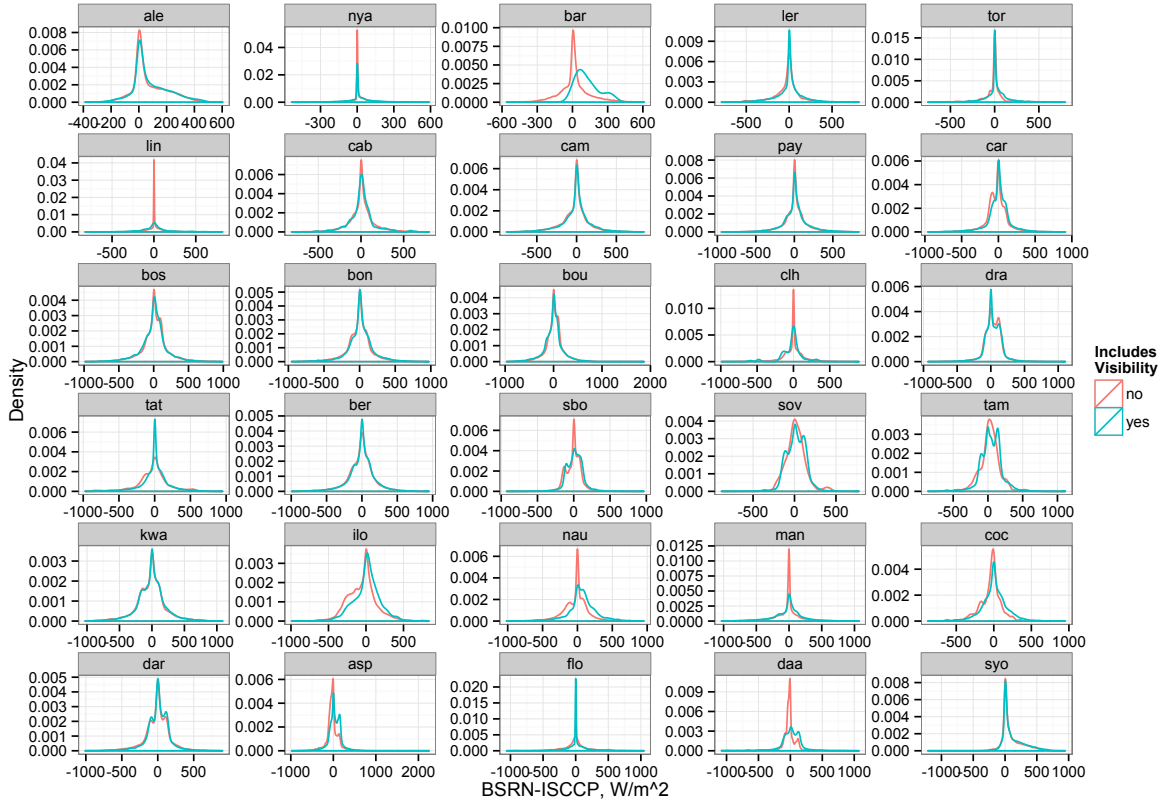


Figure 2.25: Density plot of the error between the BSRN data set and computed ISCCP values, showing a comparison between hourly time points that do and do not include visibility data from the NCDC data set. The figure shows comparisons for 30 locations for which there are time points both with and without visibility measurements.

The correlations for time points both with and without visibility data are shown in Table 2.11. A paired t-test was performed on the correlation values with and without visibility data for each location. There was no significant difference between these data sets with a p-value of 0.74. Table 2.11 also shows the mean error between the BSRN irradiance values and the computed irradiance values, both for time points including and not including visibility data. A Wilcoxon signed rank test was performed between the mean error with and without visibility measurements for

Table 2.11: Correlations for each BSRN location which have time points that include visibility measurements compared to the ISCCP computed irradiance values. Correlations were performed for both the time points at each location that had visibility measurements, as well as for locations without visibility measurements.

BSRN Code	Correlation w/o Visibility	Correlation w/ Visibility	Mean Error w/o Visibility	Mean Error w/ Visibility
ale	0.56	0.54	72.7	82.4
nya	0.71	0.68	16.9	22.5
bar	0.73	0.81	17.7	125.8
ler	0.73	0.66	-27.4	-2.3
tor	0.78	0.80	-1.9	14.2
lin	0.82	0.78	2.3	9.8
cab	0.77	0.75	2.9	8.2
cam	0.76	0.72	-20.9	-5.5
pay	0.80	0.75	5.4	14.4
car	0.86	0.85	-25.8	1.4
bos	0.78	0.80	14.3	3.8
bon	0.79	0.78	-5.5	12.9
bou	0.79	0.78	18.5	-6.3
clh	0.85	0.80	-1.9	-22.2
dra	0.91	0.91	32.5	31.4
tat	0.66	0.75	-24.6	6.1
ber	0.81	0.81	-15.3	-4.7
sbo	0.94	0.93	-6.6	16.5
sov	0.94	0.94	13.1	18.6
tam	0.90	0.90	27.7	46.5
kwa	0.77	0.78	-15.6	-4.9
ilo	0.81	0.81	-51.3	11.3
nau	0.86	0.81	-23.4	67.0
man	0.79	0.75	-26.0	-15.2
coc	0.88	0.87	-42.3	7.0
dwn	0.80	0.89	55.9	21.7
dar	0.86	0.88	-8.4	3.9
asp	0.89	0.90	-17.6	35.5
flo	0.69	0.81	6.3	6.9
daa	0.89	0.84	-19.0	6.6
syo	0.76	0.72	94.7	113.9

all locations, and found a significant difference with a p-value less than 0.01.

The inclusion of visibility data has a limited impact on improving the correlation between the computed irradiance values when compared to ground-based sources. In some locations the error between the two measurements improves, however there was not a consistent statistically significant improvement for including measured visibility data. There could be several reasons for this, in particular localized visibility effects. It is not known if the visibility data corresponds to the same location as the ground-based irradiance source or to the same location reported by the ISCCP satellites. In addition, the formula assumes the visibility is constant through the atmosphere, while the visibility values recorded in the NCDC data base are just at the surface and may only be applicable to the lower atmosphere.

## Chapter 3

# Coupling photovoltaics and grid-scale energy storage

Solar energy is typically used as a non-dispatchable resource, providing energy only during daylight hours, and even then being affected by cloud cover. There are only two options for compensating for this inherent variability: additional generating capacity, or a means by which to store excess capacity for use at times when output is low.

This chapter addresses the ability of a coupled utility scale photovoltaic array and energy storage facility to provide dispatchable power in the form of either constant base-load energy or output following a specific load curve. Primarily compressed air energy storage (CAES) is used for the storage facility, however above ground CAES and batteries are also considered.

### 3.1 Base-load Energy flow model

The energy flow model follows the energy provided by a solar photovoltaic array and a grid-scale energy storage facility. A schematic of the model components is shown in Fig. 3.1. This model, which operates on an hourly basis for the entire globe, follows basic flows of energy through the coupled system. For each location and hour, the model first determines the total output from the photovoltaic array, then determines how the energy will be used. Energy is first used to meet a predetermined baseload output with any additional energy stored up to the point at which the storage

facility is full. Energy unable to be stored is counted as excess. If there is not enough energy provided by the array to meet the baseload requirement, energy is taken out of the storage facility up to the point at which the storage facility is empty.

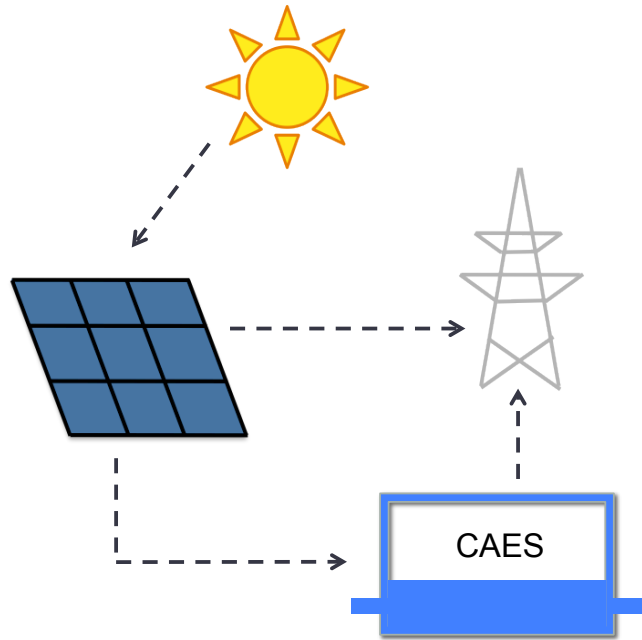


Figure 3.1: Energy is produced by the array, and sent either directly to the grid or to the storage facility depending on the energy requirements at a particular time and the charge level of the storage facility.

The coupled system is assumed to have a capacity of  $100 MW_e$  as a base-load system. Because this is a combined system with a battery requiring charging, the array must be sized such that the rated capacity of the array is greater than  $100 MW_e$ . However, in this report where the “system capacity” is referenced, capacity refers to the capacity of the coupled system, not the rated array capacity, which will be larger than  $100 MW_e$ .

The total output from the photovoltaic array is computed for each hour,  $i$ , as:

$$E_i = \frac{I(i) * (1 - R(t))}{1000 W_p/m^2} W_A \quad (3.1)$$

where  $E_i$  [J] is the energy produced in that hour,  $I(i)$  [W] is the surface solar irradiation at hour  $i$ ,  $W_A$  [ $W_p$ ] is the rated capacity of the array, and the factor of  $1000 W_p/m^2$  is a factor for determining the rated capacity for photovoltaic modules, used to standardize their ratings [120]. Equation. (3.1) is computed for the start of each hour of analysis, determining the energy available for that time step.

This analysis determines the array output using the rated array capacity,  $W_A$  instead of a specific array area. However, the size of the array may be calculated as

$$A = \frac{W_A}{\eta 1000 W_p/m^2} \quad (3.2)$$

where  $A$  is the array size [ $m^2$ ],  $\eta$  is the array efficiency, assumed to be 14% for this analysis as a conservative value for panels available to consumers [13]. This will be used to provide a general idea of the size required for the proposed systems, however the specific area would change if a different efficiency were used.

The energy produced by the array is partitioned into three components:

$$E_i = E_g + E_s + E_e \quad (3.3)$$

where  $E_g$  [J] is the energy sent directly to the local grid to meet base-load electricity needs and  $E_s$  [J] is the energy directed into storage. When the storage is full and the array is producing more than  $100MW_e$ , the excess electricity  $E_e$  [J] is available for broader use. Additionally, energy taken from the storage facility is accounted for as



$E_{fs}$  [J]. I calculate  $E_g$ ,  $E_s$ ,  $E_{fs}$  and  $E_e$  in each hour according to  $E_i$  as:

$$\begin{aligned}
E_g &= \begin{cases} 100 \text{ MWh} & E_i \geq 100 \text{ MWh} \\ E_i & E_i < 100 \text{ MWh} \end{cases} \\
E_{fs} &= \begin{cases} 0 \text{ MWh} & E_i \geq 100 \text{ MWh} \\ 100 - E_i & E_i < 100 \text{ MWh} \end{cases} \\
E_s &= E_i - 100 \text{ MWh} & E_i \geq 100 \text{ MWh}, \text{ storage not full} \\
E_e &= E_i - 100 \text{ MWh} & E_i \geq 100 \text{ MWh}, \text{ storage full}
\end{aligned} \tag{3.4}$$

The total energy in the storage facility is updated after every hour. Night-time hours are accounted for automatically because  $E_i$  is always zeros at these times. In such cases, all energy is taken from the storage facility. During daylight hours energy may be provided from both the array and storage facility or just from the array. If the storage facility does not have enough energy to provide  $E_{fs}$ , the total energy provided that hour will be less than 100  $MWh_e$ . The amount of energy in the storage facility is noted at the end of each simulated hour, as are  $E_g$ ,  $E_s$ ,  $E_e$ , and  $E_{fs}$ .

For all energy put into the storage facility, losses are accounted for through the energy ratio,  $ER$ . This quantity accounts for both the efficiency of the compressor and turbine and system losses as well as the fact that energy is added to preheat the air before it passes through the turbine. The addition of energy in the form of natural gas leads to the energy ratio being less than 1. Specifically, an  $ER$  of 0.73 is used for this analysis [47–49].

The total natural gas used per year is calculated from the total energy provided from the storage facility during its lifetime,  $E_{storage}$ , and the heat ratio,  $HR_{CAES}$  [ $MJ/MWh_e$ ], as

$$\text{fuel use} = HR_{CAES} * E_{Storage}/T_L \tag{3.5}$$

where  $E_{storage}$  [ $MWh_e$ ] is the sum of  $E_{fs}/ER$  for all hours of operation, and  $T_L$  is the lifetime of the system. This gives us an average amount of natural gas used by the

system each year, in  $MJ$ .

The model also computes a capacity factor for the coupled system for each year of operation. Given the definition of the system capacity as  $100MW_e$  of base-load capacity, the capacity factor is computed assuming  $100 MW_e$  output. The system is capable of providing more than  $100 MW_e$  due to the oversized array, however I assume that  $E_g + E_{fs} \leq 100MWh_e$  in each hour, as per Eq. 3.4, ignoring excess energy. The capacity factor is then defined as:

$$CF = \frac{\Sigma_{year}(E_g + E_{fs})}{876,000 MWh_e} \quad (3.6)$$

Any excess energy produced,  $E_e$ , would assumedly be used on the grid as traditional non-dispatchable solar power is used. During peak hours it would go towards meeting the peak demand, and during non-peak hours it would be used on the grid if traditional generators had sufficient flexibility to allow its use. If it were unable to be utilized by the grid this excess would be curtailed. If it is entirely curtailed due to lack of grid flexibility or other reasons, the operation of the coupled PV-CAES system would not be affected.

Providing energy with a capacity factor of 100% is unrealistic, as systems have unexpected failures and require maintenance. Nuclear power is a true base-load resource, as it does not load follow and is used at a constant output level. The U.S. nuclear fleet has a 5-year average capacity factor of 90.7% [121]. This value is used as a reference capacity factor for base-load sources, and sized the coupled system such that this capacity factor could be met in each year of the analysis. It should be noted that in traditional base-load generators, maintenance can be scheduled during off-peak times whereas with the current method maintenance would be required to be done during the winter time when solar irradiance is low. This may coincide to

periods of higher demand than would be seen during maintenance periods of traditional generators.

For the energy flow analysis, the size of the array and storage facility had to be determined. I determined the size of the array and storage facility such that the system had a capacity factor of  $0.907 \pm 0.001$ . I simplified the problem by fixing the storage capacity to 24 different values, and determined the array size required to reach the desired capacity factor for each of these storage sizes.

The storage sizes were determined based on the longest night at any particular location. There is no output from the array during the night-time, requiring all energy to come from storage during this time period. Therefore, the storage facility must be able to hold at least enough energy for the longest night of the year in order to provide base-load energy. I then multiplied the amount of storage required for this minimum amount by multiples of 0.5 from 1.0 to 12.5 for the analysis.

For each of these 24 storage capacity values I performed a midpoint search to identify the array size that gave  $CF = 0.907 \pm 0.001$ . The search began with an array area of  $1 \text{ km}^2$ , the lower bound array size, and  $900 \text{ km}^2$ , the upper bound array size. As most locations not in the poles only required an array size of less than  $20 \text{ km}^2$ , I performed an initial parameter sweep of 2, 5, and  $10 \text{ km}^2$ , replacing the upper and lower bounds on the array size as necessary. From this initial parameter sweep, I proceeded with the mid-point search to determine the capacity factor for an array sized according to the midpoint of the current upper and lower bound array sizes. I then replaced either the upper or lower bound based on the capacity factor of this analysis. The search stopped once the capacity factor was within the acceptable range of  $0.907 \pm 0.001$ .

While I have assumed base-load generation only from these facilities in the

current analysis, CAES facilities may actually be able to provide a higher revenue stream for themselves by providing ancillary services in addition to direct energy provision. Due to the decoupling of the compressor and turbine, both of these systems can provide ancillary services. Provision of non-spinning reserves has been determined to potentially increase the over 30%, and provision of non-spinning, spinning, and regulation up and down reserves can potentially increase profits 40-60% [122]. A direct analysis of providing ancillary services with these facilities was not performed in this dissertation, however should be noted as a potential additional revenue stream for the coupled facilities. Use of CAES facilities to provide ancillary services has been discussed in more detail for the Electric Reliability Council of Texas [122] and for use in high wind penetrations specifically [123].

While CAES is the preferred storage medium, in many locations the geology is either not suitable for CAES, or would be too expensive [105]. Figure 3.2 shows a general map of rock types throughout the globe. Salt domes are preferable for CAES facilities, but aquifers, sedimentary basins and hard rock can all be used [49]. While geology feasible for CAES exists in 68.5% of all land not including Antarctica, locations labeled as “Folded or Fractured” rock in Figure 3.2, would be unsuitable for this technology. As such, I also examined the use of above-ground CAES and batteries in the energy flow model.

Above-ground CAES utilizes the same technology as below-ground CAES, however the compressed air is stored in tanks as opposed to underground caverns. Because of this, above-ground CAES is typically envisioned to have a capacity no larger than 10 MW. However, for this analysis I assumed that multiple above-ground units would be installed to provide the required storage. The energy ratio for above-ground CAES was assumed to be 1 [107].

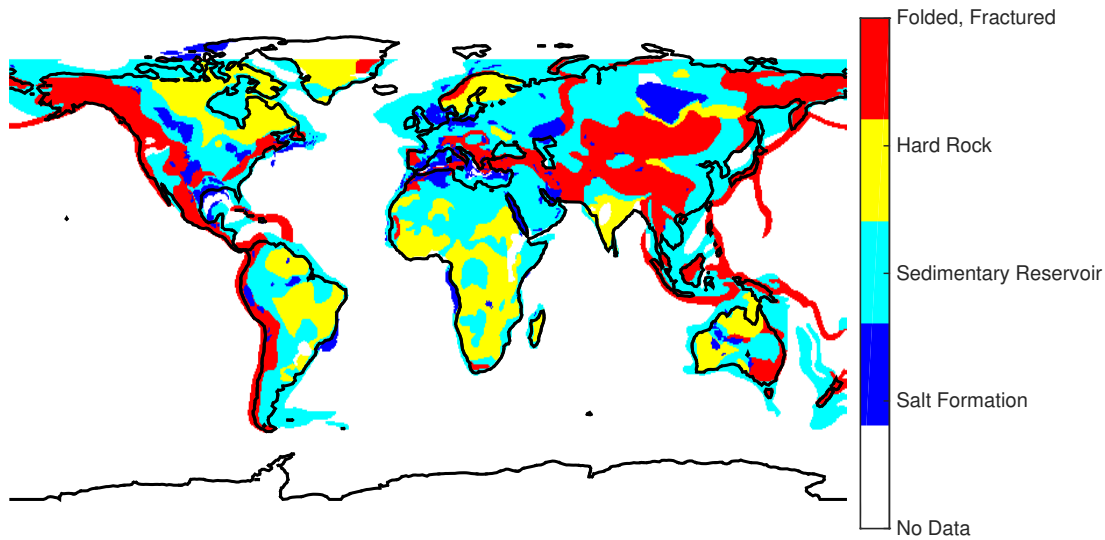


Figure 3.2: Compressed Air Energy Storage (CAES) can likely be sited in many rock types and geological structures, including salt domes, sedimentary basins, and hard rock. This figure shows globally where these formations exist and as such might be able to site a CAES facility. This map was prepared by Ian Duncan and Cari Breton at the University of Texas at Austin Jackson School of Geology, using the Geologic Province Map from US Geological Survey and [124].

Batteries are very easy to site, and so remove the locational limitations of below-ground CAES. They also do not utilize natural gas in their operation. However, because natural gas is not used as an additional energy source, the total energy batteries are able to provide are lower than that of CAES. For this model I assumed a round-trip battery efficiency of 75% [109]. The energy flow model for batteries operates qualitatively similar to the energy flow model for CAES, however does not include injection of natural gas and so Eq. 3.5 is not utilized. In addition, the battery efficiency is used instead of the energy ratio when accounting for system losses and inefficiencies. For this analysis I have assumed the batteries would not degrade over their life cycles. Including this degradation would impact the ability to store energy in these facilities, however I assume this degradation would be minimal over the rated cycle life of the facility.

## 3.2 Levelized Cost of Electricity

An important question for solar powered systems is what the total cost will be. Until recently, solar photovoltaics were prohibitively expensive for large-scale development. However, with the recently dropping costs of PV panels, such systems are becoming increasingly cost competitive. In order to quantify where such systems would be feasible, I computed the levelized cost of electricity for a coupled photovoltaic and grid-scale energy storage facility operating as described in Section 3.1.

### 3.2.1 Cost Model

I computed the total levelized system cost as the sum of the individual component costs:

$$C_{total} = C_{Array} + C_{Storage} + C_{Fuel} + C_{Replacement} + C_{O\&M} \quad (3.7)$$

Here  $C_{Array}$  is the cost of the module and balance of system components for the array, including inverters, mounting, wiring and other components [\$],  $C_{Storage}$  is the cost of the compressed air energy storage system (CAES) [\$],  $C_{Fuel}$  is the cost of fuel [\$],  $C_{O\&M}$  is the cost the operations and maintenance costs [\$], and  $C_{Replacement}$  is the total cost of replacing the photovoltaic modules and inverter [\$]. All of the component costs are levelized over the lifetime of the coupled system using continuous discounting.

Figure 3.3 shows the timing of the cash flows that go into the respective costs. The capital costs of the storage facility are assumed to be a single up-front cost. The array capital costs are assumed to be distributed throughout the construction period, due to the modular nature of photovoltaic array construction. Balance of system components are replaced twice during the system lifetime, these costs largely consist of replacing the inverter for the array. In order to compensate for degradation of the photovoltaic array I assume that solar panels are added each year in an amount equal

to the degradation as a continuous replacement cost. Other continuous costs include operations and maintenance costs and fuel costs. All point costs are discounted as single costs and all distributed costs are discounted using continuous discounting. The discount rate used was 7%.

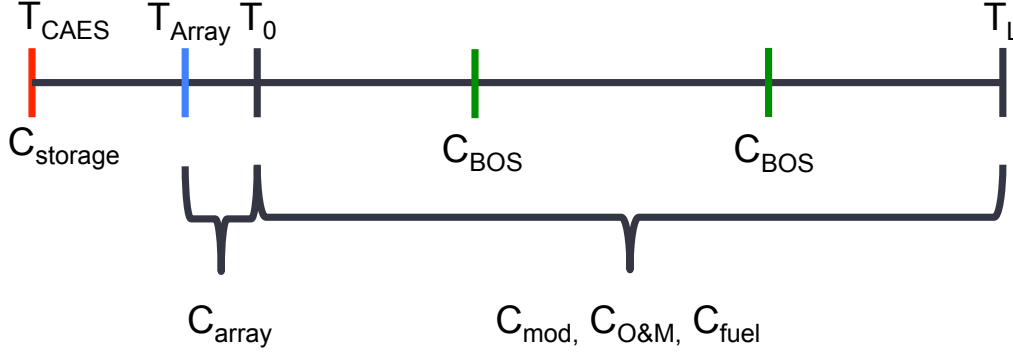


Figure 3.3:  $C_{storage}$ ,  $C_{BOS}$  are paid as lump sums while  $C_{Array}$ ,  $C_{mod}$ ,  $C_{O\&M}$ , and  $C_{fuel}$  are distributed costs. Depending on the array size,  $T_{array}$  may begin before  $T_{CAES}$ .

The levelized component costs are determined by Equations (3.8) - (3.12).

$$C_{array} = W_A * (C_{mod} + C_{BOS}) \frac{e^{-\rho T_{Array}} - e^{-\rho T_0}}{-\rho T_{Array}} \quad (3.8)$$

$$C_{Storage} = (S * C_{res} + C * C_{BOP}) e^{-\rho T_{CAES}} \quad (3.9)$$

$$C_{O\&M} = [C_{AO\&M} * W_A + C_{VO\&M} \frac{E_{Storage}}{T_L} + C_{FO\&M} * C] \frac{e^{-\rho T_0} - e^{-\rho T_L}}{\rho} \quad (3.10)$$

$$C_{fuel} = (C_{fuelPrice} * HR_{CAES} \frac{E_{Storage}}{T_L}) (e^{-\rho T_0} - e^{-\rho T_L}) / \rho \quad (3.11)$$

$$C_{replacement} = W_A * C_{mod} * \delta * \frac{e^{-\rho T_0} - e^{-\rho T_L}}{\rho} + W_A * C_{BOS} * f_{BOS} (e^{-\rho T_{BOS}} + e^{-2\rho T_{BOS}}) \quad (3.12)$$

Here  $W_A$  is the array size [ $MW_e$ ],  $E_{Storage}$  is the total energy placed in storage over the lifetime of the facility [ $MWh_e$ ],  $S$  is the storage capacity [ $MWh_e$ ], and  $C$  is the desired output of the combined system, 100  $MW_e$ .

When battery storage is used instead of compressed air energy storage, Eqs. (3.9)-(3.10) become

$$C_{Storage} = (S * C_B)e^{-\rho T_B} \quad (3.13)$$

$$C_{O\&M} = [C_{AO\&M} * W_A + C_{BO\&M} * C](e^{-\rho T_0} - e^{-\rho T_L})/\rho \quad (3.14)$$

and Eq. (3.11) no longer applies. The discount equations need to reflect that battery systems must be replaced after 15 years, Fig. 3.4, and that there is no use of natural gas.

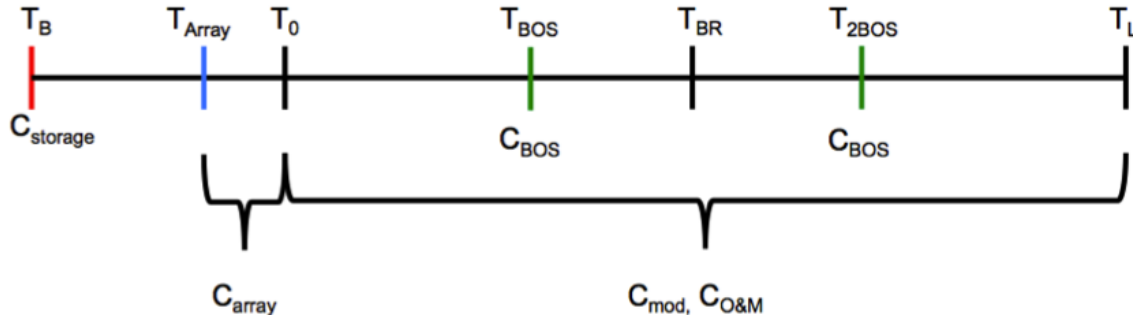


Figure 3.4:  $C_{storage}$ ,  $C_{BOS}$  are paid as lump sums while  $C_{Array}$ ,  $C_{mod}$ , and  $C_{O\&M}$  are distributed costs. Depending on the array size,  $T_{array}$  may begin before  $T_B$ .

The unit costs for components, the operations and maintenance costs, and the lead/lag times are drawn from the literature and summarized in Tables 3.1-3.3. All other terms in Equations (3.8) - (3.12) are also defined in Tables 3.1-3.3.

Above-ground CAES facility use the same equations as below-ground CAES. It should be noted that above-ground compressed air energy storage typically has capacities on the order of 10s  $MW_e$  rather than 100s of  $MW_e$ . However, I assume that above ground compressed air system would be scalable, or would be used in a distributed manner throughout the  $0.5^\circ \times 0.5^\circ$  area with a total capacity of 100  $MW_e$ .

The following sub-sections provide further detail on the costs and other variables utilized in the cost model.



Quantity	Variable	Cost	Cost Range	Reference
Module	$C_{module}$	$0.79 \times 10^6$ \$/MW <sub>p</sub>	$0.72-0.85 \times 10^6$ \$/MW <sub>p</sub>	[30, 88, 125]
BOS Costs	$C_{BOS}$	$1.13 \times 10^6$ \$/MW <sub>p</sub>	$0.83-1.43 \times 10^6$ \$/MW <sub>p</sub>	[30, 88, 125]
Array O&M	$C_{AO\&M}$	$21.3 \times 10^6$ \$/MW <sub>p</sub> -yr	$8-40 \times 10^6$ \$/MW <sub>p</sub> -yr	[88, 91, 126, 127]
Efficiency, Array	$\eta$	14 %		[13, 128]
Degradation, Array	$\delta$	0.513 %/yr	0.2 – 1 %/yr	[93, 129]
BOS Replacement, Array	$f_{BOS}$	27.8%	13.3% – 70%	[30, 93, 125]
BOS Replacement interval	$T_{BOS}$	10.4 years	7 – 15 yrs	[128, 129]
Array Construction	$T_{Array}$	variable		Table 3.15
System Lifetime	$T_L$	30 years	25 - 40 yrs	[88, 129]
Discount Rate	$\rho$	7 %/yr	5 – 10 % /yr	[129, 130]

Table 3.1: Discount model input parameters for photovoltaic array.

Quantity	Variable	Value	Value Range	Reference
Reservoir Cost	$C_{res}$	2,000 \$/MWh <sub>e</sub>		[47–49]
Salt Dome		30,000 \$/MWh <sub>e</sub>		[48, 49]
Other formations		193,271 \$/MWh <sub>e</sub>		[48, 107, 131]
Above ground			173,271 – 203,471 \$/MWh <sub>e</sub>	
Turbine/Compressor (below ground)	$C_{BOP}$	635,750 \$/MW <sub>e</sub>	440,000–989,000 \$/MW <sub>e</sub>	[47–49]
Turbine/Compressor (above ground)	$C_{BOP}$	1,179,600 \$/MW <sub>e</sub>	430,000–2,000,000 \$/MW <sub>e</sub>	[48, 107, 131, 132]
O&M, below ground				
variable	$C_{VO\&M}$	6.65 \$/MWh <sub>e</sub>	3–10.3 \$/MWh <sub>e</sub>	[47–49, 133]
fixed	$C_{FO\&M}$	$6.86 \times 10^3$ \$/MW <sub>p</sub> -yr	$2.5-14.07 \times 10^3$ \$/MW <sub>p</sub> -yr	
O&M, above ground				
variable	$C_{VO\&M}$	$4 \times 10^3$ \$/MW <sub>p</sub> -yr	3–5 \$/MWh <sub>e</sub>	[107]
fixed	$C_{FO\&M}$	$11.9 \times 10^3$ \$/MW <sub>p</sub> -yr	8–15.86 \$/MWh <sub>e</sub>	[48, 107]
Fuel Cost	$C_{fuelPrice}$	By country	<1 – $30.1 \times 10^{-3}$ \$/MJ	[134–136]
Energy Ratio	ER	0.73	0.56 – 0.84	[47–49]
		MWh <sub>e,in</sub> /MWh <sub>e,out</sub>	MWh <sub>e,in</sub> /MWh <sub>e,out</sub>	
Heat Rate, below ground	$HR_{CAES}$	$4.462 \times 10^3$ MJ/MWh <sub>e</sub>	4.2 – $4.819 \times 10^3$ MJ/MWh <sub>e</sub>	[47–49]
Heat Rate, above ground	$HR_{CAES}$	$4.51 \times 10^3$ MJ/MWh <sub>e</sub>	3.9 – $6.2 \times 10^3$ MJ/MWh <sub>e</sub>	[107, 132]
CAES Construction	$T_{CAES}$	-3 years	-2.5 – -4 yrs	[47–49]

Table 3.2: Unit costs for compressed air energy storage. Data on unit costs for both above ground and below ground systems are shown. Here CAES stands for ‘compressed air energy storage’. It is assumed that the CAES construction time is the same for both above and below ground systems.

Quantity	Variable	Value	Value Range	Reference
Battery Capital Costs (NaS)	$C_B$	342,000 \$/MWh <sub>e</sub>	238,000-535,000 \$/MWh <sub>e</sub>	[107, 109]
Battery Capital Costs (DOE Goal)	$C_B$	150,000 \$/MWh <sub>e</sub>		[107] [137]
Battery O&M fixed	$C_{BFO\&M}$	4,300 \$/MW <sub>e</sub> -yr	4,300-4,500 \$/MW <sub>e</sub> -yr	[107]
variable	$C_{BVO\&M}$	0.5 \$/MWh <sub>e</sub>	0.4 – 0.5 \$/MW <sub>e</sub> -yr	[107]
Battery efficiency	$\eta$	75%	71-90%	[107, 109]
Battery lifetime	$T_{BR}$	15 years		[45, 107]
Battery Construction	$T_B$	-1 year		[107]

Table 3.3: Battery unit costs, lead lag times, and efficiencies.

### 3.2.1.1 Battery Costs

The battery costs were determined for two different technologies, sodium sulfur and DOE’s goal for batteries by 2050. Sodium sulfur batteries are currently commercially available and have been installed in several locations, including Japan and Texas [45, 50]. The costs for these batteries vary widely, so for my cost estimate I utilized the mode values presented in a review article [109], which accounted for differences in efficiency, assumed lifetime, and use profiles. These costs were given in 2011 EUR, so the costs were converted to USD using the IRS yearly average conversion rate value of 0.748 EUR/USD for 2011 [138]. The costs for the DOE’s goal technology were taken from [137], indicating the technology costs deemed feasible by the DOE by the year 2050.

I assumed both technologies had a lifetime of 15 years, and an efficiency of 75% as a low-end estimate [109]. Operation and maintenance costs were accounted for and were taken from the DOE/EPRI 2013 Electricity Storage Handbook [107]. These values were held constant for both battery technologies.

I accounted for replacement costs by assuming a 15-year lifetime for the batteries, and that they would be completely replaced at this time, leading to one replacement

during the system lifetime. This was discounted according to the replacement time of the battery system. All variables specifically associated with battery storage are given in Table 3.3.

### 3.2.1.2 CAES Geology

Salt domes are ideal for below-ground CAES, and Fig. 3.5 shows their geographical distribution [124]. For all other locations I assume the storage cavern would be built into rock formations, which is significantly more expensive, Table 3.2. While some locations would be able to build storage caverns at a cost between these extremes, I assumed the upper bound on storage costs as a conservative estimate.

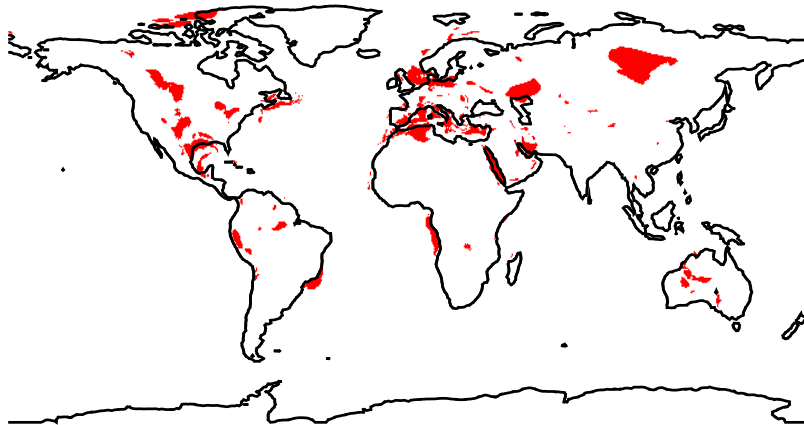


Figure 3.5: The geographical distribution of salt deposits is shown [124]. These locations are particularly good for compressed air energy storage and are the cheapest locations for building reservoirs.

### 3.2.1.3 Array Construction Time

The time to built an array,  $T_{Array}$ , was computed using data from utility scale photovoltaic installations, Table 3.4. I assumed a linear relationship between array

size and construction time, and computed a linear least squares curve fit with the data from 11 operational or partially operational utility-scale photovoltaic arrays. From this data, I determined a curve fit for the construction time for an array based on its size as:

$$T_{Array} = 0.0054W_A + 0.59 \quad (3.15)$$

which has an  $R^2$  value of 0.97, Fig. 3.6. I used Eq. (3.15) to determine the approximate construction time of each array determined in the energy flow model. In practice, I multiply  $T_{Array}$  by -1 before substituting it in Eq. (3.8) as it represents a lead time.

<b>Photovoltaic Array</b>	<b>Capacity [MW]</b>	<b>Construction Time [years]</b>	<b>Notes</b>	<b>Reference</b>
Mohammed bin Rashid Al Maktoum Solar Park	13	0.58	Operational Oct. 2013	[139]
Blythe, CA	21	0.33	Operational Dec. 2009	[140]
Cimarron, NM	30	0.67	Operational Dec. 2010	[141]
Copper Mountain Solar 1	48	1	Operational Dec. 2010	[142]
Copper Mountain Solar 2	92	1	Operational Dec. 2012	[143]
Antelope Valley Solar Ranch 1	100	1.5	Partial Deployment	[144]
Mesquite Solar 1	150	1.5	Operational Dec. 2012	[145]
California Valley Solar Ranch	250	2	Operational Oct. 2013	[146]
Agua Caliente	250	2	Partial Deployment	[147]
Topaz Solar Farm	550	3.5	Expected Completion 2015	[148]
Desert Sunlight Solar Farm	550	3.5	Expected Completion 2015	[149]

Table 3.4: Construction times for currently operational utility scale solar power facilities. Used to calculate an approximate linear relationship between array capacity and construction time for use in the cost model given above.

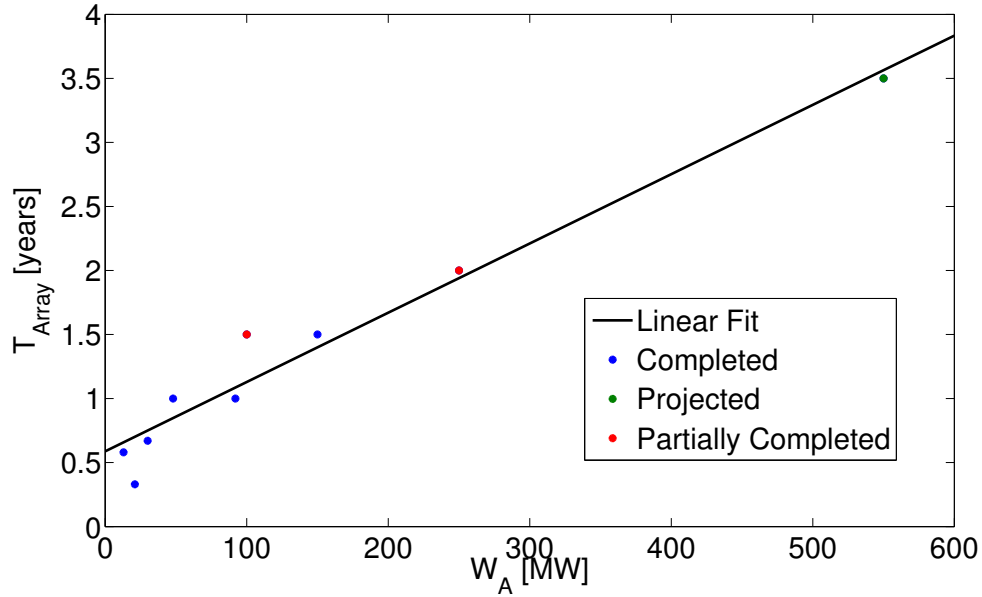


Figure 3.6: Data are from the construction times for grid scale facilities built, Table 3.15. Two 550  $MW_e$  facilities are currently under construction, however are on schedule for their projected 2015 completion, so were included as representative of large scale arrays. I used a linear least squares curve fit to approximate these times to a linear function and used this to estimate the array construction times in the model.

### 3.2.1.4 Natural Gas Prices

Natural gas prices can vary considerably from year to year, and also by region, from a 2013 low of  $< \$1 \times 10^{-3}/\text{MJ}$  in Turkmenistan to over  $\$30 \times 10^{-3}/\text{MJ}$  in Denmark [135, 136]. In particular, the retail price of industrial natural gas in Japan, South Korea, and Brazil is  $\$16 \times 10^{-3}/\text{MJ}$ , and it has recently jumped to  $\$8 \times 10^{-3}/\text{MJ}$  in India [48, 107]. At  $\$16 \times 10^{-3}/\text{MJ}$ , the land fraction that can produce baseload electricity  $\leq \$0.08/kWh_e$  falls to 15%, assuming all other costs as in Tables 3.1-3.3. At  $\$8 \times 10^{-3}/\text{MJ}$  it is 31%. The dependence on natural gas price is shown in Fig. 3.7. Natural gas markets are in a period of considerable change, and the country specific data used in this study are very likely to evolve.

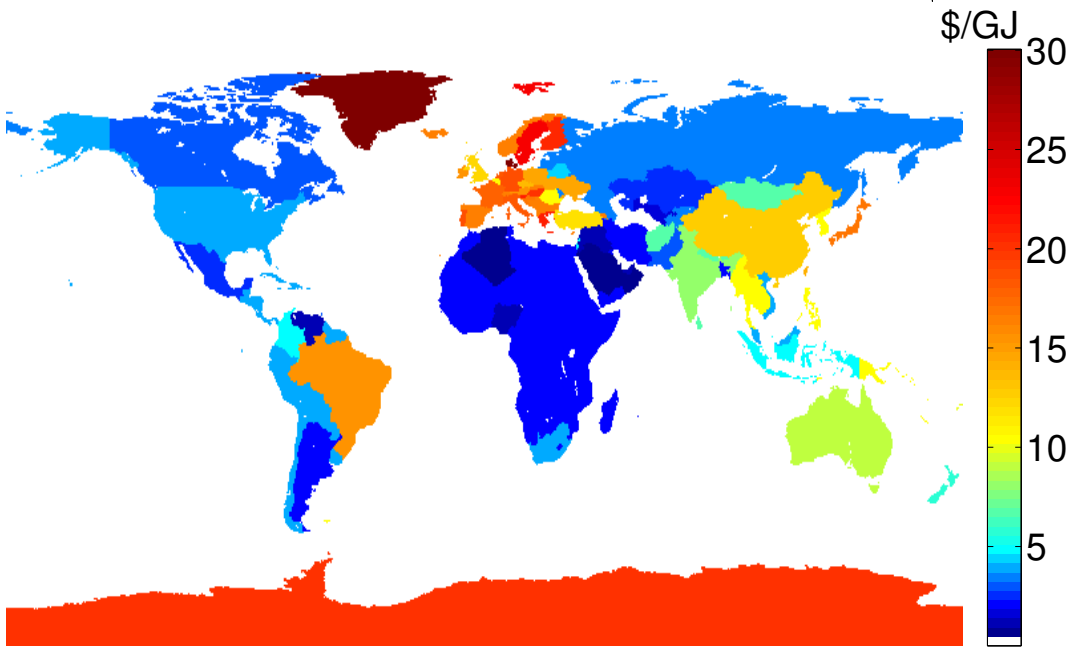


Figure 3.7: The retail price of natural gas around the world, as described in Table 3.2.

### 3.2.2 Life-cycle Electricity Cost

The model described in Section 3.2 can be used to determine the total system cost for any particularly sized array and storage facility. This can be used in conjunction with the energy flow model from Section 3.1 to identify the life-cycle cost of energy from a particular system. This energy cost is computed as the total levelized cost divided by the energy provided by the system over its lifetime:

$$C_{energy} = \frac{C_{total}}{\sum_{lifetime}(E_g + E_{fs})} \quad (3.16)$$

where  $C_{energy}$  is the life-cycle cost of energy in  $\$/kWh_e$ .

I was most interested in determining the system which would provide the lowest levelized electricity cost at each location. To do this, I optimized the array size and storage capacity for the minimum cost configuration based on the 24 system sizes determined by in the energy flow model. For each of 24 separate storage sizes

the array size,  $W_A$ , which provided a capacity factor greater than or equal to 0.907 was determined. Storage facilities as large 13500  $MWh_e$  have been proposed and studied [106], so this was used as an upper bound and capped the total storage size at this amount. Many polar regions were unable to provide 100 MW of energy with a 90.7% capacity factor and 13500  $MWh_e$  storage due to long lasting polar nights.

For each combination of storage and array size, the life-cycle cost was determined using Equations (3.7)-(3.12) and (3.16). The costs of these 24 configurations were compared and the minimum cost solution was then identified at each location. The array size and storage capacity of this minimum cost solution were then utilized to determine the overall costs of the coupled facility.

Figures 3.8 - 3.9 show the array size and storage capacity respectively for the minimum cost configurations out of the 24 systems analyzed, specifically for

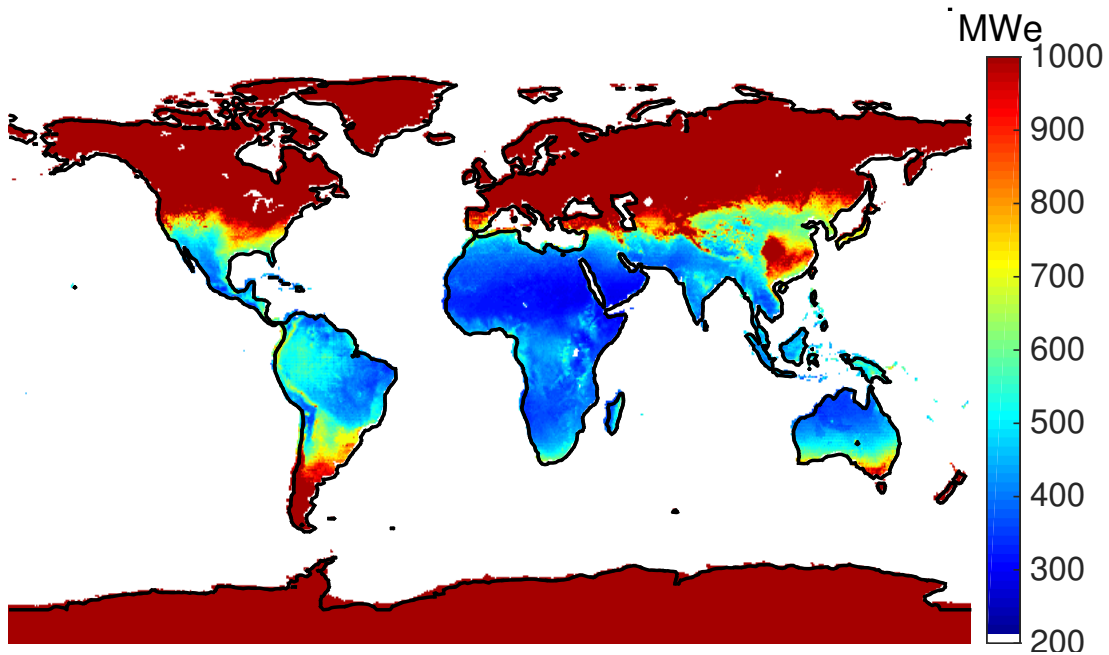


Figure 3.8: Array rated capacity in  $MW_e$  for the minimum cost configuration of the system. The minimum cost was determined by comparing 24 configurations of array and storage capacities.

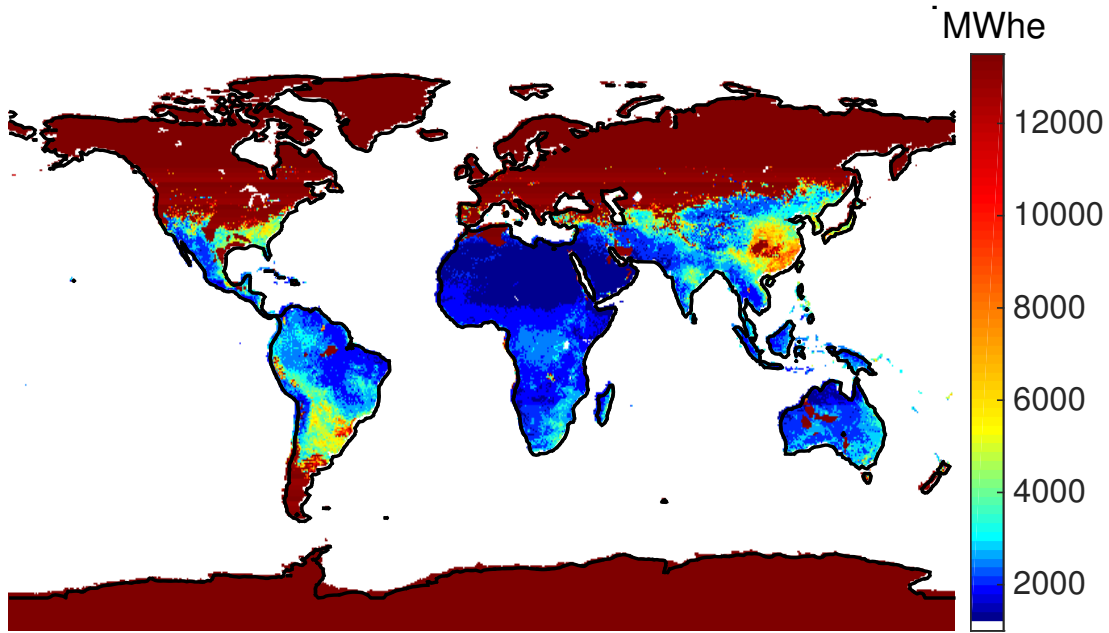


Figure 3.9: Total storage capacity in  $MWh_e$  for the minimum cost configuration of the system. The minimum cost was determined by comparing 24 configurations of array and storage capacities. The cost-optimized storage configuration was influenced by the location of salt domes, which are much cheaper for building CAES plants than other geologies.

below-ground CAES. Many of the non-polar locations with high storage capacities are locations with salt domes. Given the low cost to build below-ground CAES facilities here, the cost-optimized configurations include higher storage capacity than locations at similar latitudes without salt domes.

I performed the above cost analysis assuming the storage capacity was below-ground CAES, above-ground CAES, or battery storage independently. Figures 3.10 - 3.12 show the life-cycle energy costs for each of these technologies, as computed using Equations 3.7 - 3.16 and the costs provided in Tables 3.1-3.3. However, when using battery storage facilities, array costs of  $\$0.43/W_p$  for the module and  $\$0.57/W_p$  for the balance of system components were used to simulate  $\$1/W_p$  projected array costs. Battery storage facilities were not cost competitive with current average prices as presented in Table 3.1.



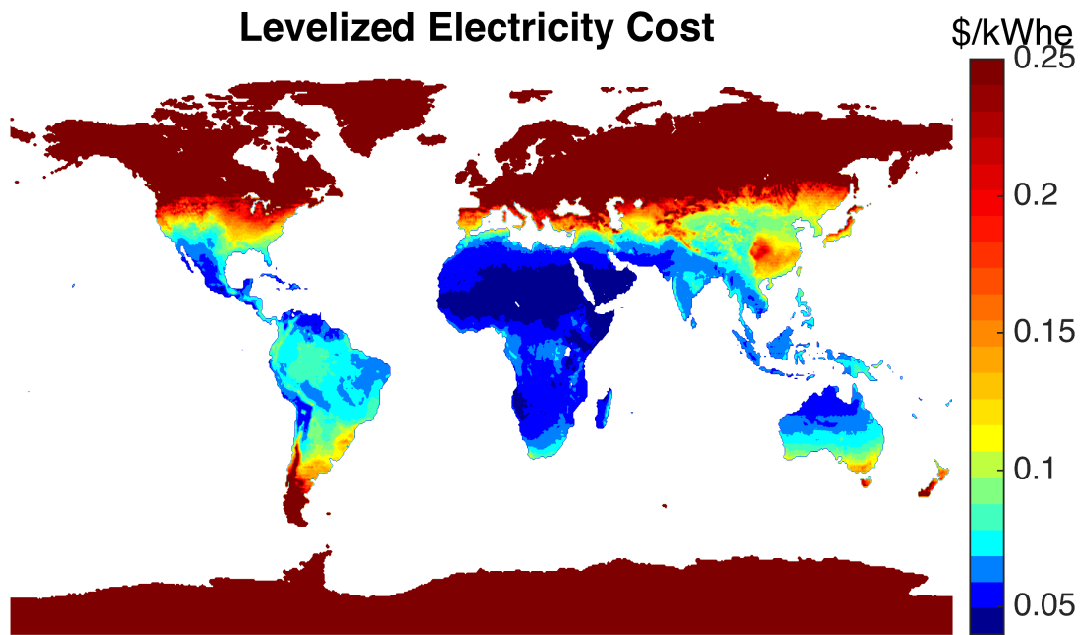


Figure 3.10: The life-cycle electricity cost for a coupled photovoltaic array and below-ground compressed air energy storage facility. The array and storage capacity were sized to provide the least-cost energy.

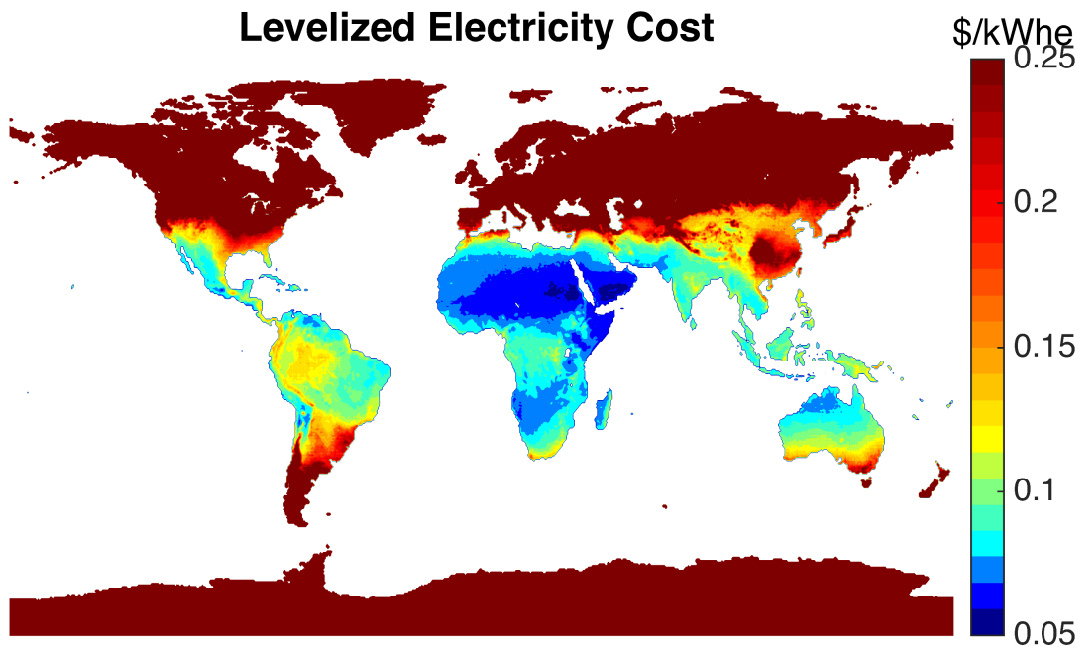


Figure 3.11: The life-cycle electricity cost for a coupled photovoltaic array and above-ground compressed air energy storage facility. The array and storage capacity were sized to provide the least-cost energy.

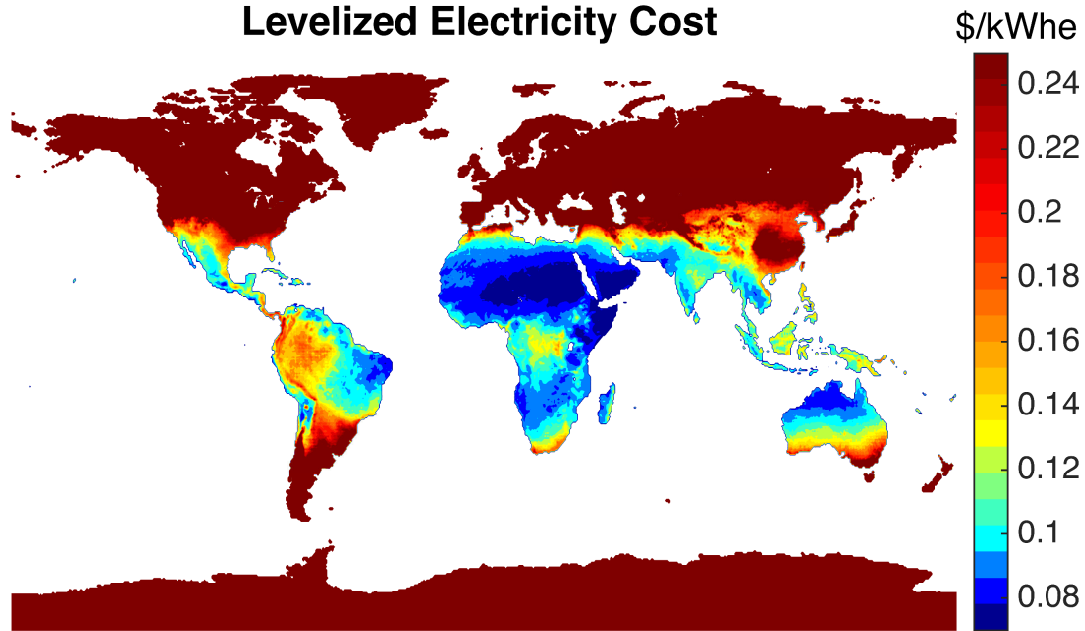


Figure 3.12: The life-cycle electricity cost for a coupled photovoltaic array and battery storage. The array and storage capacity were sized to provide the least-cost energy.

### 3.2.2.1 Cost Comparison

Extensive studies for the cost of building new nuclear capacity were done in 2003 and 2009. The estimates took into consideration recent experience in Japan and Korea as well as projections for the cost of new capacity in the US [10, 150]. The 2003 study put the levelized cost of electricity at  $\$0.067/kWh_e$  in 2002 US dollars, and the 2009 study put it at  $\$0.084/kWh_e$  in 2007 dollars. The biggest contributor to the difference was the cost of capacity, which was  $\$2000/kW_e$  and  $\$4000/kW_e$  respectively. When adjusted to 2010 US dollars the levelized cost estimates for the 2003 and 2009 studies are  $\$0.08/kWh_e$  and  $\$0.09/kWh_e$ , respectively. The low end of estimates for the cost of nuclear capacity in developing countries is consistent with the value assumed in the 2003 study. In order to be consistent with these estimates for nuclear power, I utilize  $\$0.08/kWh_e$  as a benchmark for low-cost energy from a base-load system.

The Fifth Assessment by the International Panel on Climate Change analyzed levelized cost of electricity from three different forms of coal fired power with carbon capture and storage as well as a combined cycle natural gas option. The later was estimated to be the least expensive, with a mean cost of  $\$0.086/kWh_e$  in 2010 US dollars [5], which is higher than the estimate of nuclear energy. To be conservative, I utilized the lowest cost estimate of these two estimates for low-carbon technologies when analyzing the potential feasibility of a coupled photovoltaic and energy storage system.

### 3.2.3 Variance in the levelized cost of electricity.

For each variable in the cost calculation, I computed the cost distribution and found a standard deviation. I assumed triangular distributions for the cost components with end points at the low and high values given in the literature and the peak at either the mean value, or the mode if there was a commonly cited value. Triangular distributions were used because typically only 2-4 data points were available for each variable. The peak value used in the cost analysis along with the range of cost values is given in Tables 3.1-3.3.

Mean values were assumed for the peak of the triangular distribution for the variables  $C_{mod}$ ,  $C_{BOS}$ ,  $C_{CAES}$ ,  $C_{AO\&M}$ ,  $C_{VO\&M}$ ,  $C_{FO\&M}$ ,  $C_{fuel}$ ,  $HR_{CAES}$ ,  $d$ ,  $f_{BOS}$ , and  $T_{BOP}$ . When ranges for a variable were given by a source, the min, mean, and max values of that range were used in computing the overall average value. This provided full representation of the data in each range given.

Mode values were used for the peak of the triangular distribution for the variables  $\rho$ ,  $T_{CAES}$ ,  $T_L$ , and  $T_{BOS}$ . Mode values were used for these variables because most or all sources listed a common value as either the only value, or gave a range of possible values but cited the most expected value as this common value. In this case

the full range of given values was used to compute the standard deviation, but this common value was used in computation of the cost itself.

The reservoir cost per  $MWh_e$  was assumed to be a constant for below-ground CAES, and based on the geology of each location. Only two CAES facilities have been constructed, and the range of costs is not well known. Sources typically give the same expected cost for cavern construction, Table 3.2. Because of this I assume  $C_{res}$  has no variance for below-ground CAES. Above-ground CAES reservoir costs did show a range in the literature, and so the variance of  $C_{res}$  for above-ground CAES was not assumed to be 0.

The variance of each variable, except for  $T_{Array}$ , was computed separately for each of the  $i$  unit costs:

$$\sigma_i = 1/18(a^2 + b^2 + c^2 - ab - ac - bc) \quad (3.17)$$

where  $a$  is the min value,  $b$  the peak, and  $c$  is the maximum value of the triangle. The exception to this was the array construction time,  $T_{Array}$ . For this variable, the variance was computed from the linear least squares fit of the data in Table 3.4.

Once the  $\sigma_i$  were computed for each variable, the standard deviation for the total cost was computed using the error propagation formula, and assuming that the unit costs were uncorrelated:

$$\sigma^2 = \sum_i \left( \sigma_i \frac{\delta C}{\delta x_i} \right)^2 \quad (3.18)$$

where  $x_i$  represents the unit costs. The standard deviation of the cost of electricity is shown in Figures 3.13 - 3.14.

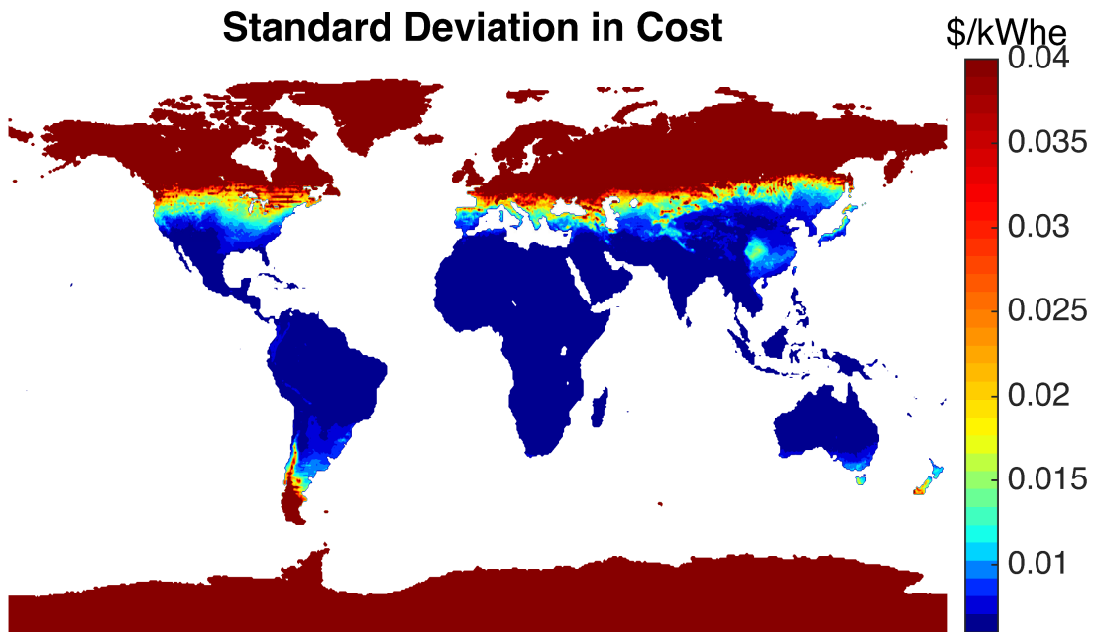


Figure 3.13: World map of standard deviation in electricity cost for the minimum cost system of coupled photovoltaic array and below-ground CAES.

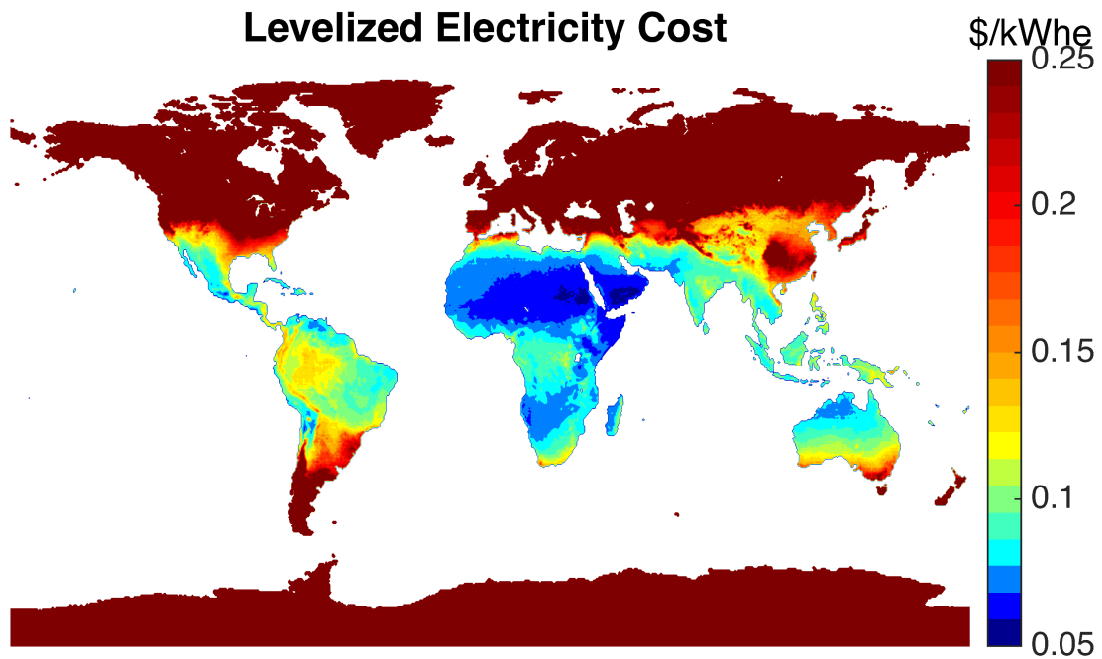


Figure 3.14: World map of standard deviation in electricity cost for the minimum cost system of coupled photovoltaic array and above-ground CAES.

### 3.2.4 Sensitivity Analysis

The sensitivity of the total cost to each of the variables used in the cost calculation can be seen in Fig. 3.15. The figures were generated by systematically varying a single variable while holding all other parameters in the cost model fixed. The variables were varied over the full ranges given in the literature for each value. In some cases these values were extended to show a wider range of potential values.

Two particular locations were used for this analysis, one with a low total system cost and one with a high total system cost. The size of the array and storage facility as well as the total energy provided from the system were used for each location. This was done in order to show any differences due to array size or storage capacity. The lower cost system had a  $2.1 \text{ km}^2$  array and  $2600 \text{ MWh}_e$  of storage. The higher cost system has an  $11.2 \text{ km}^2$  array and  $12700 \text{ MWh}_e$  of storage.

This analysis shows the effect that increases or decreases in particular variables will have on the cost, in particular which variables have the largest impact on cost and which variables do not influence cost to a high degree. I found that variations in the discount rate, as well as array and balance of system costs have the biggest effect on the levelized system, in large part due to the fact that these variables provide the largest fraction of the total cost. The construction time for the array is also important.

In addition, locations with high overall costs were more sensitive to changing module, balance of system and reservoir costs. These costs comprised a higher percentage of the total cost, so small changes in any of the variables led to a greater change in overall system costs. For the lower cost system, the fuel price had a much higher impact. With lower array and storage costs, fuel was a much more significant fraction of the system cost.

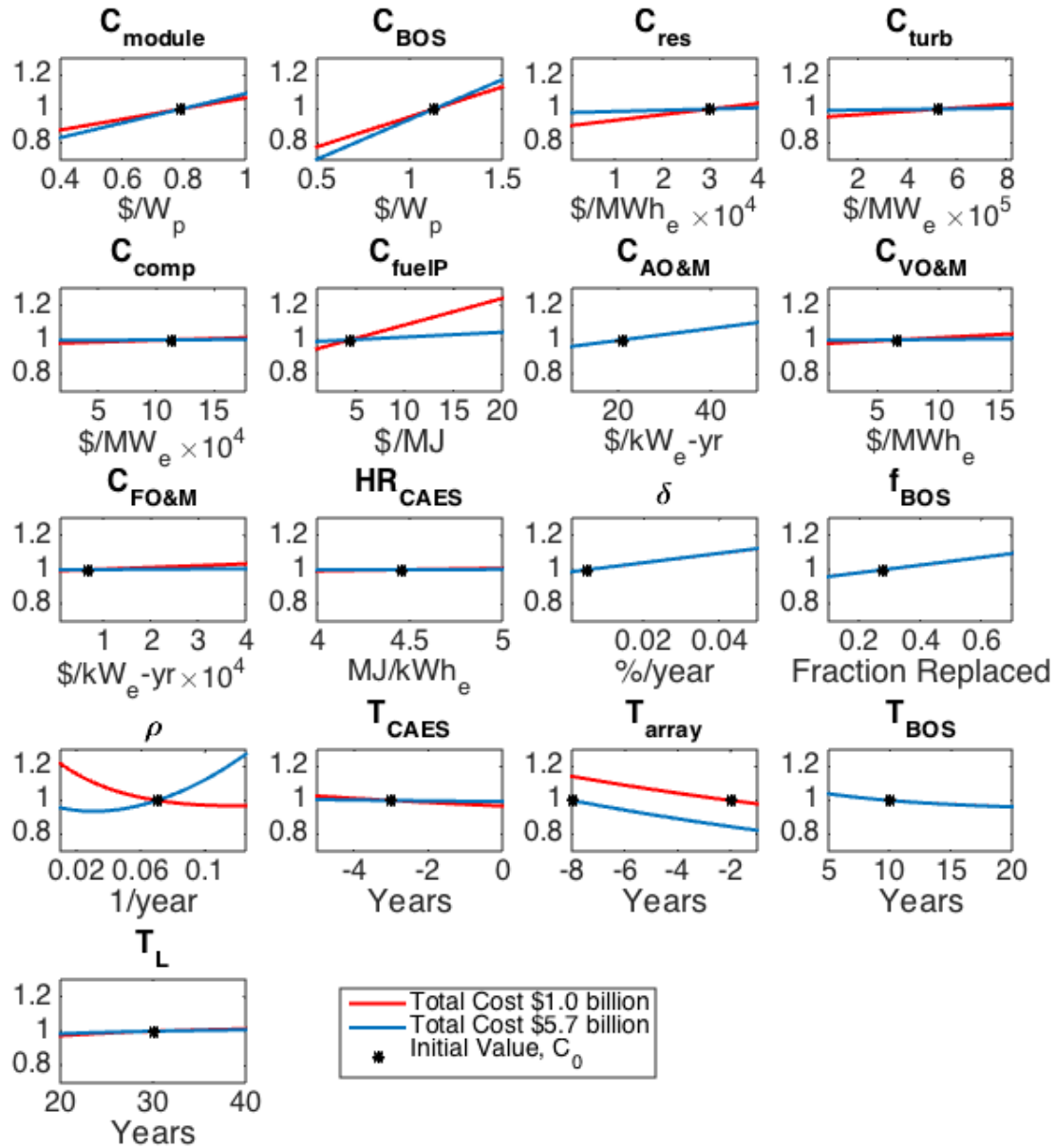


Figure 3.15: The sensitivity of the levelized system cost to changes in the unit costs. The costs were weighted according to the total system cost for two different locations, one with a lower total system cost and one with a higher one. The lower cost system had a  $2.1 \text{ km}^2$  array and  $2600 \text{ MWh}_e$  of storage. The higher cost system has an  $11.2 \text{ km}^2$  array and  $12700 \text{ MWh}_e$  of storage. Baseline unit costs and lad/lag times are from Tables 3.1-3.3. The initial cost and parameter value is shown with a dot in each figure.

### 3.3 Carbon intensity of the coupled system.

Lowering carbon emissions is a large draw for installing renewable energy systems. Solar power itself has very low life-cycle carbon emissions, the majority of which comes from manufacturing the photovoltaic panels. However, when coupled to CAES storage facilities, the use of natural gas contributes additional carbon emissions. Quantifying these emissions is important to determine the degree to which the coupled system could reduce carbon emissions compared to traditional generators such as coal or natural gas.

I calculated the emission rate for the combined system of photovoltaics and CAES using life-cycle emissions from the manufacturing, construction, and operation of the photovoltaic modules and the storage system. The emissions from the storage facility include construction of the facility,  $19.4 \times 10^6$  g CO<sub>2</sub>-eq/MWh capacity, the delivery systems for the natural gas, 11.1 g CO<sub>2</sub>-eq/MJ natural gas delivered, and the burning of natural gas, 50.3 g CO<sub>2</sub>-eq/MJ natural gas consumed [44]. The total green-house gas emissions were computed as the sum of these contributions:

$$GHG_{CAES} = S * \left( 19.4 \times 10^6 \frac{g - eqCO_2}{MWh_e} \right) + E_s * HR * \left( 1000 \frac{kWh_e}{MWh_e} \right) * \left( 61.4 \frac{g - eqCO_2}{MJ} \right) \quad (3.19)$$

where  $E_s HR_{CAES}$  (1000 kWh<sub>e</sub>/MWh<sub>e</sub>) is the total natural gas used in MJ. The largest contributor of emissions was the natural gas consumption.

I computed the emissions from the photovoltaic system using mean values presented by Hsu et al. (2012) [8], who calculated the emissions rate for a photovoltaic module assuming an efficiency of 14%, performance ratio of 0.8, average irradiance of 1700 kWh/m<sup>2</sup>/yr and a 30-year lifetime. I multiplied their result of 52 g-eq CO<sub>2</sub>/kWh<sub>e</sub> by their assumed efficiency, performance ratio (ratio of AC to DC electricity), average



irradiance and system lifetime to calculate the green-house gas emissions per  $m^2$  of array, which yielded  $2.97 \times 10^5$  g-eq  $CO_2/m^2$ . I then calculated the emissions from the photovoltaic system as:

$$GHG_{PV} = A * 2.97 * 10^5 \text{ g} - \text{eq}CO_2/m^2 \quad (3.20)$$

where  $A$  was the array size in  $m^2$  as calculated from the cost optimization and Eq. (3.2).

The emissions from the two systems were summed and then divided by the total energy provided by the PV-CAES system over its lifetime to calculate the emissions per unit of energy provided:

$$Emissions = \frac{GHG_{CAES} + GHG_{PV}}{\Sigma_{lifetime}(E_g + E_{fs}) * (1000 \frac{kWh_e}{MWh_e})} \quad (3.21)$$

Figure 3.16 shows the carbon intensity for the coupled system in the regions for which the cost of baseload electricity was found to be  $\leq \$0.08/kWh_e$ .

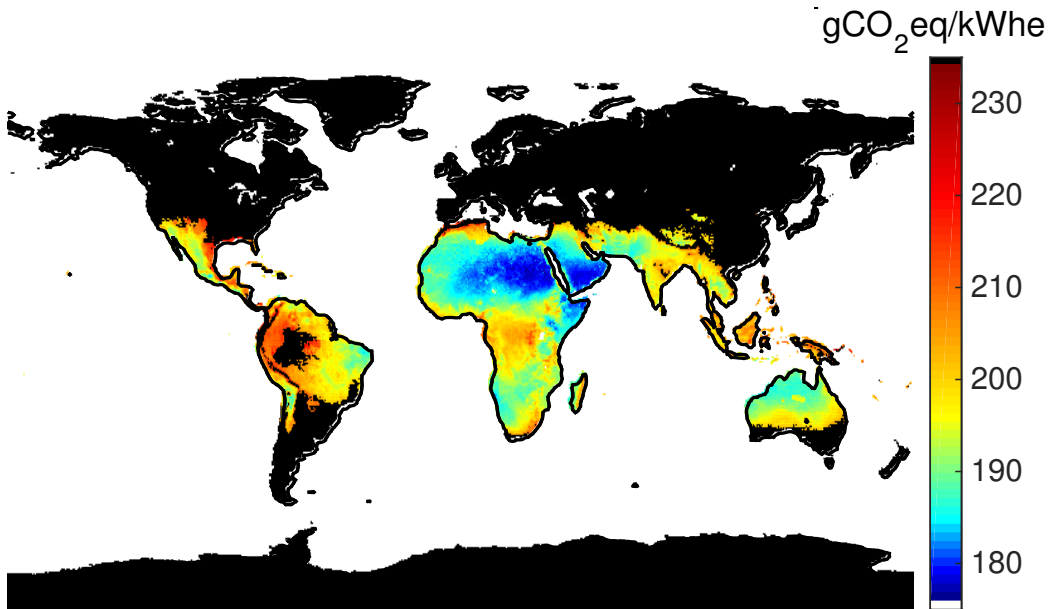


Figure 3.16: Green-house gas emissions of coupled PV-CAES system, colored for all locations with a leveled cost of  $\leq 0.08$   $\$/kWh_e$ .

## 3.4 Global Analysis

As described in sub-section 3.2.2.1, the cost of energy from a nuclear power facility is projected to be  $\$0.08/kWh_e$  [10], and estimates of electricity costs for carbon capture systems are expected to be higher [5]. I use this as a reference cost below which the coupled photovoltaic-CAES facility would be cost competitive as a low-carbon base-load energy source. Of particular importance are locations globally for which such a low-cost system could be sited.

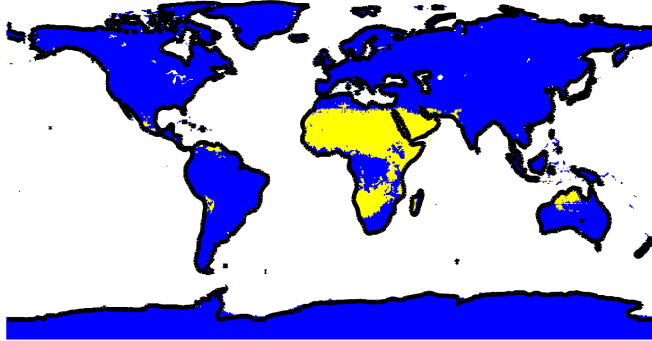
### 3.4.1 Feasible land fraction

The global land area for which the system described in Section 3.1 and 3.2 is capable of providing low-cost base-load energy has dropped dramatically given falling solar prices. Figure 3.17 shows the global land area for which the energy cost of a coupled PV-CAES facility is less than  $\$0.08/kWh_e$  for several different PV module and balance of system costs. All other costs are held fixed.

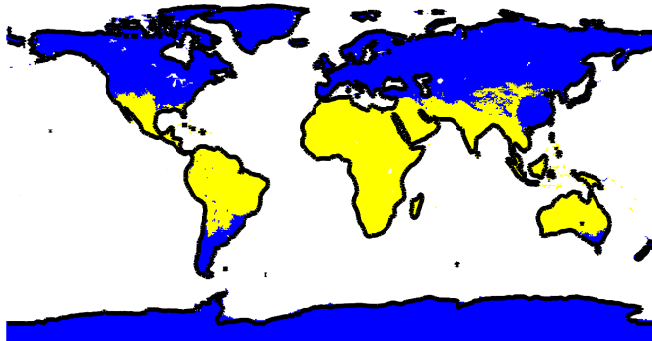
The costs of photovoltaic modules and balance of system components dropped significantly since 2010, from  $1.85 \$/W_p$  for modules and  $1.39 \$/W_p$  for balance of system components to  $0.72 \$/W_p$  for modules and  $0.83 \$/W_p$  for balance of system components in 2013 [30]. Costs are expected to continue dropping to a combined  $\$1/W_p$  for both module and balance of system components within a decade [92,93]. For  $\$1/W_p$  combined costs, I assumed costs of  $\$0.43/W_p$  for the module and  $\$0.57/W_p$  for the balance of system components.

Above-ground CAES is a more expensive alternative to traditional CAES, and as such has an energy cost of less than  $\$0.08/kWh_e$  for a much smaller fraction of the earth's surface. However, if PV costs drop below  $\$1/W_p$  it becomes a much more cost effective option.

### 2010 Array Cost



### 2013 Array Cost



### \$1/Wp Array Cost

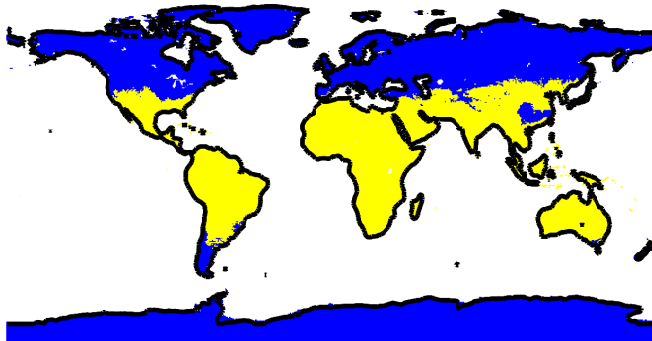


Figure 3.17: Fraction of global land for which the life-cycle electricity cost is less than  $\$0.08/kWh_e$ . The dropping costs of photovoltaic modules has greatly improved the ability of photovoltaic systems to provide low cost power globally

Batteries are the most costly storage option I investigated. They are not currently cost effective with today’s photovoltaic and storage costs. However, assuming that the cost of photovoltaics will drop to  $\$1/W_p$  within the next 10-15 years, this could be an option for large-scale storage coupled to solar power facilities. Additionally, the U.S. Department of Energy has set a goal for battery prices to drop to  $\$150/kWh_e$ . Such a cost reduction would also improve the economic feasibility of a coupled PV-battery base-load system.

Figure 3.18 shows for a coupled PV-battery system the percentage of global land with a life-cycle energy cost less than or equal to a particular value. This is shown for both current technologies, assumed to be sodium-sulfur (NaS) batteries, and for the Department of Energy goal battery. While there is only a small land area with an energy cost less than  $\$0.08/kWh_e$ , a coupled PV-battery facility would be more cost-competitive in locations with high costs of electricity.

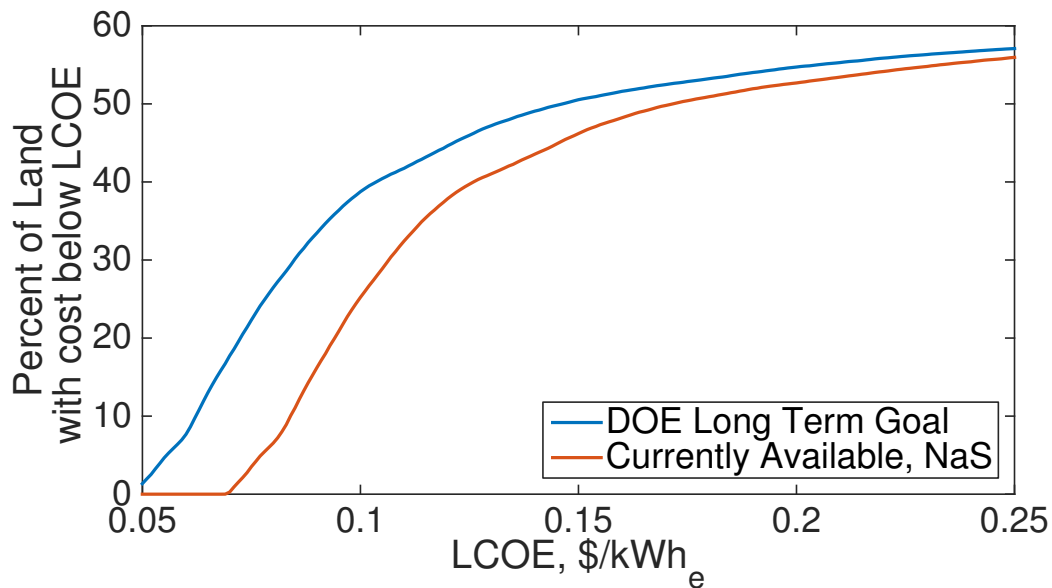


Figure 3.18: The percentage of land area with less than a particular energy cost is shown for two battery systems, currently available sodium-sulfur batteries and the Department of Energy (DOE) goal for battery costs.

The percent of land with energy cost less than  $\$0.08/kWh_e$  for each of the three storage technologies are shown in Table 3.5. The percentages are shown for both the average array costs from Table 3.1 used in this analysis and for  $\$1/W_p$  array costs.

<b>Land Percentage with cost &lt; <math>\\$0.08/kWh_e</math></b>		
Storage Technology	Array Cost	
	Average	$\$1/W_p$
Below-Ground CAES	43.1%	56.1%
Above-Ground CAES	17.5%	43.0%
NaS Battery	0 %	6.5%
DOE Goal Battery	3.1 %	26.5%

Table 3.5: The percentage of land area across the globe for which the life-cycle cost of energy is less than  $\$0.08/kWh_e$ , for each of the potentially storage technologies investigated. Both types of batteries are shown. The percentages are shown for both the average array cost assumed in this analysis as well as if the array cost were to drop to  $\$1/W_p$ .

It should be noted that there is a percentage of land area for which this system is not technically feasible with current technologies. Polar latitudes which have extremely long nights, particularly those more extreme the polar circle, would not be able to store enough energy for this entire night given current storage technologies. While other considerations such as technology performance at low temperatures would also be a concern for these locations, the length of the night currently provides a hard cap based on latitude for which the above analysis would be technically feasible.

### 3.4.2 Population with access to feasible land

More important than land fraction is the fraction of the population within regions with low-cost photovoltaics. Many regions with high irradiance values are also desert regions with low population densities. These locations may provide lower

cost energy due to higher output, however they would need expensive long-distance transmission lines to connect to load centers.

I identified the fraction of the world's population which would have access to low-cost energy from the coupled photovoltaic-storage facilities identified in Section 3.2. Figure 3.19 shows the locations which would be able to provide energy at a cost less than  $\$0.08/kWh_e$  for below-ground CAES storage facilities and varying array costs.

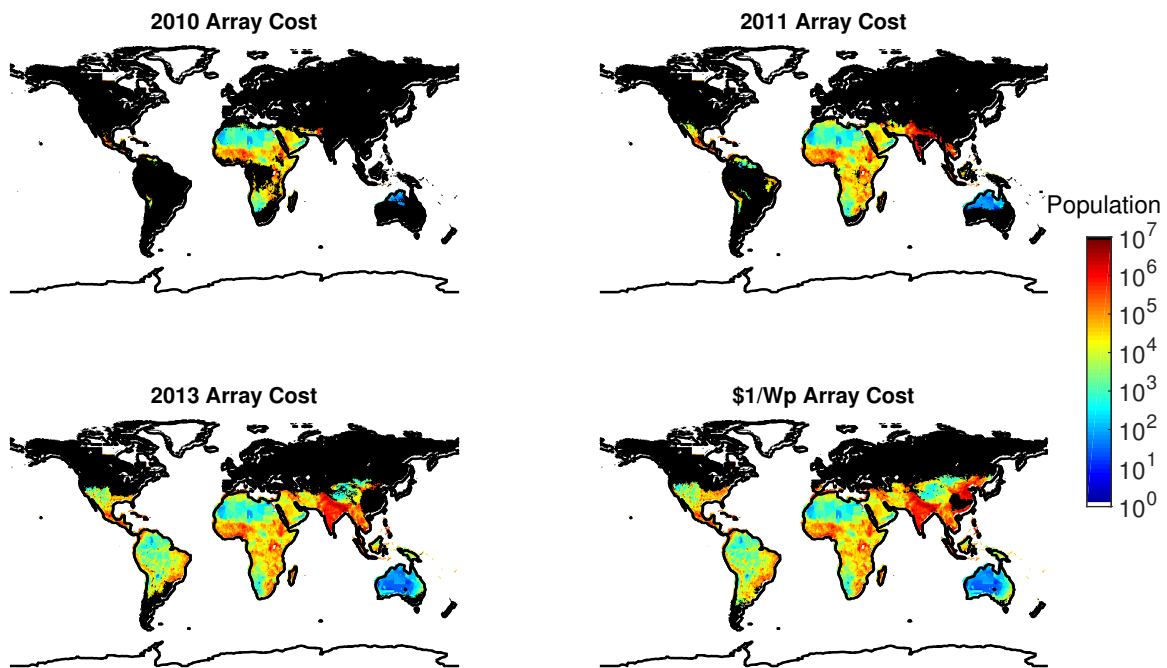


Figure 3.19: Areas with a cost  $< \$0.08/kWh_e$ , colored by the log of the population in that area

This is particularly illustrative as with the 2010 array costs a very small percentage of the world's population is able to provide low-cost PV-CAES energy. The locations with such low-cost energy are largely in Saharan Africa and Saudi Arabia. By 2013 however, the cost had dropped enough that India, south-east Asia, and the southern United States all show an energy cost of less than  $\$0.08/kWh_e$  from a coupled PV-CAES system.

Above-ground storage and batteries are not yet at a cost point where a majority of the world’s population would have access to low-cost energy from a coupled PV-storage facility. However, as the costs of these technologies drop it will become more feasible to use either of these technologies. Figure 3.20 shows the fraction of the world’s population that can provide energy at less than or equal to a particular cost for both the sodium-sulfur batteries and the U.S. Department of Energy goal technology.

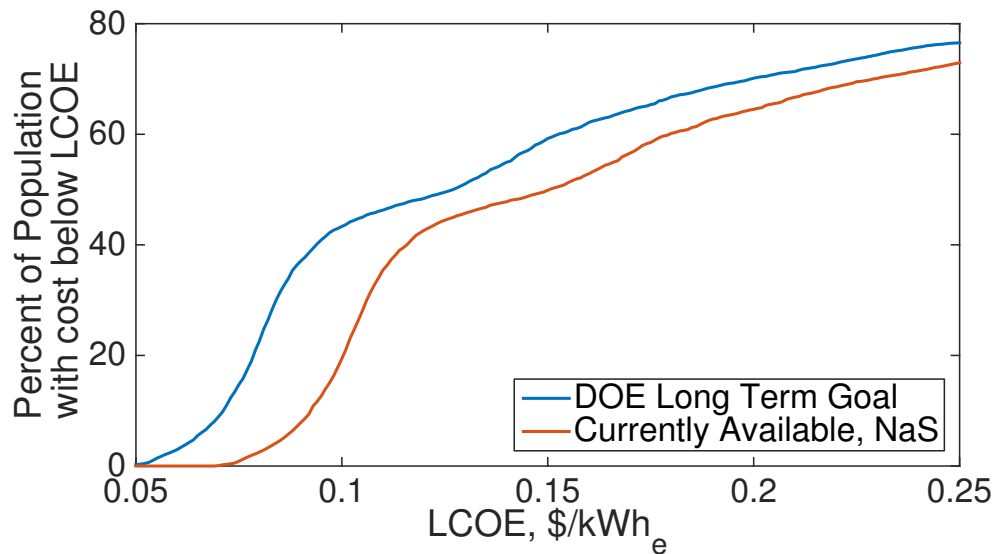


Figure 3.20: The percentage of the world’s population with access to energy from a PV-battery system at a cost less than a particular energy cost. This is shown for two battery systems, currently available sodium-sulfur batteries and the U.S. Department of Energy goal for battery costs.

The percentage of population with access to a particular energy cost is not linear, due to the nature of where global populations are situated. As can be seen in Fig. 3.20, a large portion of the population is on the cusp of having access to such low-cost energy, particularly if improvements in technologies allow for either increases in efficiency of batteries or reductions in cost of the system components.

Table 3.6 shows the percentages of the global population with access to energy from a coupled photovoltaic-storage facility at a cost less than  $\$0.08/kWh_e$  for each of

the storage technologies examined, at both the average array cost utilized in Section 3.2 and at  $\$1/W_p$ .

<b>Population Percentage with access to energy costs &lt; <math>\\$0.08/kWh_e</math></b>		
Storage Technology	Array Cost	
	Average	$\$1/W_p$
Below-Ground CAES	47.1%	71.0%
Above-Ground CAES	8.4%	47.4%
NaS Battery	0 %	2.5%
DOE Goal Battery	0.5%	22.6%

Table 3.6: The percentage of global population for which the life-cycle cost of energy is less than  $\$0.08/kWh_e$ , for each of the potentially storage technologies investigated. Both types of batteries are shown. The percentages are shown for both the average array cost assumed in this analysis as well as if the array cost were to drop to  $\$1/W_p$ .

While the concerns with technical feasibility at pole-ward latitudes discussed in sub-section 3.4.1 are also an issue for the population analysis, this is less of a concern when considering population as much of the world’s population do not live in these extreme latitudes.

### 3.5 Excess Energy

The model presented in Section 3.1 only accounts for energy provided directly to the grid via the coupled PV-CAES system. It does not utilize any energy in excess of 100 MWh in any hour, marking this energy instead as “excess”, and assuming that it would be utilized by other sources or directly sold on the grid. In some cases, this excess energy can be more than double the total energy provided directly from the array and storage facility, Figure 3.21

In the previous analysis, I assumed that this excess energy would be utilized in



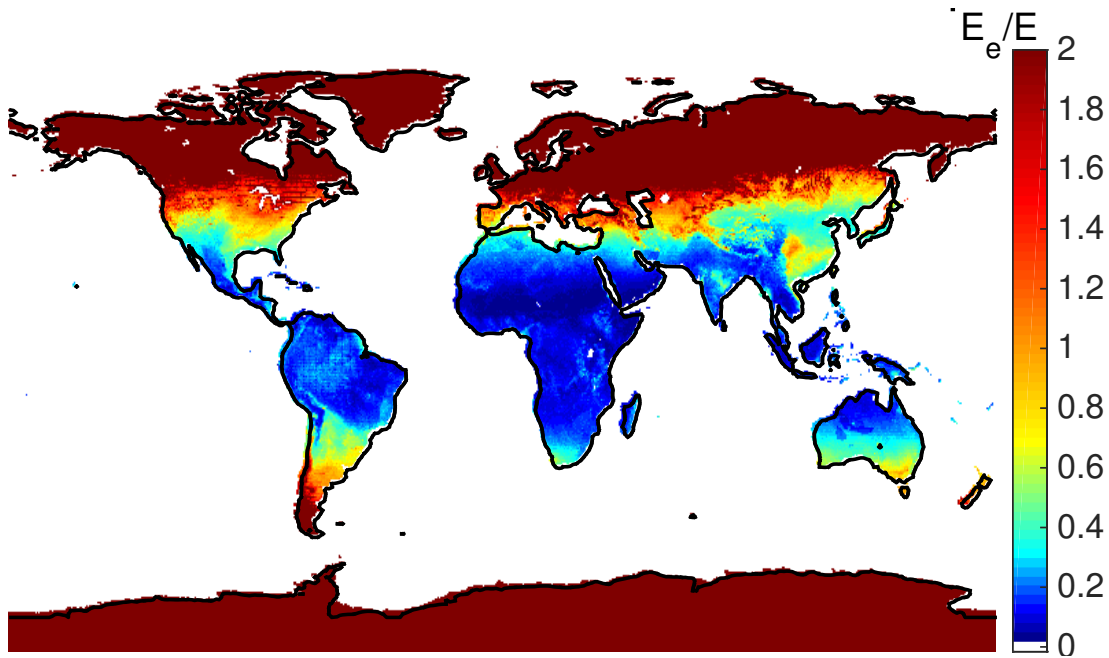


Figure 3.21: The total excess energy produced from the coupled system can in some cases be a large amount. This figure shows the ratio of excess energy to energy provided directly from the array and storage facility. Northern latitudes have higher excess due to the need to over-build for longer winter nights.

some manner, however did not perform an analysis of how it would be used. In reality, this energy would likely be sold to the electric grid on the real-time market, similarly to the current manner in which solar power is sold. If the electric grid operators were unable to utilize this energy, it would be curtailed. However, if it were sold on the electricity market it would generate revenue for the system owners. As noted in [151], solar power typically is high during on-peak times, providing a much higher compensation than wind power.

I have performed an analysis of a simple model for selling this excess energy on a typical electric grid and the potential additional revenue that could be acquired by doing so. I assumed that the energy provided would be a price taker, meaning its bid into the market would not influence the prices given at that time. This is likely a good assumption for locations with little excess, as the amount of energy sold would

not be a large percentage of the total energy on the grid and therefore would it would be unlikely to affect the price. In more northern locations where particularly in the summer time there would be large amounts of excess, as much as 500 or more MWh, this assumption is potentially less reasonable. The large influx of low-cost PV energy into the market could be of a high enough level to impact the electricity price at some times, resulting in lower energy prices overall [152]. While a possibility, I have however assumed that this would not be the case for this analysis.

I also assumed that the electric grid had enough flexibility in each hour to accept the energy and did not account for possible curtailment. This assumption, similarly to the previous assumption, is less likely to hold true at northern latitudes and also in locations without a stable electric grid. However, determining the degree to which the solar energy would be curtailed would require a much more extensive analysis concerning the energy and transmission resources at every location on the planet. Such an analysis was beyond the scope of this study.

Given these two assumptions, this analysis presents a high-end boundary on the additional revenue that could be expected to be gained by selling the excess energy provided from the coupled PV-CAES system described in Section 3.1.

I utilized real-time prices for U.S. independent system operators (ISO's), Fig. 4.2, for the pricing data of this analysis. For each U.S. ISO except for the California ISO historical real-time price data for the aggregated ISO were collected. Data for ERCOT were available from 2010-2014 [153], for MISO from October 2011 through June 2014 [154], for NYISO from January 2011 through March 2014 [155], for ISO-NE from 2008-2013 [156], for SPP from April 2008 through February 2014 [157], and for PJM from 2009 through 2014 [158].

I averaged these price data by hour and month for each ISO, creating an

average daily price profile for each month of the year for each ISO. This allowed for smoothing some of the daily volatility in prices while retaining the general trends seen throughout the year in each region. Figure 3.22 shows the monthly electricity price averages for ERCOT and PJM for two months of the year.

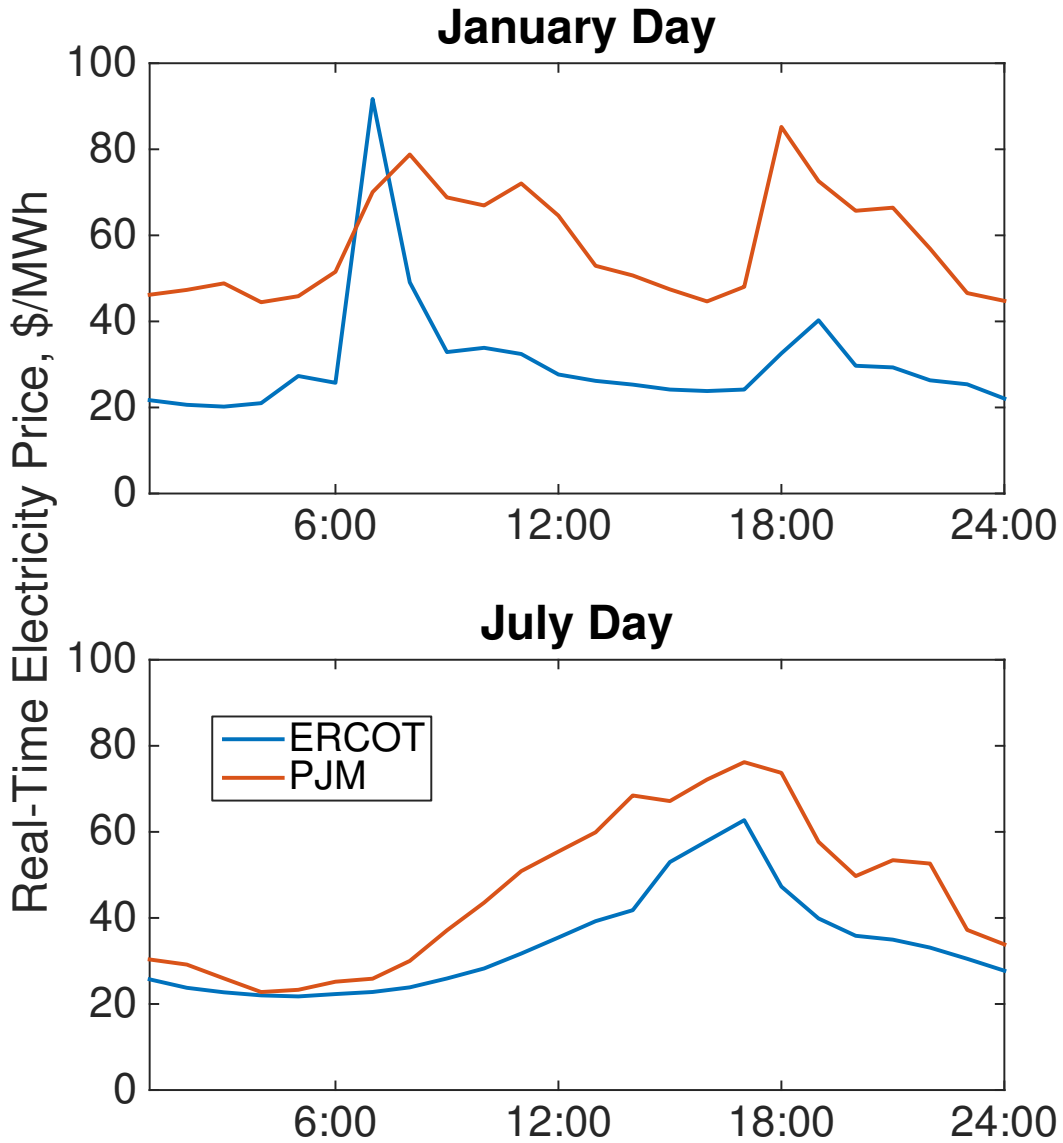


Figure 3.22: Daily average real-time electricity prices from two ISO's used in the analysis of excess energy revenue, ERCOT and PJM. The average price was determined hourly for each month of the year.

I modified the energy flow model presented in Section 3.1 such that at each hour, the excess energy  $E_e$  was multiplied by the price at that hour for each of the ISOs. The cumulative revenue from selling this excess energy at the averaged real-time price was tracked for each location.

In order to account for the effect of time and seasonality of energy pricing, the pricing data were shifted according to the approximate local solar time at each location. This was done by approximating the 24 time zones according to longitude. I also accounted for the difference in season by shifting the data by 6 months, such that the data utilized for January in the northern hemisphere were used for July in the southern hemisphere.

This approach assumes that electricity use patterns are based more on local daylight conditions and seasons than on political time zones. Behaviors are influenced by a complicated combination of political and geographical times, which is difficult to separate in a meaningful way. Realistically each location would have a different use and price pattern that would shift more gradually than the distinct hourly bands. However, as this analysis uses two representative price curves to identify possible outcomes rather than specific local data, this method was deemed acceptable. It should be noted that this approach does lead to artifacts at the boundaries due to hard cut-offs between each hour and the hemispheres.

I utilized the average prices from two ISOs in order to analyze the potential differences varying price curves would have on the data. Specifically data for PJM and ERCOT were used for this analysis. These regions represent areas with different pricing characteristics in the summer versus winter, and also variable structures throughout the day, Fig. 3.22. Together they present a set of representative price data for use in this analysis.

The total additional revenue computed was potentially up to \$10 billion for locations with significant excess energy, however most locations have additional revenue of less than \$2 billion. Africa, which has very little excess energy, has the lowest overall excess, typically less than \$0.5 billion. This revenue represents nominal revenue, as the revenue was not discounted. ERCOT price curves lead to larger additional revenue than PJM price curves, likely due to the high summer peak of the ERCOT system. Figure 3.23 shows the global map of the additional revenue that could be expected over the lifetime of the system.

It should be noted that these prices are not representative of current markets across the world, specifically regions such as Africa do not have markets at this scale. However, this analysis looks forward to a future in which these facilities might exist inside of a larger grid system with electricity markets instead of stand-alone facilities operating independently.

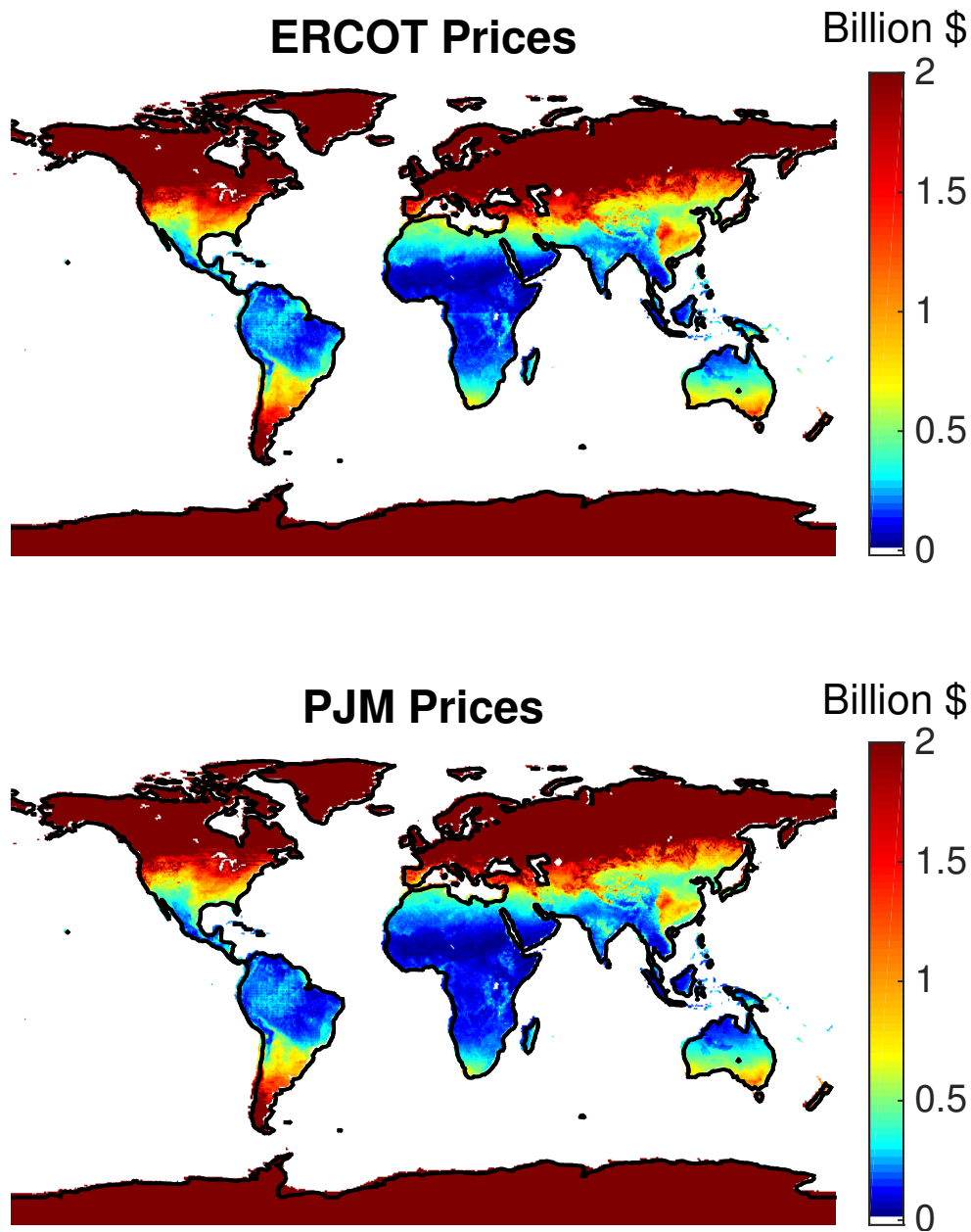


Figure 3.23: Additional revenue that could be expected from a base-load generating PV-CAES facility. The revenue was calculated for two different pricing data sets to show potential differences in prices used. Slight differences in total revenue can be seen, however both prices lead to potentially large additional revenue streams for these facilities.

## Chapter 4

### Load Following with Photovoltaics

The energy flow model discussed in Section 3.1 was assumed to provide constant base-load output from the coupled photovoltaic array and storage facility. However, the output of solar power systems rises and falls during the day with peak output often only slightly out of phase with peak load requirements. As a result, coupling solar power systems with grid-scale energy storage could more beneficially provide a dispatchable source of electricity for load following.

Solar irradiance peaks in the mid afternoon and falls to zero overnight, requiring the use of stored energy, which is also needed at dawn, dusk, and during cloudy time periods. Typical demand curves, e.g. Figure 4.1, also tend to peak during the day and drop overnight. Following these profiles will typically require less energy storage to provide the same yearly capacity factor than would be required with systems providing baseload electricity due to lower night-time requirements.

As a result, using photovoltaics and compressed air energy storage to match specific load profiles could have lower capital costs, potentially providing a lower electricity costs. In addition, compressed air energy storage systems typically burn natural gas to preheat the air before it passes through turbines that recover the stored energy. As a result, systems designed to load follow can have lower carbon signatures than systems optimized for baseload electricity production.

Providing dispatchable power from a photovoltaic array would help alleviate concerns about grid stability. While I previously investigated the ability to provide

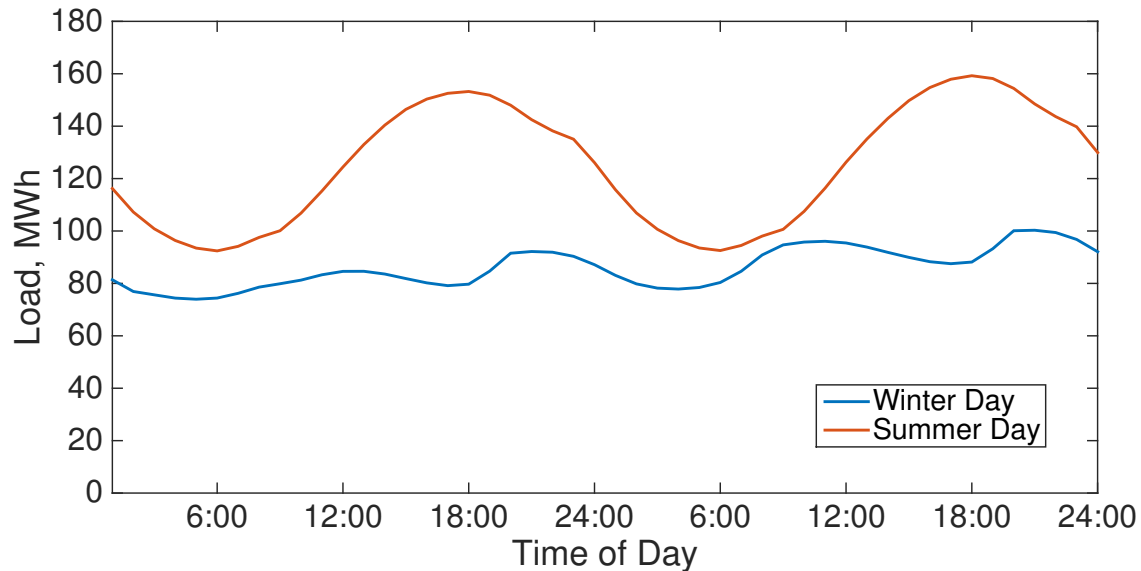


Figure 4.1: Typical load curve for two days for the Electric Reliability Council of Texas, which provides electricity to most of Texas. Two curves are shown, representing example days from both the winter and summer months. The load was scaled to provide 876,000  $MWh_e$  per year.

dispatchable power in the form of base-load energy, dispatchable power can also be provided to match demand, or according to the requirements of the electric grid. Solar power could achieve a large benefit from providing dispatchable power in a manner which more closely matched the output from the solar array, therefore requiring smaller storage facilities and potentially having a lower cost of energy.

I here analyze the total energy that could be provided from the same system following each of four load curves. These load curves include baseload output, on-peak output, and following either an average summer peaking load, or an average load that peaks in both the winter and summer. The total energy provided for each load curve is analyzed and compared. This is done for 8 different storage amounts to examine how energy provided by each load profile changes with increasing storage.



## 4.1 Load Data

To generate representative load profiles I aggregated historical load data from the independent system operators (ISOs) across the United States. Specifically, I was able to obtain data from California ISO (CAISO), Electric Reliability Council of Texas (ERCOT), Midwest ISO (MISO), New York ISO (NYISO), ISO New England (ISO-NE), Southwest Power Pool (SPP), and PJM Interconnection (PJM). Figure 4.2 shows the regional coverage of the different ISO's in the U.S. [159]. Data were not available for regions not covered by ISO's.

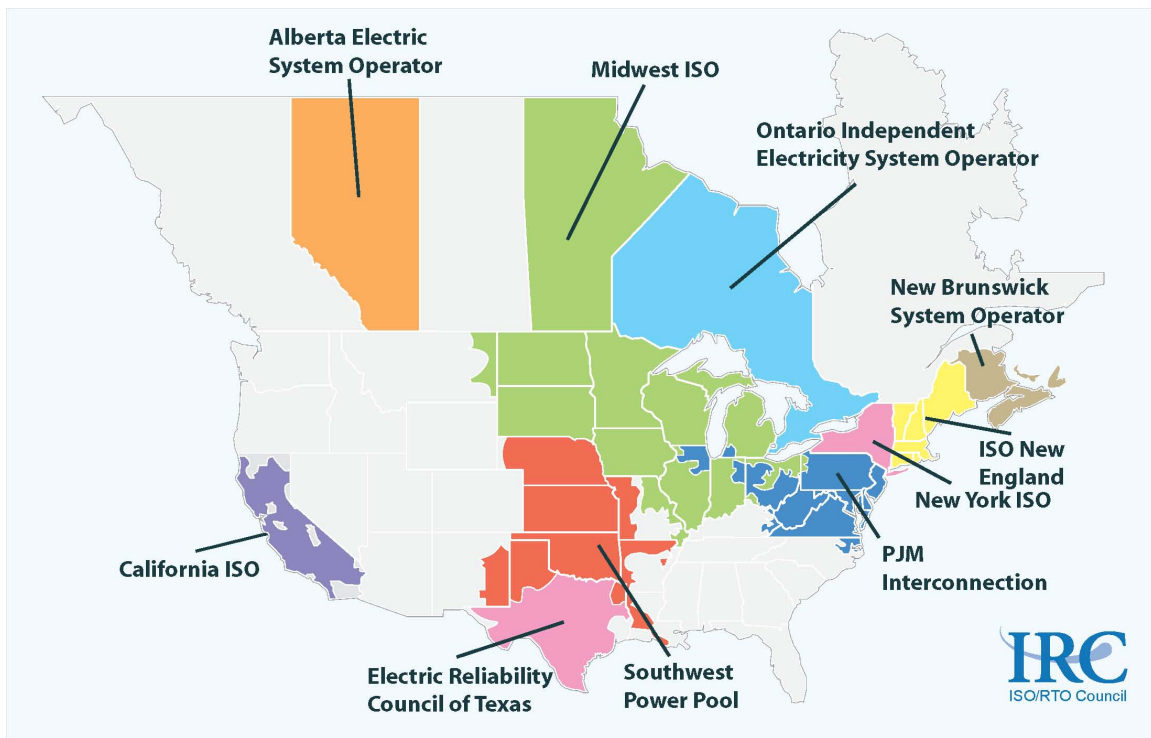


Figure 4.2: There are seven different independent system operators (ISOs) in the United States. This map shows their coverage [159].

For each of these ISO's I collected historical real-time load data for the aggregated ISO area. Data for CAISO were available from January 2, 2011 through December 31, 2014 [160], for ERCOT from April 16, 2003 through December 31,

2013 [161], for ISO-NE from January 9, 2008 through December 31, 2014 [162], for MISO from January 1, 2007 through December 31, 2012 [163], for NYISO from January 1, 2008 through December 31, 2013 [164], for PJM from January 1, 2000 through December 31, 2013 [165], and for SPP from January 1, 2010 through December 31, 2013 [166].

For each ISO the data were averaged for each hour of the year to create an average year’s hourly demand profile. The data were then scaled such that over the course of the year each ISO provides the same total energy. This was done to highlight the different shapes of the load profiles, rather than the sizes of each ISO. Figure 4.3 shows the yearly cycles of these values by aggregating hourly values to 24-hour averages.

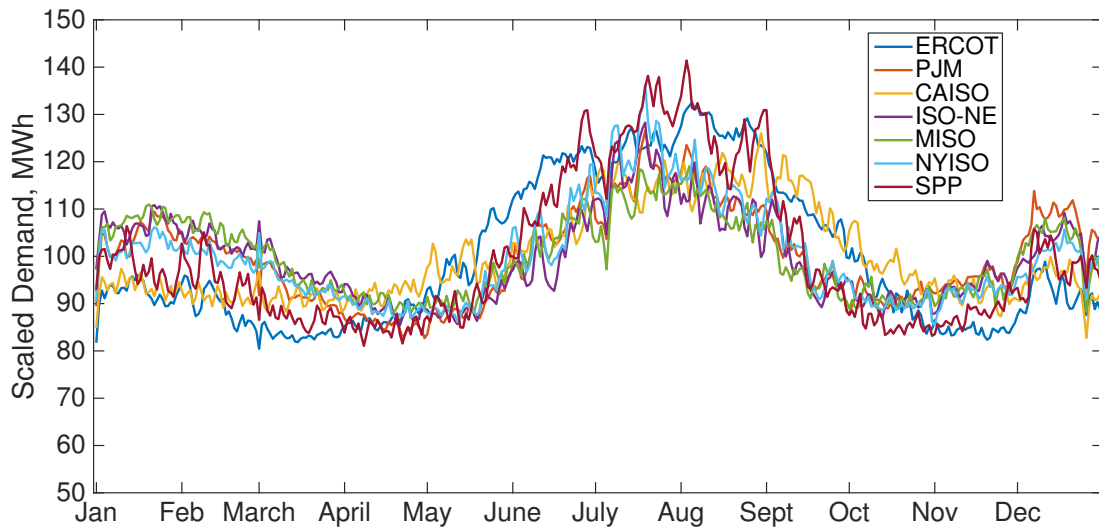


Figure 4.3: Variation in daily demand profiles for the seven ISOs serving the United States. I aggregated the load for the 7 ISO’s in the U.S. and then averaged this value for each day of the year. In order to more clearly show the yearly changes, this figure shows the 24-hour average load instead of the hourly load for each region.

Load profiles from ERCOT and PJM were used to examine the ability of the coupled systems to load-follow. These systems were chosen because they are both larger systems that showed different yearly demand cycles, and so represent two

disparate examples of when power might be required from this system. ERCOT has a high summer peak and low winter demand. PJM shows a double peak in both the winter and summer time due to increased heating and lighting loads in the winter. Figure. 4.4 show the variation in the average daily electricity demand specifically for ERCOT and PJM during the year.

Due to higher demand during the day, many load following plants will operate only for specific hours of the day. Here I assume an on-peak load profile with a fixed output of  $150 \text{ MWh}_e$  for each hour between 6 am and 10 pm, and zero otherwise. Representative ERCOT and PJM load curves for winter and summer days are shown in Fig. 4.5, along with on-peak and baseload profiles, with each scaled to provide  $876,000 \text{ MWh}_e$  of energy in one non-leap year.

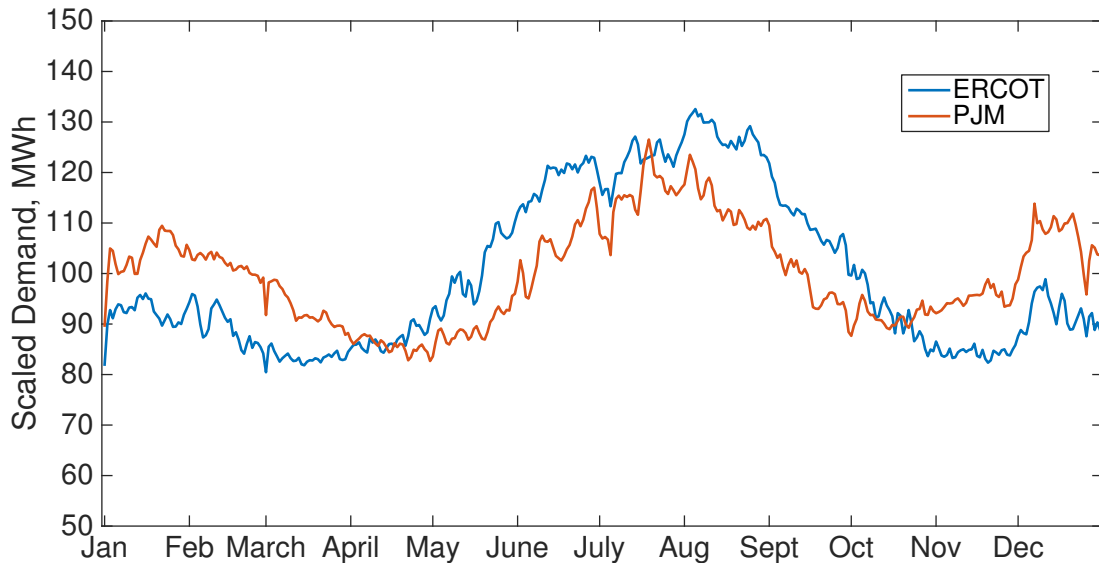


Figure 4.4: Twenty-four hour average load profile for ERCOT and PJM, the regions focused on in this analysis. The data were scaled such that each curve provides the same energy over the course of a year.

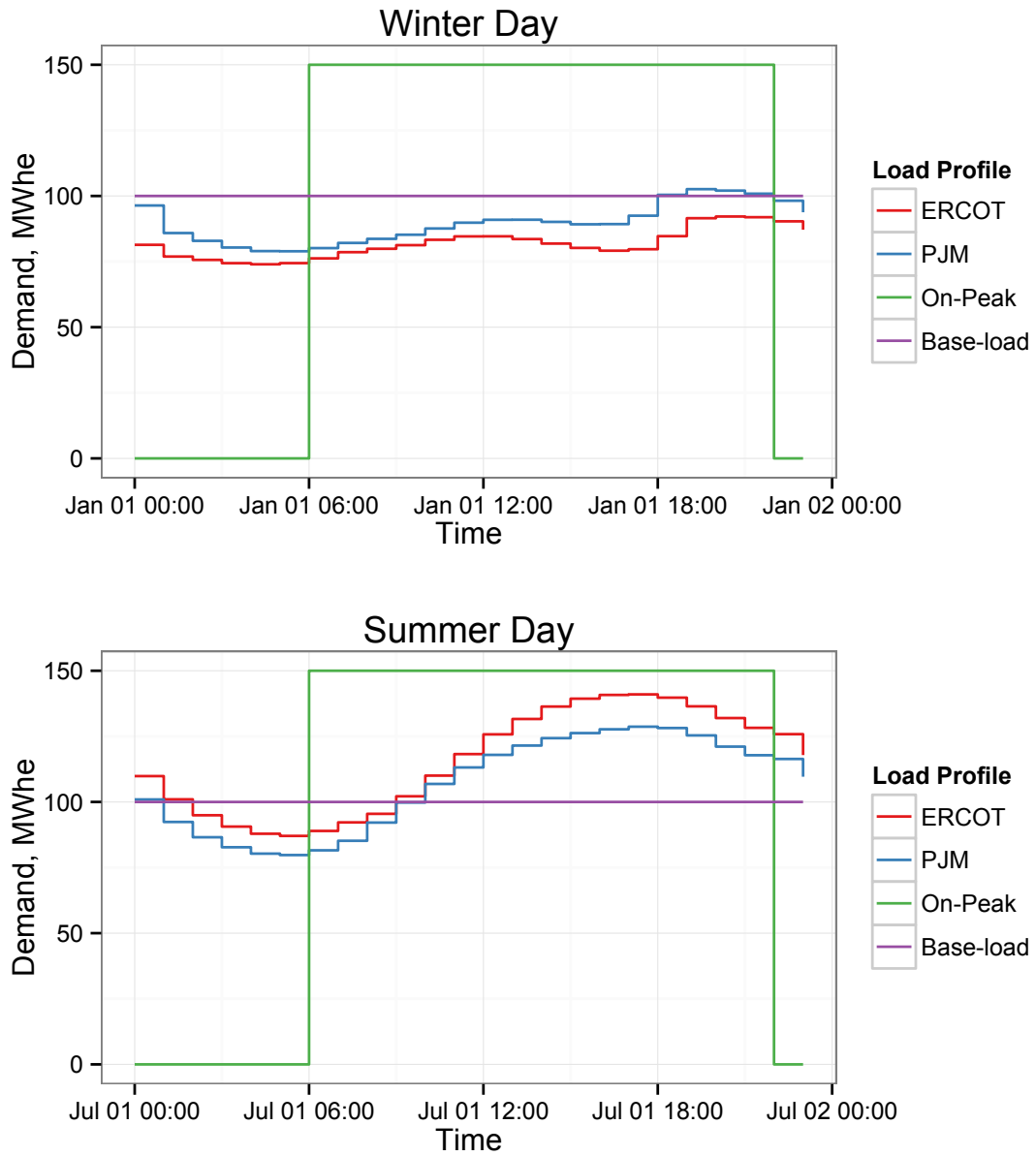


Figure 4.5: Daily load profiles for each of the four dispatchable loads utilized in this analysis. Both a summer and winter day are shown. All loads are scaled such that the yearly output is the same for all profiles.

## 4.2 Methods

The energy flow model used as in Section 3.1 was modified to allow a variable output depending on which load curve was being followed. Similarly to Section 3.1, the total output from the photovoltaic array is computed for each hour,  $i$ , as:

$$E_i = \frac{I(i) * (1 - R(t))}{1000 W_p/m^2} W_A \quad (4.1)$$

where  $E_i$  [J] is the energy produced in that hour,  $I(i)$  [W] is the surface solar irradiation at hour  $i$ ,  $W_A$  [ $W_p$ ] is the rated capacity of the array, and the factor of  $1000 W_p/m^2$  is a factor for determining the rated capacity for photovoltaic modules, used to standardize their ratings [120]. Equation. (4.1) is computed for the start of each hour of analysis, determining the energy available for that time step.

In each hour the energy required by the grid is a variable amount determined by the load curve being followed, represented as  $E_d(i)$  for each hour  $i$ . Each load profile was scaled such that each provides the same amount of energy over the course of a year, specifically 876,000  $MWh_e$  in a non-leap year. The system did not provide more energy than was required by the particular load profile being followed; any additional energy produced by the array that could not be stored was counted as excess energy as in the baseload analysis.

The energy produced by the array is again partitioned into three components:

$$E_i = E_g + E_s + E_e \quad (4.2)$$

where  $E_g$  [J] is the energy sent directly to the local grid to meet base-load electricity needs and  $E_s$  [J] is the energy directed into storage. When the storage is full and the array is producing more than the required demand  $E_d(i)$ , the excess electricity  $E_e$  [J] is available for broader use. I calculate  $E_g$ ,  $E_s$ ,  $E_{fs}$  and  $E_e$  in each hour according to

$E_i$  and  $E_d(i)$  as:

$$\begin{aligned}
E_g &= \begin{cases} E_d(i) & E_i \geq E_d(i) \\ E_i & E_i < E_d(i) \end{cases} \\
E_{fs} &= \begin{cases} 0 \text{ MWh} & E_i \geq E_d(i) \\ E_d(i) - E_i & E_i < E_d(i) \end{cases} \\
E_s &= E_i - E_d(i) & E_i \geq E_d(i), \text{ storage not full} \\
E_e &= E_i - E_d(i) & E_i \geq E_d(i), \text{ storage full}
\end{aligned} \tag{4.3}$$

The load-following model utilizes the array and storage sizes that were determined in Section 3.1, which provides 100  $MW_e$  base-load output with a capacity factor  $\geq 90.7\%$ . The array size was then held fixed and the storage capacity at each location was varied between 10-200% of the storage capacity for the previously analyzed baseload system to identify how the ability to meet a particular load varied with storage capacity. The storage capacity producing the lowest cost electricity was identified for each load profile.

In order to account for hourly differences in energy use, the demand data were shifted according to the approximate local solar time at each location. This was done by approximating the 24 time zones according to longitude. I also accounted for the difference in season by shifting the data for the southern hemisphere by 6 months, so that the data utilized for January in the northern hemisphere were used for July in the southern hemisphere.

For each load profile the coupled systems are scaled to provide 876,000  $MWh_e$ /year and I assume for each hour  $E_g + E_{fs} \leq E_d$ . The capacity factor is then defined as:

$$CF = \frac{\Sigma_{year}(E_g + E_{fs})}{876,000 \text{ MWh}e} \tag{4.4}$$

Excess energy,  $E_e$ , is assumed to go to peak power demand, or out onto a broader grid, and does not contribute to the capacity factor.

I computed the energy provided throughout the year by each load profile, in addition to the lifecycle energy cost. This was done for eight different storage amounts in order to compare the effect of increasing or decreasing the storage capacity. The base level storage amount was determined according to the analysis of Section 3.1 as a reference point. This capacity was then multiplied by different factors in order to increase or decrease the total storage amount.

The cost of each of the eight facilities was calculated according to the cost equations, Eq. (3.8) – (3.12) presented in Section 3.2, and the energy cost computed in Eq. (3.16).

The carbon emissions for each system and load profile were also computed. This was done using Eqs. (3.19) – (3.21) from Section 3.3.

### **4.3 Results**

For the time dependent load profiles, optimization of the coupled systems of energy storage and photovoltaics assumed that the loads shift with local daylight conditions, which is an idealization. In reality, load profiles are also affected by season, weather, social and industrial patterns. Each location would have a different use pattern as a result. However, the on-peak profile would be encountered even with such region to region variations, as would the baseload profile. The ERCOT and PJM load profiles are representative of a western economy in temperate and subtropical regions.

Figure 4.6 shows the geographical distribution in which each load profile produces the lowest levelized cost of electricity. The distribution is shown at six different levels of storage capacity, relative to the optimum for baseload electricity production. On-peak and ERCOT load profiles produced the lowest cost of electricity across a wide range of storage sizes, with on-peak dominating at low storage levels

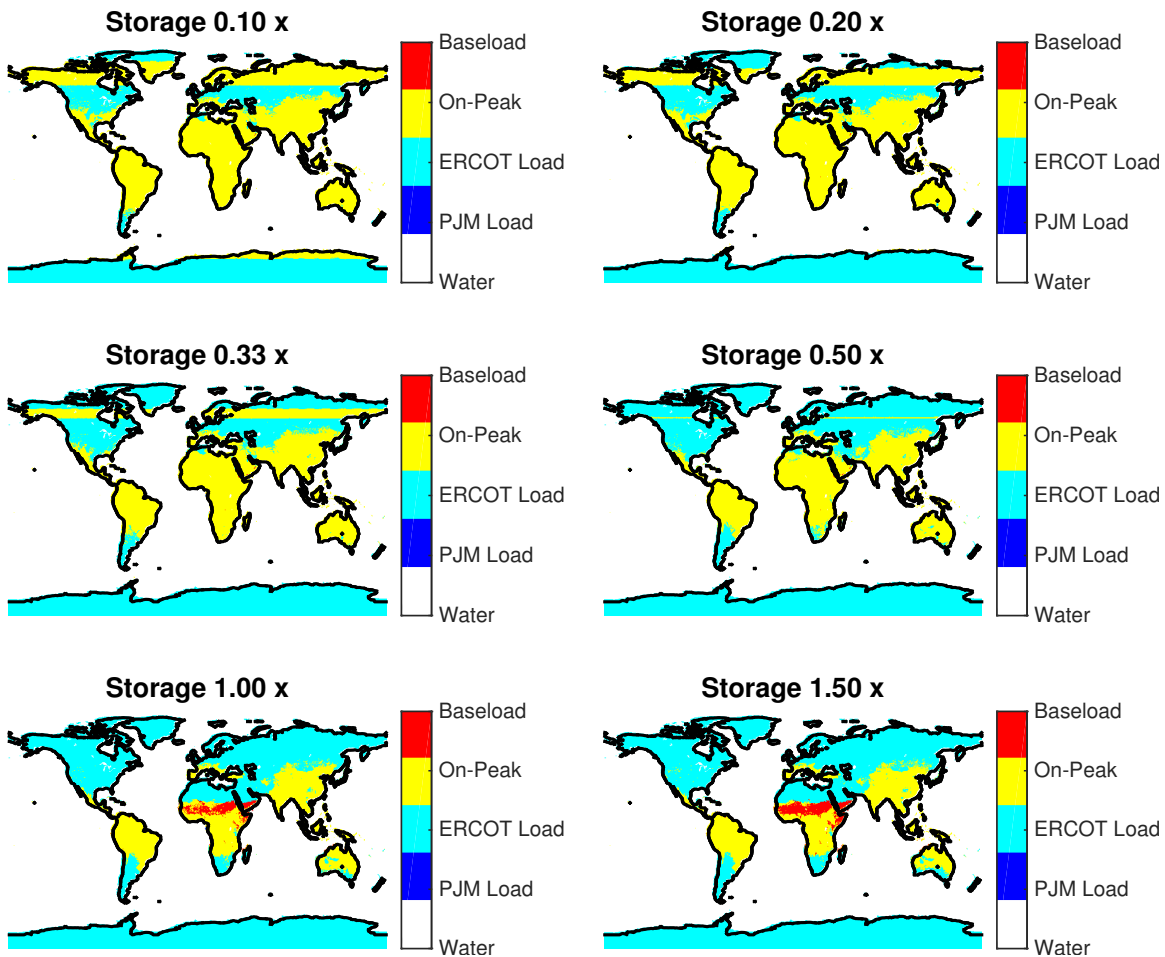


Figure 4.6: The energy cost from each of four load profiles was determined for eight different storage amounts, all multiples of a base-level storage capacity. This figure shows for four of these storage capacities, which load profile provided the lowest cost energy.

and ERCOT at higher levels. However, we also found that as the storage capacity increased, there were regions in which the base-load load profile was actually the cheapest, particularly in Africa.

Figure 4.7 shows the storage capacities required to produce the minimum levelized cost of electricity for each load profile. I found that the on-peak load profile required the lowest of storage, up to  $2000 MW_e$  less than the lowest cost base-load configuration.



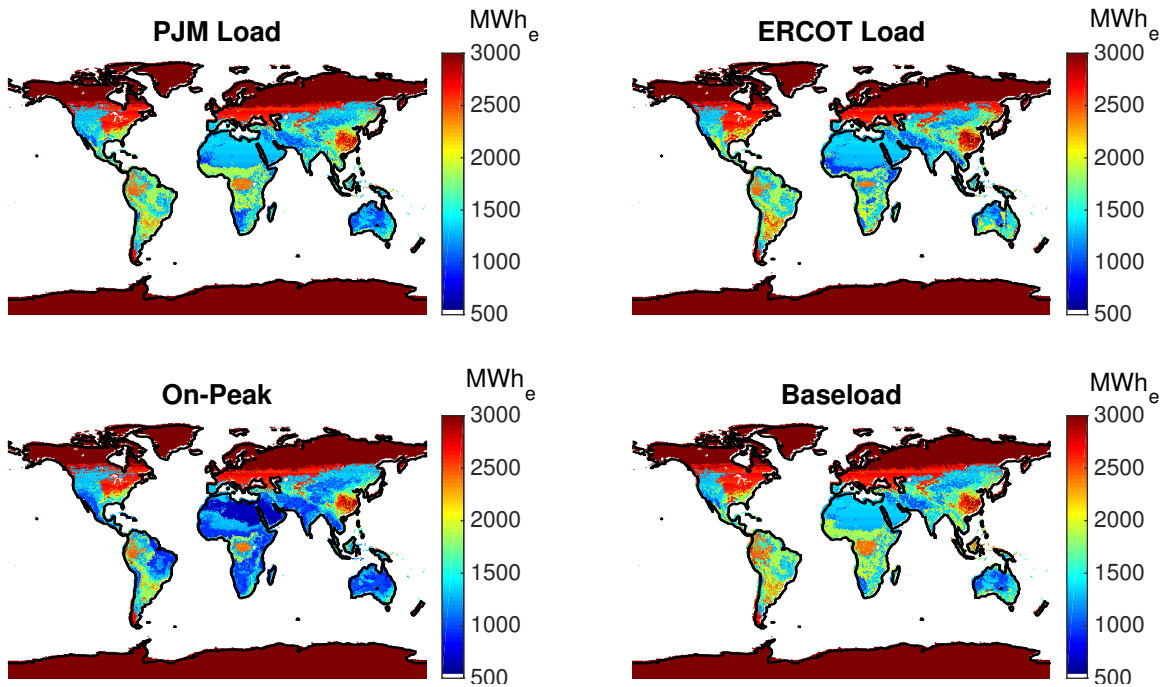


Figure 4.7: The minimum energy cost from each of four load profiles was determined. The storage amount for this minimum cost is shown here for each load profile. The On-Peak load profile tends to have the lowest storage requirement.

A major motivation for the adoption of renewable energy systems, photovoltaics included, is their ability to provide low-carbon electricity. The compressed air energy storage systems considered here were assumed to burn natural gas to preheat air before it was decompressed through turbines to recover stored energy. Because the on-peak load profile required the least storage to produce a minimum in the levelized cost of electricity, it also gave the smallest carbon intensity. This has a benefit of reducing the green-house gas emissions from the coupled system. The on-peak load profile showed the greatest reduction in carbon emissions, up to 30% from base-load generation. The load curves from PJM and ERCOT both saw up to 17% reduction in carbon emissions. Figure 4.8 shows the percent reduction in carbon emissions between base-load use and each of the other three load curves analyzed.

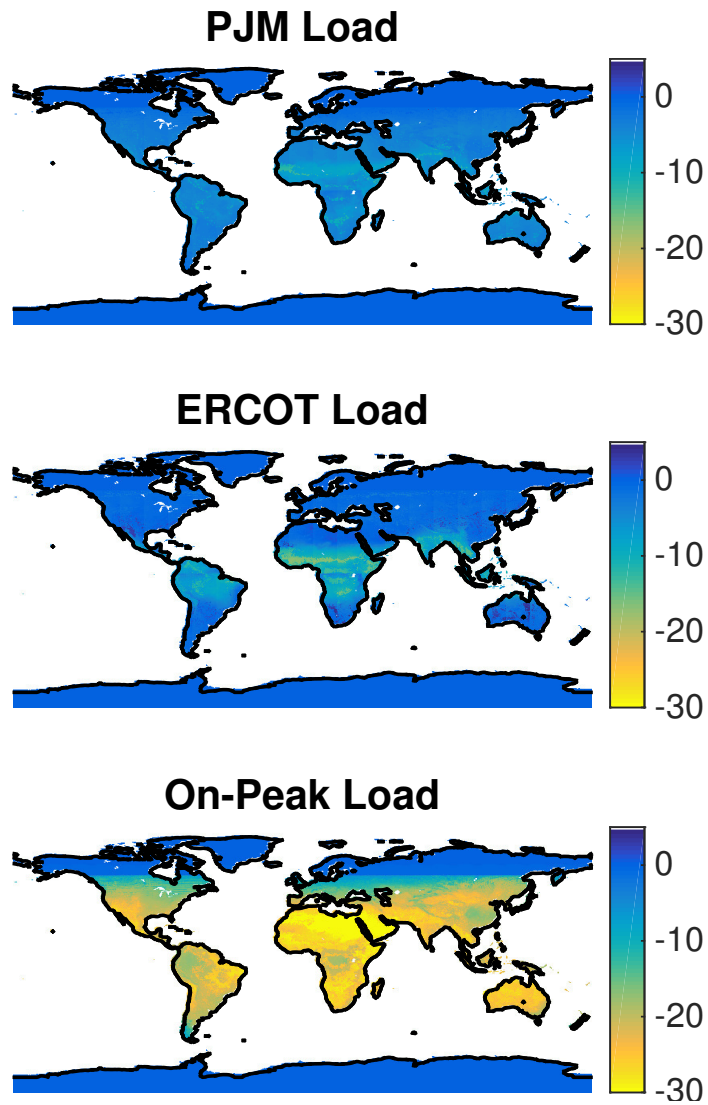


Figure 4.8: The total carbon emissions from load following show a reduction over base-load use due to a reduction in use of energy from storage. The percent reduction in carbon emissions for each load profile compared to the base-load use is shown.

## Chapter 5

### GIS Multi-criteria Decision Analysis

Solar power, a low-carbon fuel source, has seen a large increase in installed capacity, partly due to rapidly dropping costs. An important question for governments and aid organizations interested in solar power is where to install these facilities. While cost is a strong concern, also of importance is where the facility will provide the most benefit to the population. Locations expected to provide energy at the lowest cost do not necessarily correspond to load and population centers, where the energy is most useful. In order to garner the greatest social benefit from a solar power facility, the cost in addition to need for low-carbon energy sources must be evaluated.

I here perform an analysis of the optimal locations for solar power facilities on a global scale, accounting for the full system cost, siting capability, as well as socio-political factors that indicate a need for low-cost energy. While studies have examined the feasibility of siting these facilities, none have looked globally at locations that could provide a large benefit to society in the form of low-cost electricity. I utilize the multi-criteria decision analysis framework to identify key locations where low cost base-load solar power facilities correspond with high population areas and with socio-political factors indicating a need for low-cost energy. This is done for two separate characteristics of social benefit, including locations with high growth in electricity use and secondly locations with low grid connectivity levels.

I found that the most ideal locations for the first definition of social benefit are generally located in Africa, followed by Iraq, India and South America, as these

locations have both high irradiance levels as well as expanding electricity needs. The second analysis is dominated by most of Africa, which has a very low fraction of the population with access to electricity. I present maps showing the ideal locations for both of these analyses.

## 5.1 Background

As the costs of solar photovoltaics continue to drop [30,88], it will become more economical to utilize solar power as a low-carbon source. The expansion of renewable energy technologies is being promoted as a means to limit carbon emissions, with dramatic effect [2, 21, 25, 61]. Between 2007 and 2013 the global installed capacity of solar power facilities grew an average of 55% annually, to a total of 139 GW [18]. An increasingly important question is where to build future facilities. Many studies have investigated the siting of solar power facilities [167, 168]. However, they have typically looked only at the feasibility of building in particular locations, and the studies have tended to be localized to particular geographical regions. To date, none have performed an analysis of socially beneficial locations, particularly on a global scale. Doing this is complicated by the many factors that must be considered when choosing site locations.

Multi-criteria decision analysis (MCDA) has been widely utilized since the late 1990's to analyze complex questions involving many variables [169, 170]. When coupled with geographic information systems (GIS), it provides a framework for analyzing spatially dependent problems, such as identifying ideal desalination sites [171], potential nuclear waste facility locations [169], forest conservation planning [172], power plant siting [167, 168], as well as investigating many other environmental and locational questions [170, 173–175]. Analyses such as these typically have several, often competing,

requirements and identifying what is optimal is rarely straightforward. Multi-criteria decision analysis can be used in combination with geographical information systems to comprehensively assess how diverse sets of decision variables affect siting decisions for things such as power facilities [170, 173, 174].

Due to high insolation levels, solar power tends to have the lowest cost in desert locations [42]. However, these locations are typically far from population centers and transmission lines are often missing. Identifying the most advantageous location for a solar power facility therefore should include considerations beyond a simple cost or siting analysis. Geographical information systems data provide a means with which to identify feasible locations with an optimal combination of low-cost energy and high social benefit. Here I define social benefit as the provision of low-cost, low-carbon energy to populations with a high need for electricity. These populations consist of two separate groups with differing needs for electricity, the first with a high-expected expansion, and the second with no current access.

High-expected expansion is characterized by a high expected growth in electricity use. Areas with these characteristics will have a growing need for electricity if their living standards are to remain stable, let alone increase. A lack of current access to electricity is endemic to much of the developing world, and is widely regarded as a drag on economic expansion [176]. Increases in electricity access has been linked to growth in income, productivity, and growth in social services [177]. Access to electricity can also provide easier access to drinking water and light and can be particularly beneficial for women, whose daily tasks can be eased with electricity [178]. Additionally, a correlation has been found between literacy rates and electrification of rural areas [179].

Here I present a global analysis of the optimal locations for solar photovoltaic

facilities coupled to compressed air energy storage facilities. I account for the feasibility of siting these facilities by incorporating terrain slope, proximity to wetlands and 100 year flood plains, and geology with potential for compressed air energy storage facilities. To determine social benefit, I performed two separate analyses, utilizing full system cost, global population, and either expected growth in population or electricity demand. These analyses each show high benefit through high need, measured in two separate ways. I use a multi-criteria decision analysis framework in conjunction with geographical information systems to determine feasible locations with low cost and high social benefit.

## 5.2 Methods

Spatially defined data were used to identify potential siting issues and to categorize the social benefit of photovoltaic installations collocated with grid-scale energy storage. Exclusion criteria for these coupled facilities included geology lacking the potential for below ground energy storage, high terrain slope, high population density, and co-location in wetlands or 100 year flood plains. Land use was not used as an exclusion criteria because photovoltaic modules could be placed on rooftops of buildings [39, 180] or collocated with agricultural land. Protected areas are assumed to already be excluded due to lack of population, which is used in the social benefit score.

Variables indicating social benefit included the levelized cost of electricity from the coupled facilities, population per pixel, and either expected growth in electricity demand or lack of access to electricity. For each location, each variable was scaled to a value between 0 and 1. The lower the value, the more ideal the location is for that variable. Table 5.1 summarizes the siting variables and the ideal conditions.

Data	Variable Type	Criteria for ideal	Reference
CAES Geology	Exclusion	Salt Dome, Sedimentary Basin, or Hard Rock	[42, 124]
Land Slope	Exclusion	Slope < 3%	[180, 181]
Wetlands	Exclusion	Not Wetland or Flood Plain	[182, 183]
Population Density	Exclusion	Density < 500 persons/km <sup>2</sup>	[167, 184]
Population, persons	Social Benefit	Higher Population	[185]
Energy Cost, \$/kWh <sub>e</sub>	Social Benefit	Lower Cost	[42]
Electricity Growth, %	Social Benefit	Higher Growth	[186–188]
Access to Electricity, %	Social Benefit	Lower Access	[189]

Table 5.1: Criteria used for MCDA analysis, distinguished by siting or social benefit criteria. Variables used as exclusion criteria are not included in the score computed for each location. Regions with one or more exclusion criteria are assumed to be unable to site these facilities, and are not included in subsequent analyses.

The data were processed and aggregated into equal-angle pixels of  $0.5^\circ \times 0.5^\circ$  to match the resolution of the energy cost data set. Data on population, population density, land slope, wetlands and subsurface geology were available either at this resolution or at a higher resolution, in which case they were aggregate to  $0.5^\circ \times 0.5^\circ$ . The data sets for expected electricity growth and grid connectivity were available at a country level, and a constant value used for each  $0.5^\circ \times 0.5^\circ$  pixel within the respective countries.

All analysis was performed in Matlab using an equal angle grid of resolution  $0.5^\circ \times 0.5^\circ$ . All data were available in a format read-able by Matlab, except for Wetlands data. These data were filtered through the geographical information system GRASS [190] and converted to ascii format, which was then used in Matlab.

For each pixel, a score  $x_i$  was computed for each variable, ranging from 0 to 1. The population and growth in electricity usage were scaled from the highest value:

$$x_i = \frac{V_{max} - V}{V_{max} - V_{min}} \quad (5.1)$$

and energy cost and access to electricity were scaled from the lowest value:

$$x_i = \frac{V - V_{min}}{V_{max} - V_{min}} \quad (5.2)$$

In Eqs. (5.1) and (5.2),  $x_i$  is the scaled value of the  $i^{th}$  variable,  $V$  is the variable's value at a particular location, and  $V_{max}$  and  $V_{min}$  are the maximum and minimum values of  $V$ .

A total score,  $X$ , for each pixel was then calculated as:

$$X = \sum_{i=1} w_i x_i \quad (5.3)$$

where  $w_i$  is the weight of each variable. Equal weighting was used for this analysis as there was no strong motive for ranking of the criteria. Scores were only calculated for locations not excluded under the exclusion criteria.

Figure 5.1 summarizes the multicriteria decision analysis process used in this analysis.



Figure 5.1: MCDA process overview

## 5.3 Data Description

### 5.3.1 Geology

While above-ground compressed air and battery storage are technically feasible, they are currently more expensive than would be below ground compressed air energy



storage, Section 3.2. Site geology is included in the siting variables to capture this. Grid-scale compressed air storage has been demonstrated in salt formations [49], but it is also feasible in hard rock and sedimentary basins.

Figure 5.2, reproduced from Section 3.1, shows the distribution of geological formations where below ground air storage could potentially be sited. The data are based on an aggregation of the units on the Geologic Province Map (<http://earthquake.usgs.gov/data/crust/maps.php>) created by the US Geological Survey, which was digitized and re-projected onto a  $0.5^\circ \times 0.5^\circ$  grid. The salt distribution comes from data compiled for Applied Geodynamics Laboratory at the Bureau of Economic Geology [124]. This higher resolution data was projected onto the  $0.5^\circ \times 0.5^\circ$  grid along with the aggregated US Geologic Survey map data.

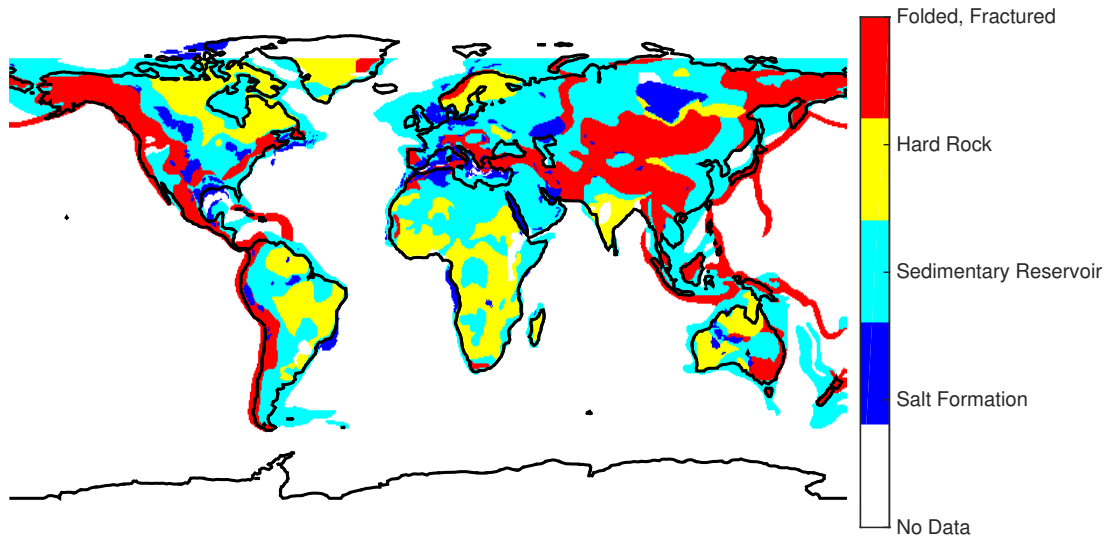


Figure 5.2: Distribution of geology with potential for below ground compressed air energy storage. Salt formations, hard rock, and sedimentary reservoirs have potential for supporting below ground compressed air energy storage [42, 124].

### 5.3.2 Land Slope

Large-scale photovoltaic arrays are most easily built in areas with a slope of less than 3% [180]. I used elevation data from the Shuttle Radar Topography Mission (SRTM), which provides elevation data at 90 m resolution for all land areas not including Antarctica and latitudes above 60°N [181], to determine the land slope in each pixel. The highest and lowest point within each 0.5° x 0.5° pixel were identified, and the difference was divided by the length of the pixel in order to identify a lower boundary on the slope within that pixel. This is a coarse method for determining the slope of a region, and locations could exist within a particular pixel that would allow for siting a solar array, however this method was used as an approximation given the granularity of other data, Table 5.1. Figure 5.3 shows the global estimated land slope.

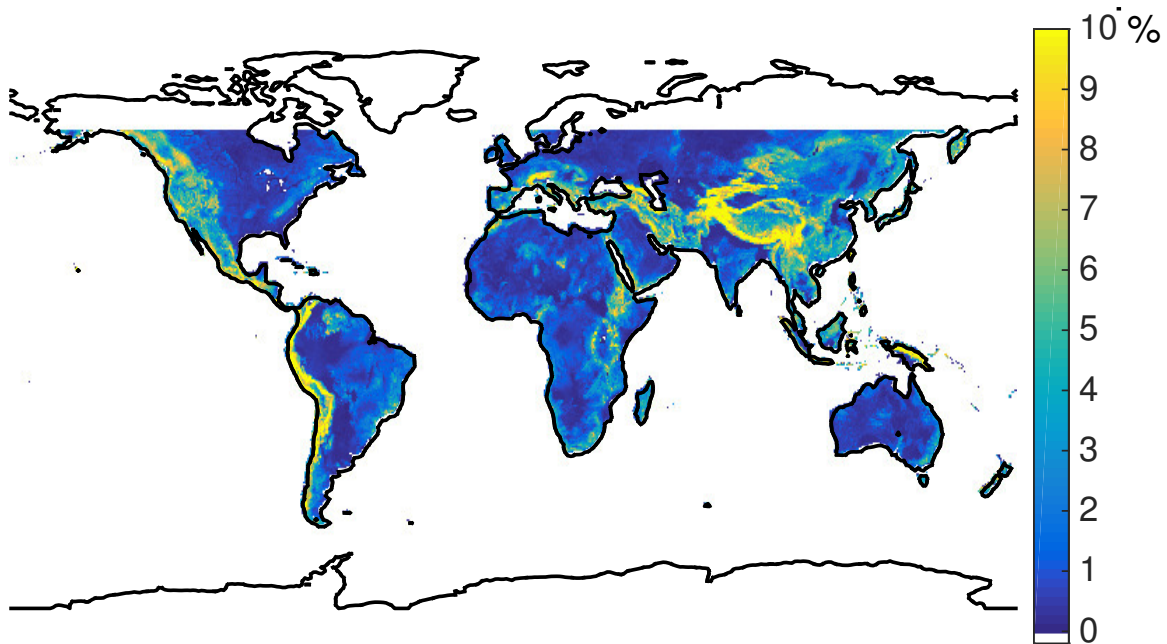


Figure 5.3: Large scale solar arrays require a slope less than 3% for optimal siting. This map shows the approximate minimum slope globally as computed from the SRTM data set [181]. Data were not available for Antarctica or latitudes north of 60°N.

### 5.3.3 Population Density

Photovoltaics could potentially be located on rooftops in regions with a high population density [39]. However, noise and safety requirements make such locations problematic for below-ground compressed air energy storage [167]. Use of batteries or transmission lines could relax this requirement, however would require additional siting analysis. Population density data from the Socio-economic Data and Applications Center was used to exclude pixels with a population density  $> 500$  people/ $km^2$ , Fig. 5.4. The data was collected for sub-national administrative units and computed as the total population divided by the land area [184].

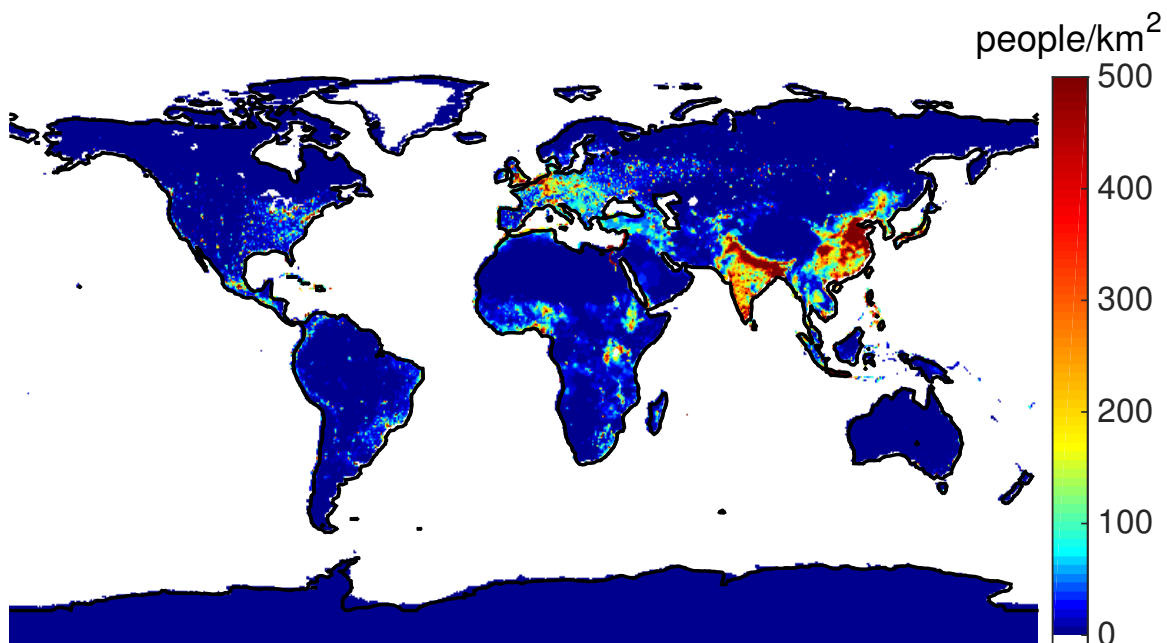


Figure 5.4: The global population density per  $0.5^\circ \times 0.5^\circ$  pixel is shown, computed as the total population divided by the land area of a unit [184].

### 5.3.4 Wetland Areas and Flood Plains

Wetland areas, including marshland, lakes, rivers, swamps and flood plains, are not suitable for building the facilities required for this coupled system. I utilized the

Global Lakes and Wetlands Database provided by the World Wildlife Foundation [182, 183] for this analysis. These data have a resolution of 30 arc second x 30 arc second and provide 12 categories of wetland types. In order to aggregate these data into  $0.5^\circ \times 0.5^\circ$  pixels for the current analysis, I assumed that any pixel was suitable for building a coupled system of photovoltaics and compressed air energy storage if less than half of its total area was wetland area. Figure 5.5 shows the aggregated map of all wetland types. The wetland type shown was determined by the most common wetland type in each pixel.

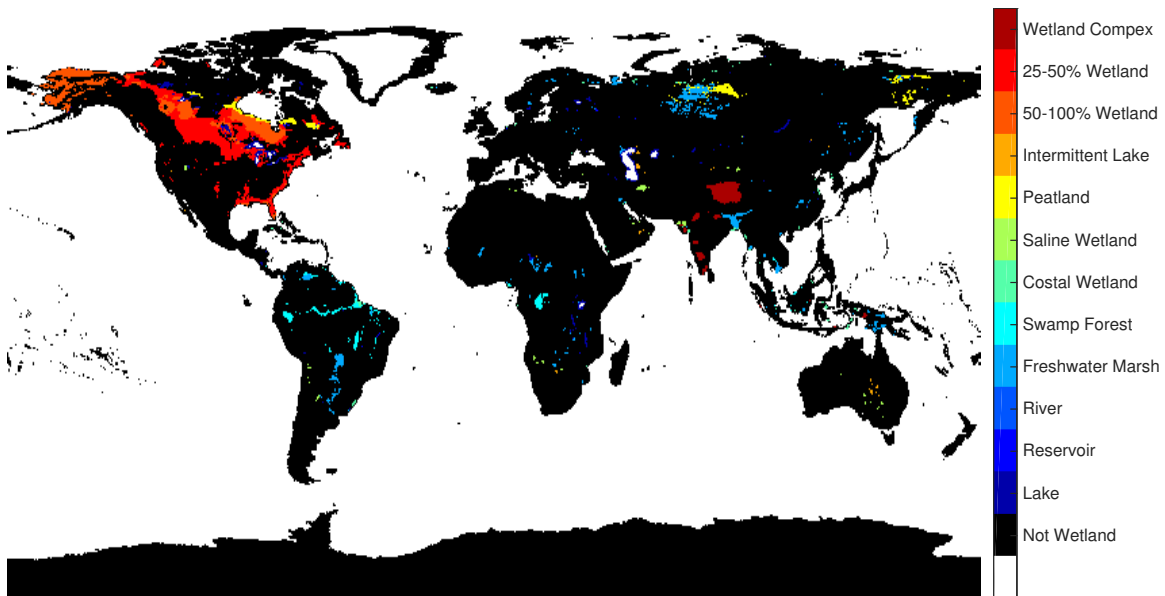


Figure 5.5: Global wetlands extent. This map shows all pixels with a majority wetland area, by wetland type. These areas would not be suitable for siting a PV-CAES facility.

### 5.3.5 Population

The electricity provided by a coupled system of photovoltaics and compressed air energy storage is assumed to be directly utilized within each  $0.5^\circ \times 0.5^\circ$  region. This ensures that the electricity produced is accessible to the local population even in the absence of a stable distribution grid. Given this assumption, locations with higher

populations are able to provide electricity to a larger number of people. I assume a higher social benefit is obtained if a greater number of people are given access to low-carbon electricity, scaled according to the population of each pixel. Population data were used for the year 2000 for the local population within each  $0.5^\circ \times 0.5^\circ$  area, Figure 5.6, also from the SEDAC database [185].

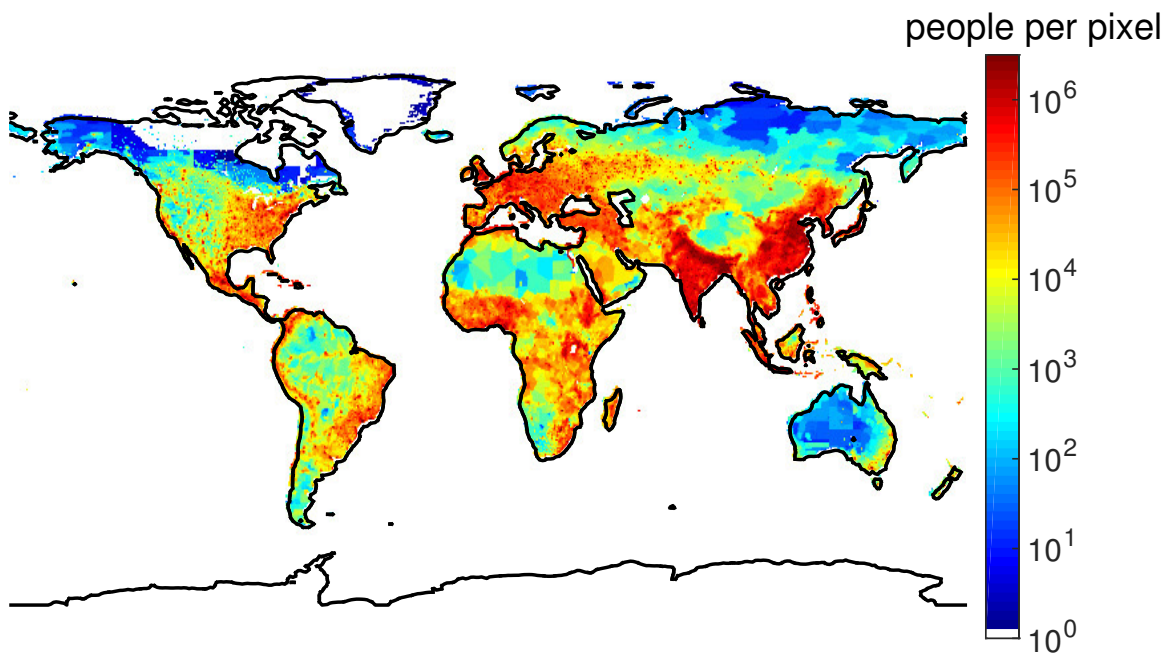


Figure 5.6: The global population is shown here on a  $\log_{10}$  scale [185].

### 5.3.6 Growth in Electricity Consumption

Providing low-carbon energy to regions with a high-expected growth in electricity consumption will have a higher social benefit than to locations with low expected growth, particularly as those locations with high growth are expected to require additional electricity generation to be installed. If such installations were provided by renewable sources such as solar power, a large amount of carbon emissions could be avoided. This metric was used in the first analysis performed, identifying locations

with growing need as ideal for solar power facilities.

The growth rate in electricity consumption was computed for each country using the Electric Power Consumption data set [186], the Population Total data set [187] and the Population Estimates and Projections data set [188]. Countries were converted to pixels using the country boundaries defined in the Socio-economic Data and Applications Center data-base [191]. In order to compute the growth in electricity consumption, the per capita electric power consumption was multiplied by population to approximate the total electricity consumed by country in a particular year. The per capita electric power consumption data from 2007 through 2012 was used to project the electric power consumption per capita in 2020 using linear regression. This was multiplied by the World Bank expected population in 2020 to estimate the total electricity consumption in 2020. The expected increase in consumption was computed as the percent increase in electricity use from 2012 to 2020, shown in Figure 5.7.

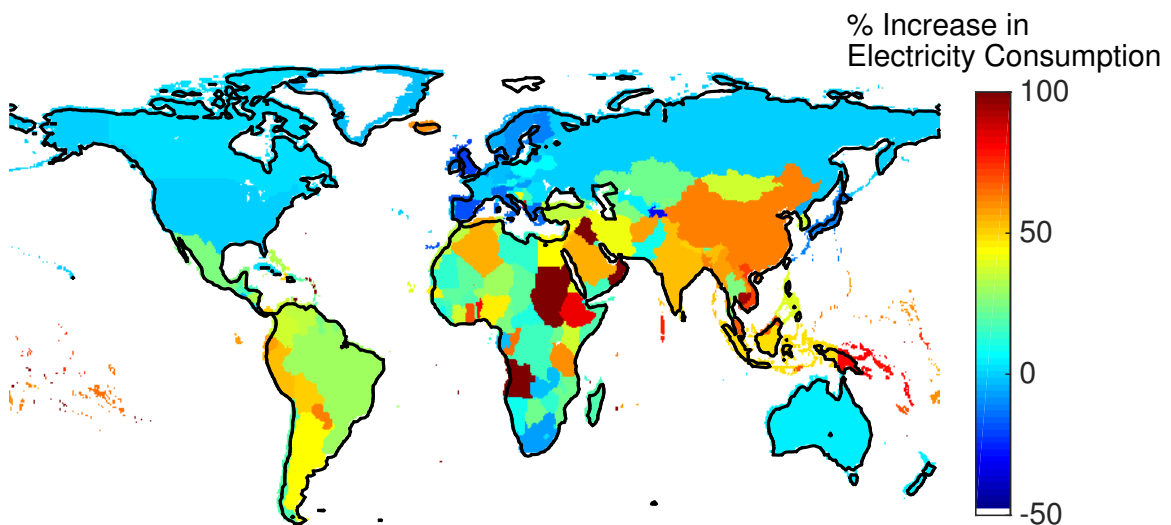


Figure 5.7: The expected percent increase in electricity consumption between 2012 and 2020 was determined by projecting the electricity use per capita growth rate using country level data from 2007-2012 and the World Bank estimated population in 2020 [186–188].

### 5.3.7 Access to Electricity

Access to electricity is a marker for economic development and it varies considerably in the developing world. As living standards in these regions rise, so will consumption of electricity. The lower the access level in a particular region, the higher the social benefit of providing future capacity through low-carbon generation sources. Data on country-wide access to electricity were used from the World Bank [189], shown in Fig. 5.8. These data were also converted to pixels based on the Socio-economic Data and Applications Center database country boundaries [191].

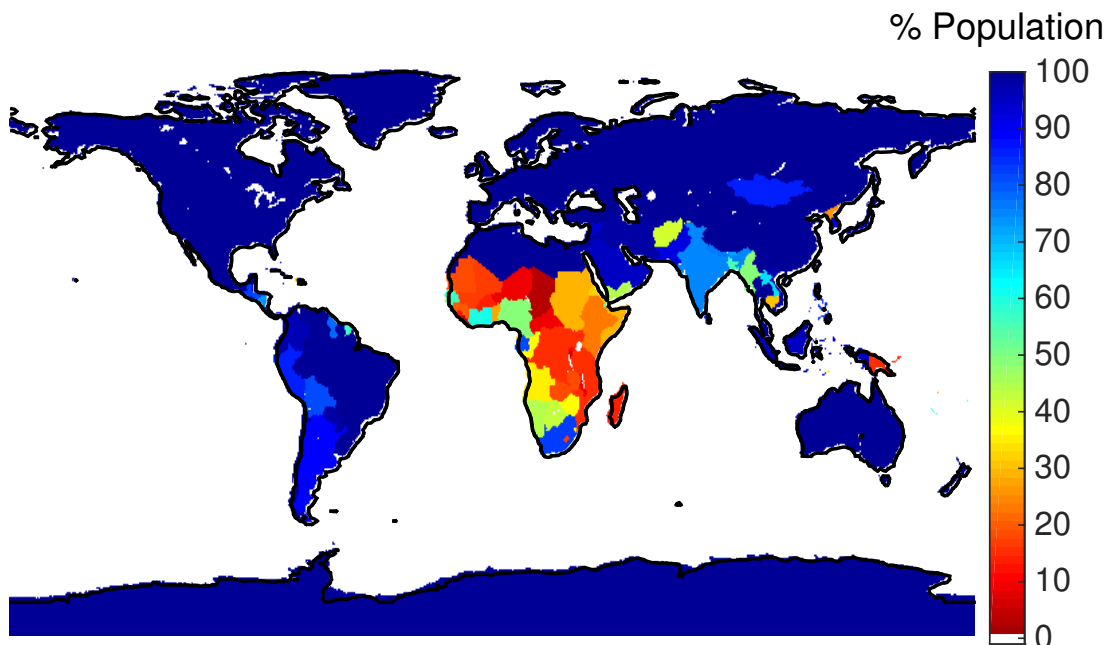


Figure 5.8: Percentage of the population with access to electricity, by country.

This metric was used in a second analysis, with need for electricity determined by current lack of access. The available country-level data is coarse for this metric, and so is unable to identify local needs. However, countries with the lowest overall connectivity could benefit the most from additional energy production, and in many instances data is not available on the extent of local grid connectivity across the world.

### 5.3.8 Cost of Electricity

The economic feasibility of coupled systems of photovoltaics and grid-scale energy storage was determined by the levelized cost of electricity for these systems, Fig. 5.9. The systems utilized were sized to provide 100MWe output with a capacity factor equivalent to that of the U.S. nuclear fleet, as was previously computed at  $0.5^\circ \times 0.5^\circ$  resolution in Section 3.2. Economically, locations with lower cost have a higher benefit than more costly locations.

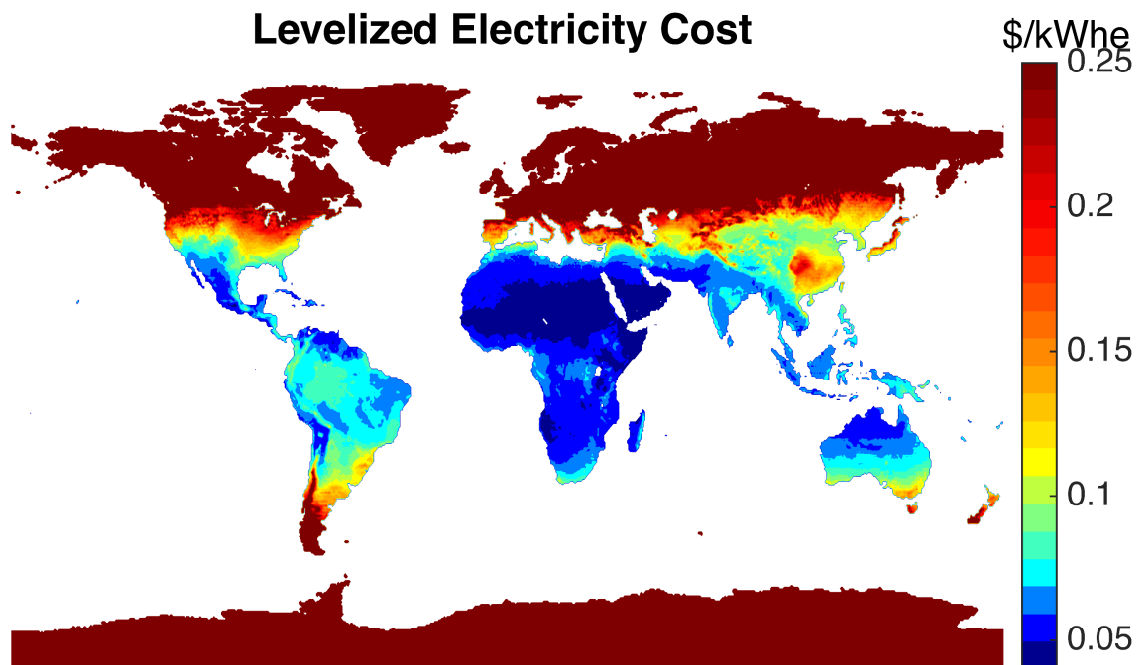


Figure 5.9: Levelized cost of baseload electricity from the coupled systems. The life-cycle energy cost for a coupled photovoltaic array and compressed air energy storage facility, as computed in Section 3.2.

Many locations north of the arctic circle were unable to provide year-round energy, and as such had unrealistically high energy costs. I therefore introduced a cap on the cost of 1  $\$/kWh_e$ , such that all locations with a cost greater than or equal to this value were given a score of 1.



## 5.4 Multi-Criteria Decision Analysis

The exclusion criteria were combined to identify all locations at which a coupled photovoltaic and compressed air energy storage facility would not be feasible to site. Figure 5.10 shows the number of criteria,  $N_{exclusion}$ , for which each location is excluded. The locations with one or more exclusions will be colored black in subsequent figures.

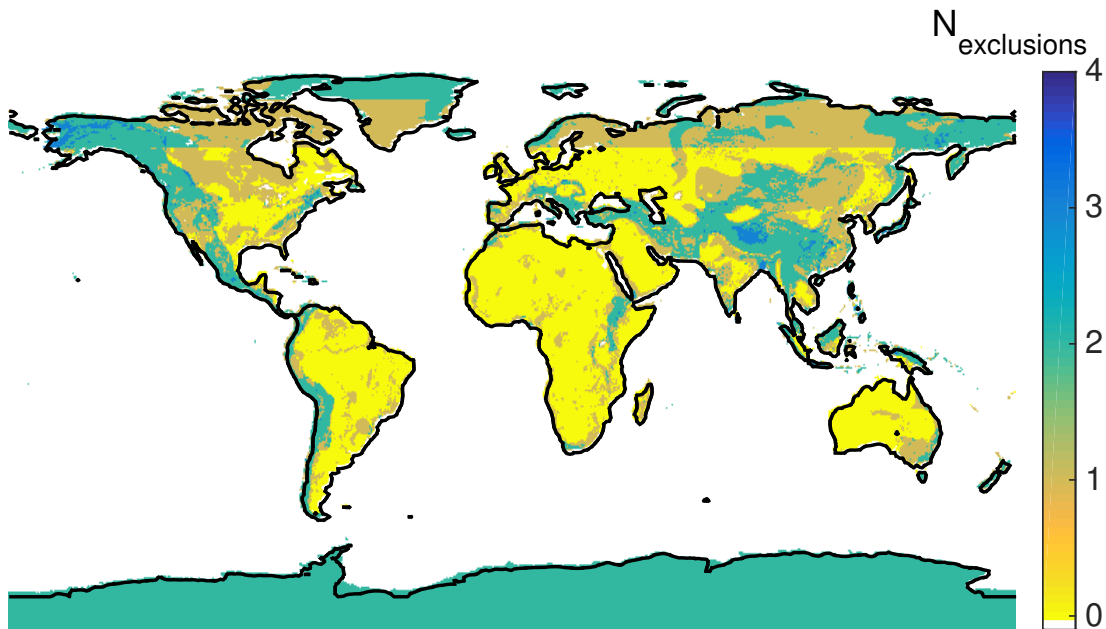


Figure 5.10: Number of exclusion criteria for each pixel. The straight line at latitude 60°N is due to a lack of data for land slope, and so these pixels were all excluded.

The granularity of the data utilized to identify excluded regions could potentially lead to imprecise results. Particularly for exclusion via slope and wetland area, I have used an aggregate measure for the entire pixel, which is approximately 30 km x 30 km in size. Within these pixels, favorable conditions could exist for these facilities that the granular data is unable to show. In addition, all locations with favorable geology for compressed air energy storage facilities would require a site-specific analysis to confirm such a facility could be sited there.

After aggregating all of the data and identifying excluded regions, I determined

the highest and lowest scores in total for each of the two social benefit analyses. Locations with lower scores are more ideal and locations with higher scores would be particularly non-ideal locations.

The first analysis included population, cost, and expected growth in electricity usage. The location with the lowest score was located near Ho Chi Minh City in Vietnam, with a score of 0.91. The location with the highest score was located in northern Scotland, with a score of 2.6. Figure 5.11 shows score,  $X$ , from Eq. (5.3) for each location on the planet for the first analysis.

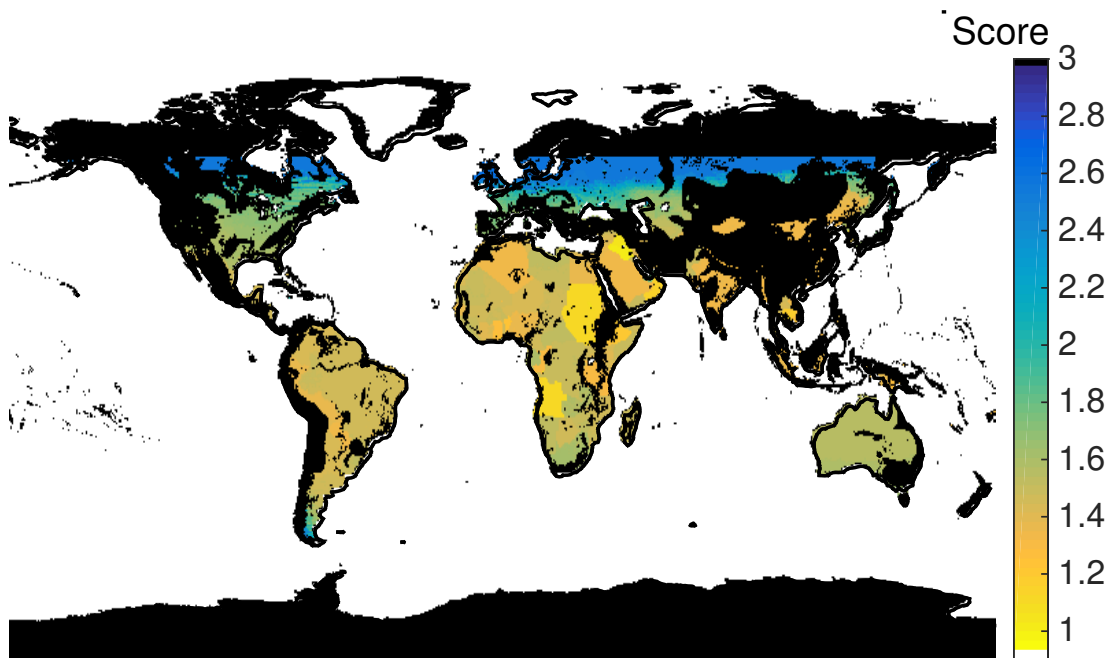


Figure 5.11: Score  $X$ , determined by criteria of population, cost, and expected growth in electricity usage, used to identify locations with optimal combinations of all variables. Lower values indicate more ideal locations. Locations with one or more exclusions are colored black.

While the lowest score is in Vietnam, locations in Iraq and much of Africa also have low scores, in addition to other locations in southeast Asia. These regions have high expected increase in electricity consumption, low costs for the coupled facilities, and high populations, respectively.

I next analyzed locations that would be ideal for populations that currently have little access to electricity. This analysis included population, cost, and the percent of a country's population with access to electricity. A strong benefit of a coupled system of photovoltaics and grid-scale energy storage is its ability to provide stand-alone base-load electricity. Populations with no current access to the grid could gain a large benefit, both in terms of education and quality of life, from increased access to electricity. As such, these populations would have a strong benefit from the proposed solar power facility.

Figure 5.12 shows the score,  $X$ , from Eq. (5.3) based on population, electricity access, and cost. The lowest score, 1.0, was found to be at the northeastern border of Burundi, a country where only 5.3% of the population has access to electricity. As a

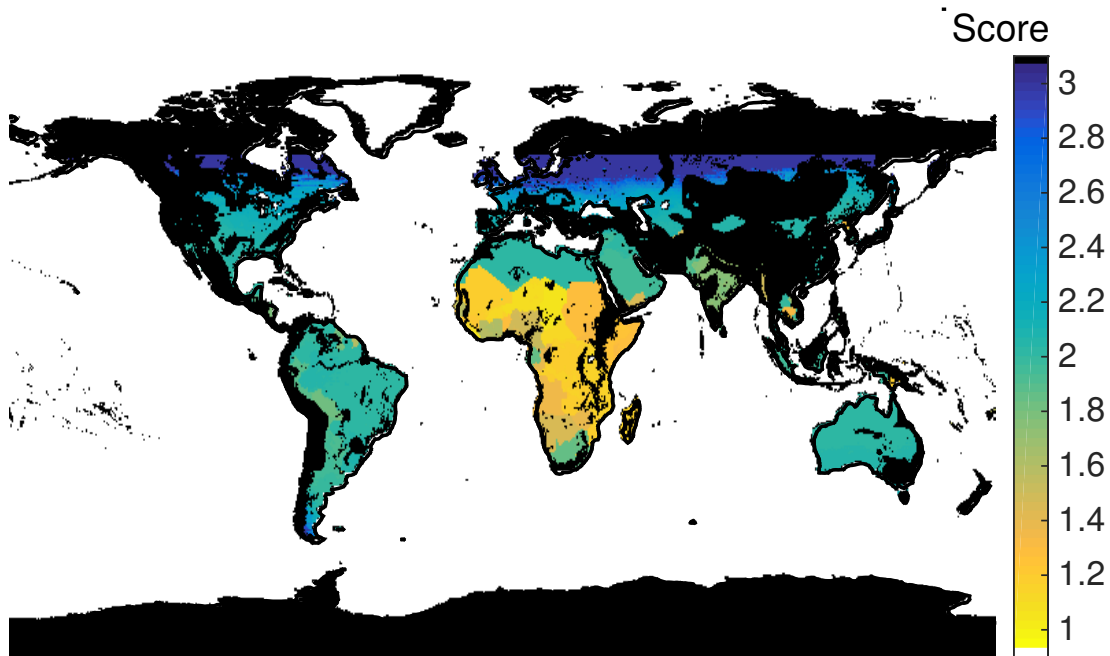


Figure 5.12: The criteria described in Section 5.3 were used to compute a score  $X$  when including electricity access to identify locations with a high need for stand-alone electricity. This map shows the value of  $X$  for each location across the globe. Locations with one or more exclusions are colored black.

whole, Africa had very low scores for this metric due to very low electricity access and also low electricity costs. The highest score, 3, was seen in many northern locations which all have access to electricity and high electricity costs from these facilities.

It should be noted that there are likely many rural areas overlooked in this analysis due to the granularity of the data source. The global electricity access data I used is only available at a country level. In many countries, particularly Africa and India, the rural populations have much lower electricity access than large cities do. Averaging this throughout a country will lead to skewed results, particularly when coupled with the population metric, which has a lower score for cities with high population. Future work could look locally at specific countries, such as India, where grid connectivity varies widely between urban and rural areas. Such granular data is not available globally, however could potentially be found for specific regions of interest.

## Chapter 6

### Conclusions

#### 6.1 Conclusions from Irradiance Calculations

I have created a 25-year data set of solar irradiance values with 1-hour temporal resolution and  $0.5^\circ \times 0.5^\circ$  angular resolution utilizing the ISCCP satellite-based data set. This data set was vetted against four separate data sets of ground-based irradiance measurements. The mean error was found to be less than 14% in all non-polar locations, and correlations of 24-hour average irradiance values between the calculated and measured irradiance were greater than 0.69, with the majority of locations having a correlation greater than 0.9. This was determined to be an acceptable error for a rapidly changing, localized resource such as solar irradiance.

I attempted to improve the correlation of the computed irradiance to more closely match the ground-based measurements by including several correction factors. First, I utilized the wavelength used to calibrate the ISCCP instruments when computing the transmission values. Second, I computed a wavelength-averaged irradiance by integrating irradiance values computed for 35 wavelengths in the solar spectrum over the solar spectrum. Third, I incorporated visibility measurements from the NCDC data base at all locations for which they were available. None of these corrections were found to significantly improve the correlation of computed irradiance values to ground-based data.

I believe that the lack of improvement of this data set is due to the spatial resolution of the satellite data. The satellites view a particular solid angle of the

earth's surface, which may or may not correspond to the ground-based location at which the irradiance values were measured. Differences in local weather phenomena are assumed to have a greater effect on the differences in the computed and measured data points than the correction factors examined in this analysis.

## 6.2 Conclusions from PV-CAES Model

I created an energy flow model for a coupled photovoltaic-compressed air energy storage (PV-CAES) system and calculated the life-cycle costs from utilizing this system as a base-load resource. I determined that given the recent drop in cost of photovoltaic modules, such a system would be able to provide energy at a life-cycle cost less than 0.08  $$/kWh_e$  for 42.0% of the global land area, and for 46.2% of the world's population.

I also utilized the same model to determine the cost of a system utilizing above-ground CAES storage or battery storage for locations in which traditional CAES would not be technically feasible. These systems are more expensive than traditional CAES, and so while technically feasible are less economically advantageous than the PV-CAES system. Battery systems in particular are not able to provide low-cost energy from a coupled PV-battery system until PV modules reach  $\$1/W_p$ , and do not become widely site-able until battery costs drop to the DOE goal of  $\$150/kWh_e$ .

Additionally, in all locations some amount of excess energy was produced in the analysis of a coupled PV-CAES facility. This energy could be sold to the electric grid on the real-time market to provide additional revenue for the PV-CAES facility. I computed average hourly real-time prices by month for the U.S. independent system operators and determined the total revenue that could be expected for two average price curves. The total revenue was as high as \$10 billion for northern locations with

large arrays. In most locations the revenue was less than \$2 billion. This could be used to offset the costs of the system.

### **6.3 Conclusions from Load Following Model**

I determined the effect of utilizing a coupled photovoltaic and compressed air energy storage system to provide load-following and on-peak energy production instead of base-load energy. Solar irradiance patterns are similar to load requirements, particularly in locations with summer-peaking load. For each of four load profiles I computed the cost of energy for eight separate storage capacities and identified the storage capacity which provided the lowest cost energy. I found that on-peak energy generation operating between 6 am and 10 pm required the least storage capacity, followed by a summer-peaking load such as the average load of ERCOT. I also determined that at higher storage capacities, base-load generation was actually cheaper than load following for some locations. In addition, utilizing these load profiles reduced carbon emissions from the CAES facility up to 17% for ERCOT and PJM average load profiles and up to 30% for on-peak generation.

### **6.4 Conclusions from GIS Analysis**

I utilized the multi-criteria decision analysis framework to identify locations that provide an optimal combination of low cost, high population, and either high growth in electricity usage or low grid connectivity along with siting limitations. These variables together indicate a strong need for low-cost dispatchable renewable energy sources, as measured by a growing need for electricity or a current lack of electricity. I presented global maps showing the optimal locations, which tended to be in Africa, the Middle East as well as Southeast Asia. These locations all represent growing areas

with low expected electricity costs from the proposed PV-CAES facility, and would be ideal for solar power facilities.

## 6.5 Suggestions for future work

This analysis could be extended by examining in more detail how the proposed coupled PV-CAES facility would interact with a traditional electric grid. Such a system could be operated in different manners depending on the particular capacity mix and load curve for specific locations. Such an analysis could potentially change the sizing of either array or storage facility for optimal operation, given the ability of other energy sources to provide electricity during the night or cloudy days.

Ideal site placement of these systems could be improved by incorporating additional metrics in the multi-criteria decision analysis, particularly finer resolution data. More detailed data concerning expected population growth and electricity access would allow for a more in-depth, localized analysis. In addition, other land-based limitations such as current land-use patterns and land-quality could be identified and incorporated, and the use of above-ground CAES or battery storage facilities could be investigated, eliminating one of the current geographical exclusion criteria.

Additionally, it should be noted that countries with the largest amount of installed capacities do not correspond with those locations identified in Chapter 5 as ideal for solar power. Locations with high installed capacities of photovoltaics tend to instead be locations with strongly beneficial policies for solar energy technologies. While many papers have been published analyzing the impact of these policies, these are typically focused on specific regions and on the traditional use of solar power as a non-dispatchable resource. It could be of interest to examine ideal policies that would encourage growth of dispatchable solar power systems as described in Chapter 3.



## Bibliography

- [1] J. Conti, “International energy outlook 2013,” tech. rep., EIA, 2013.
- [2] IPCC, “Climate change 2007: Synthesis report. contribution of working groups I, II, and III to the fourth assessment report of the intergovernmental panel on climate change,” tech. rep., United Nations, 2007.
- [3] K. H. Solangi, M. R. Islam, R. Saidur, N. A. Rahim, and H. Fayaz, “A review on global solar energy policy,” *Renewable and Sustainable Energy Reviews*, vol. 15, p. 21492163, 2011.
- [4] IEA, “Key world energy statistics 2014,” tech. rep., International Energy Agency, 2014.
- [5] IPCC, “Climate change 2014: Mitigation of climate change. working group III contribution to the ipcc 5th assessment report - final drafts,” Tech. Rep. IPCC WGIII AR5, United Nations, 2014.
- [6] M. I. Hoffert, K. Caldeira, G. Benford, D. R. Criswell, C. Green, H. Herzog, A. K. Jain, H. S. Kheshgi, K. S. Lackner, J. S. Lewis, H. D. Lightfoot, W. Manheimer, J. C. Mankins, M. E. Mauel, L. J. Perkins, M. E. Schlesinger, T. Volk, and T. M. L. Wigley, “Advanced technology paths to global climate stability: Energy for a greenhouse planet,” *Science*, vol. 298, no. 5595, pp. 981–987, 2002.
- [7] M. Z. Jacobson, “Review of solutions to global warming, air pollution, and energy security,” *Energy & Environmental Science*, vol. 2, pp. 148–173, 2009.

- [8] D. D. Hsu, P. O'Donoghue, V. Fthenakis, G. A. Heath, H. C. Kim, P. Sawyer, J. K. Choi, and D. E. Turney, "Life cycle greenhouse gas emissions of crystalline silicon photovoltaic electricity generation," *Journal of Industrial Ecology*, vol. 16, pp. 122–135, 2012.
- [9] D. Weisser, "A guide to life-cycle greenhouse gas (ghg) emissions from electric supply technologies," *Energy*, vol. 32, pp. 1543–1559, 2007.
- [10] J. Deutch, C. Forsberg, A. Kadak, M. Kazimi, E. Moniz, and J. Parsons, "Update of the mit 2003 future of nuclear power," tech. rep., MIT, 2009.
- [11] J. R. Lamarsh and A. J. Baratta, *Introduction to Nuclear Engineering*. USA: Prentice Hall, third ed., 2001.
- [12] S. Chu and A. Majumdar, "Opportunities and challenges for a sustainable energy future," *Nature*, vol. 488, pp. 294–303, 2012.
- [13] N. Lewis, "Toward cost-effective solar energy use," *Science*, vol. 315, pp. 798–801, 2007.
- [14] R. Ruther, P. Knob, C. Jardim, and S. Rebechi, "Potential of building integrated photovoltaic solar energy generators in assisting daytime peaking feeders in urban areas in Brazil," *Energy Conversion and Management*, vol. 49, pp. 1074–1079, 2008.
- [15] G. Masson, M. Latour, M. Reking, I. T. Theologitis, and M. Papoutsis, "Global market outlook for photovoltaics 2013-2017," tech. rep., European Photovoltaic Industry Association, 2013.
- [16] "California solar initiative," 2013.

- [17] V. Lauber and L. Mez, “Renewable electricity policy in Germany, 1974 to 2005,” *Bulletin of Science Technology and Society*, vol. 26, no. 2, pp. 105–120, 2006.
- [18] REN21, “Renewables 2014 global status report,” tech. rep., Paris: REN21 Secretariat, 2014.
- [19] N. Ayoub and Y. Naka, “Governmental intervention approaches to promote renewable energies - special emphasis on japanese feed-in tariff,” *Energy Policy*, vol. 43, pp. 191–201, 2012.
- [20] R. Wiser, G. Barbose, and E. Holt, “Supporting solar power in renewables portfolio standards: Experience from the united states,” *Energy Policy*, vol. 39, pp. 3894–3905, 2011.
- [21] S. Avril, C. Mansilla, M. Busson, and T. Lemaire, “Photovoltaic energy policy: Financial estimation and performance comparison of the public support in five representative countries,” *Energy Policy*, vol. 51, pp. 244–258, 2012.
- [22] U.S. DOE, “Sunshot vision study,” tech. rep., U.S. Department of Energy, 2012.
- [23] NEDO, “Overview of ”PV roadmap toward 2030”,” tech. rep., New Energy and Industry Technology Development Organization, 2004.
- [24] IEA, “Global renewable energy: Iea/irena joint policies and measures database,” September 26, 2012 2012.
- [25] European Commission, “Europe 2020 targets,” 2011.
- [26] G. E. Azuela and L. A. Barroso, “Design and performance of policy instruments to promote the development of renewable energy: Emerging experience in selected developing countries,” tech. rep., World Bank, 2012.

- [27] J. Ondraczek, “Are we there yet? Improving solar PV economics and power planning in developing countries: The case of Kenya,” *Renewable and Sustainable Energy Reviews*, vol. 30, pp. 604–615, 2014.
- [28] S. Kann, M. Shiao, S. Mehta, C. Honeyman, N. Litvak, J. Jones, B. J., W. Lent, and S. Rumery, “U.S. solar market insight report: 2013 year-in-review, executive summary,” tech. rep., SEIA, 2014.
- [29] G. Nemet, “Beyond the learning curve: factors influencing cost reductions in photovoltaics,” *Energy Policy*, vol. 34, pp. 3218–3232, 2006.
- [30] Bloomberg Finance, L.P., “Sustainable energy in america 2014 factbook,” tech. rep., Business Council for Sustainable Energy, 2014.
- [31] M. A. Eltawil and Z. Zhao, “Grid-connected photovoltaic power systems: Technical and potential problemsa review,” *Renewable and Sustainable Energy Reviews*, vol. 14, pp. 112–129, 2010.
- [32] O. Alsayegh, S. Alhajraf, and H. Albusairi, “Grid-connected renewable energy source systems: Challenges and proposed management schemes,” *Energy Conversion and Management*, vol. 51, pp. 1690–1693, 2010.
- [33] J. A. Pecas Lopes, N. Hatziargyriou, J. Mutale, P. Djapic, and N. Jenkins, “Integrating distributed generation into electric power systems: A review of drivers, challenges and opportunities,” *Electric Power Systems Research*, vol. 77, pp. 1189–1203, 2007.
- [34] P. Denholm and M. Hand, “Grid flexibility and storage required to achieve very high penetration of variable renewable electricity,” *Energy Policy*, vol. 39, pp. 1817–1830, 2011.

- [35] L. Xie, P. M. S. Carvalho, L. A. F. M. Ferreira, J. Liu, B. H. Krogh, N. Popli, and M. D. Ilic, “Wind integration in power systems: Operational challenges and possible solutions,” *Proceedings of the IEEE*, vol. 99, pp. 214–232, 2011.
- [36] E3, “Investigating a higher renewables portfolio standard in california,” tech. rep., Energy and Environmental Economics, Inc., 2014.
- [37] D. Lew, G. Brinkman, E. Ibanez, A. Florita, M. Heaney, B. M. Hodge, M. Hummon, and G. Stark, “Western wind and solar integration study phase 2,” Tech. Rep. NREL/TP-5500-55588., NREL, 2013.
- [38] H. Chen, T. N. Cong, W. Yang, C. Tan, Y. Li, and Y. Ding, “Progress in electrical energy storage system: A critical review,” *Progress in Natural Science*, vol. 19, pp. 291–312, 2009.
- [39] B. L. Stoll, T. A. Smith, and M. R. Deinert, “Potential for rooftop photovoltaics in Tokyo to replace nuclear capacity,” *Environmental Research Letters*, vol. 8, p. 014042, 2013.
- [40] R. M. Dell and D. A. J. Rand, “Energy storage - a key technology for global energy sustainability,” *Journal of Power Sources*, vol. 100, pp. 2–17, 2001.
- [41] H. Ibrahim, A. Ilinca, and J. Perron, “Energy storage systems - characteristics and comparisons,” *Renewable and Sustainable Energy Reviews*, vol. 12, pp. 1221–1250, 2008.
- [42] B. L. Stoll, A. Osborne, and M. Deinert, “Photovoltaics and grid-scale energy storage can provide baseload electricity competitively in many regions,” In Review.

- [43] J. Deane, B. P. Gallachir, and E. J. McKeogh, “Techno-economic review of existing and new pumped hydro energy storage plant,” *Renewable and Sustainable Energy Reviews*, vol. 14, pp. 1293–1302, 2010.
- [44] P. Denholm and G. Kulcinski, “Life cycle energy requirements and greenhouse gas emissions from large scale energy storage systems,” *Energy Conversion and Management*, vol. 45, pp. 2153–2172, 2004.
- [45] B. Dunn, H. Kamath, and J. Tarascon, “Electrical energy storage for the grid: a battery of choices,” *Science*, vol. 334, pp. 928–935, 2011.
- [46] Y. Hou, R. Vidu, and P. Stroeve, “Solar energy storage methods,” *Industrial & Engineering Chemistry Research*, vol. 50, pp. 8954–8964, 2011.
- [47] J. Mason, V. Fthenakis, K. Zweibel, T. Hansen, and T. Nikolakakis, “Coupling PV and CAES power plants to transform intermittent PV electricity into a dispatchable electricity source,” *Progress in Photovoltaics: Research and Application*, vol. 16, pp. 649–668, 2008.
- [48] I. P. Gyuk, “EPRI-DOE handbook of energy storage for transmission & distribution applications,” tech. rep., U.S. Department of Energy, 2003.
- [49] S. Succar and R. H. Williams, “Compressed air energy storage: Theory, resources and applications for wind power,” tech. rep., Princeton University, 2008.
- [50] Z. Yang, J. Zhang, M. C. Kintner-Meyer, X. Lu, D. Choi, J. P. Lemmon, and J. Liu, “Electrochemical energy storage for green grid,” *Chemical Reviews*, vol. 111, no. 5, pp. 3577–3613, 2011.
- [51] W. B. Rossow, A. W. Walker, D. E. Beuschel, and M. D. Roiter, “International satellite cloud climatology project documentation of new cloud datasets,” tech.

- rep., International Council of Scientific Unions and the World Meteorological Organization, 1996.
- [52] W. B. Rossow, “International satellite cloud climatology project dx dataset,” 2013.
- [53] W. B. Rossow, “International satellite cloud climatology project d1 dataset,” 2013.
- [54] J. K. B. Bishop, W. B. Rossow, and E. G. Dutton, “Surface solar irradiance from the international satellite cloud climatology project 1983-1991,” *Journal of Geophysical Research*, vol. 102, no. D6, pp. 6883–6910, 1997.
- [55] R. Frouin, D. W. Lingner, and C. Gautier, “A simple analytical formula to compute clear sky total and photosynthetically available solar irradiance at the ocean surface,” *Journal of Geophysical Research*, vol. 94, no. C7, pp. 9731–9742, 1989.
- [56] S. Chu, “Carbon capture and sequestration,” *Science*, vol. 325, p. 1599, 2009.
- [57] R. S. Haszeldine, “Carbon capture and storage: How green can black be?,” *Science*, vol. 325, pp. 1647–1652, 2009.
- [58] J. Pires, F. G. Martins, M. C. M. Alvim-Ferraz, and M. Simoes, “Recent developments on carbon capture and storage: An overview,” *Chemical engineering research and design*, vol. 89, pp. 1446–1460, 2011.
- [59] T. Grau, M. Huo, and K. Neuhoff, “Survey of photovoltaic industry and policy in Germany and China,” *Energy Policy*, vol. 51, pp. 20–37, 2012.

- [60] Y. Yamamoto, “Pricing electricity from residential photovoltaic systems: A comparison of feed-in tariffs, net metering, and net purchase and sale,” *Solar Energy*, vol. 86, pp. 2678–2685, 2012.
- [61] G. R. Timilsina, L. Kurdgelashvili, and P. A. Narbel, “Solar energy: Markets, economics and policies,” *Renewable and Sustainable Energy Reviews*, vol. 16, pp. 449–465, 2012.
- [62] A. Macintosh and D. Wilkinson, “Searching for public benefits in solar subsidies: A case study on the Australian governments residential photovoltaic rebate program,” *Energy Policy*, vol. 39, pp. 3199–3209, 2011.
- [63] T. Coutour and Y. Gagnon, “An analysis of feed-in tariff remuneration models: Implications for renewable energy investment,” *Energy Policy*, vol. 38, pp. 955–965, 2010.
- [64] J. A. Lesser and S. X., “Design of an economically efficient feed-in tariff structure for renewable energy development,” *Energy Policy*, vol. 36, 2008.
- [65] D. Fouquet and T. B. Johansson, “European renewable energy policy at cross-roads: Focus on electricity support mechanisms,” *Energy Policy*, vol. 36, pp. 4079–4092, 2008.
- [66] N. R. Darghouth, G. Barbose, and R. Wiser, “The impact of rate design and net metering on the bill savings from distributed PV for residential customers in california,” *Energy Policy*, vol. 39, p. 52435253, 2011.
- [67] D. of State Incentives for Renewable Energy, “Solar summary maps.” <http://www.dsireusa.org/summarymaps/index.cfm?ee=1&RE=1>. U.S. DOE.



- [68] L. Dusonchet and E. Telaretti, “Economic analysis of different supporting policies for the production of electrical energy by solar photovoltaics in western European Union countries,” *Energy Policy*, vol. 38, pp. 3297–3308, 2010.
- [69] Y. Zhang, J. Song, and S. Hamori, “Impact of subsidy policies on diffusion of photovoltaic power generation,” *Energy Policy*, vol. 39, pp. 1958–1964, 2011.
- [70] SEIA, “State solar policy: California solar.” <http://www.seia.org/state-solar-policy/california>. Accessed: Feb 24, 2015.
- [71] CSI, “Program totals by administrator.” [http://www.californiasolarstatistics.ca.gov/reports/agency\\_stats/](http://www.californiasolarstatistics.ca.gov/reports/agency_stats/). Accessed: Feb 24, 2015.
- [72] D. M. Hart, “Making, breaking, and (partially) remaking markets: State regulation and photovoltaic electricity in new jersey,” *Energy Policy*, vol. 38, pp. 6662–6673, 2010.
- [73] E. Martinot, A. Chaurey, D. Lew, J. R. Moreira, and N. Wamukonya, “Renewable energy markets in developing countries,” *Annual Review of Energy and the Environment*, vol. 27, pp. 309–48, 2002.
- [74] J. Cochran, T. Mai, and M. Bazilian, “Meta-analysis of high penetration renewable energy scenarios,” *Renewable and Sustainable Energy Reviews*, vol. 29, pp. 246–253, 2014.
- [75] Transpower stromubertragungs gmbh, “European wind integration study,” Tech. Rep. TREN/07/FP6EN/S07.70123/038509, 2010. Ed. Wilhelm Winter.
- [76] EnerNex Corporation, “Eastern wind integration and transmission study,” Tech. Rep. NREL Report No. SR-550-47078, NREL, 2010.

- [77] GE Energy, “Western wind and solar integration study,” tech. rep., NREL, 2010.
- [78] Eastern Interconnection Planning Collaborative, “Phase 2 report: Interregional transmission development and analysis for three stakeholder scenarios,” Tech. Rep. DOE Award Project: DE-OE0000343, EIPC, 2012.
- [79] S. Lu, N. Samaan, D. Meng, F. Chassin, Y. Zhang, B. Vyakaranam, M. Warwick, J. Fuller, R. Diao, T. Nguyen, and C. Jin, “Duke Energy photovoltaic integration study: Carolinas service areas,” Tech. Rep. PNNL-23226, PNNL, 2014.
- [80] GE Energy, “PJM renewable integration study,” tech. rep., GE Energy, 2013.
- [81] MISO and M. Hydro, “Manitoba Hydro wind synergy study,” tech. rep., 2013.
- [82] J. M. Morales, A. J. Conejo, and J. Perez-Ruiz, “Economic valuation of reserves in power systems with high penetration of wind power,” in *Power Systems, IEEE Transactions on (Volume:24 , Issue: 2)*, pp. 900–910, 14 April 2009.
- [83] A. Borghetti, M. Bosetti, S. Grillo, S. Massucco, C. A. Nucci, M. Paolone, and F. Silvestro, “Short-term scheduling and control of active distribution systems with high penetration of renewable resources,” *Systems Journal, IEEE*, vol. 4, pp. 313–322, 2010.
- [84] D. M. Powell, M. T. Winkler, H. J. Choi, C. B. Simmons, D. B. Needleman, and T. Buonassisi, “Crystalline silicon photovoltaics: a cost analysis framework for determining technology pathways to reach baseload electricity costs,” *Energy and Environmental Science*, vol. 5, pp. 5874–5883, 2012.
- [85] T. Saga, “Advances in crystalline silicon solar cell technology for industrial mass production,” *Asia Materials*, vol. 2, pp. 96–102, 2010.

- [86] M. A. Green, “Thin-film solar cells: review of materials, technologies and commercial status,” *Journal of Materials Science: Materials in Electronics*, vol. 18, pp. S15–S19, 2007.
- [87] A. Jäger-Waldau, “Thin film photovoltaics: Markets and industry,” *International Journal of Photoenergy*, vol. 2012, 2012.
- [88] M. Bazilian, I. Onyeji, M. Liebreich, I. MacGill, J. Chase, J. Shah, D. Gielen, D. Arent, D. Landfear, and S. Zhengrong, “Re-considering the economics of photovoltaic power,” *Renewable Energy*, vol. 53, pp. 329–338, 2013.
- [89] G. Nemet, “Interim monitoring of cost dynamics for publicly supported energy technologies,” *Energy Policy*, vol. 37, pp. 825–835, 2009.
- [90] J. McNerney, J. Farmer, S. Redner, and J. Trancik, “Role of design complexity in technology improvement,” *PNAS*, vol. 108, no. 22, pp. 9008–9013, 2011.
- [91] M. Bolinger and S. Weaver, “Utility-scale solar 2012: An empirical analysis of project cost, performance, and pricing trends in the united states,” Tech. Rep. LBNL-6408E, Lawrence Berkeley National Lab, 2013.
- [92] J. E. Trancik and K. Zweibel, “Technology choice and the cost reduction potential of photovoltaics,” in *Photovoltaic Energy Conversion, Conference Record of the 2006 IEEE 4th World Conference on*, vol. 2, pp. 2490–2493, 2006.
- [93] R. Bhandari and I. Stadler, “Grid parity analysis of solar photovoltaic systems in Germany using experience curves,” *Solar Energy*, vol. 83, pp. 1634–1644, 2009.
- [94] D. Poponi, “Analysis of diffusion paths for photovoltaic technology on experience curves,” *Solar Energy*, vol. 74, pp. 331–340, 2003.

- [95] B. van der Zwaan and A. Rabl, “Prospects for PV: a learning curve analysis,” *Solar Energy*, vol. 74, pp. 19–31, 2003.
- [96] J. Trancik, “Scale and innovation in the energy sector: a focus on photovoltaics and nuclear fission,” *Environmental Research Letters*, vol. 1, 2006.
- [97] L. Neij, “Use of experience curves to analyse the prospects for diffusion and adoption of renewable energy technology,” *Energy Policy*, vol. 23, no. 13, pp. 1099–1107, 1997.
- [98] G. J. Schaeffer, E. Alsema, A. Seebregts, L. Beurskens, H. de Moor, W. van Sark, M. Durstewitz, M. Perrin, P. Boulanger, and H. Laukamp, “Learning from the sun: Final report of the Photex project,” tech. rep., 2004.
- [99] L. Neij, “Cost development of future technologies for power generation: A study based on experience curves and complementary bottom-up assessments,” *Energy Policy*, vol. 36, pp. 2200–2211, 2008.
- [100] B. A. Sanden, “The economic and institutional rationale of PV subsidies,” *Solar Energy*, vol. 78, pp. 137–146, 2005.
- [101] B. van der Zwaan and A. Rabl, “The learning potential of photovoltaics: implications for energy policy,” *Energy Policy*, vol. 32, pp. 1545–1554, 2004.
- [102] T. E. Drennen, J. D. Erickson, and D. Chapman, “Solar power and climate change policy in developing countries,” *Energy Policy*, vol. 24, no. 1, pp. 9–16, 1996.
- [103] Z. Glasnovic and J. Margeta, “The features of sustainable solar hydroelectric power plant,” *Renewable Energy*, vol. 34, pp. 1742–1751, 2009.

- [104] TEPCO, “Kannagawa hydroelectric power station.” Press Release, June 7 2012.
- [105] R. H. Schulte, N. Critelli, K. Holst, and G. Huff, “Lessons from Iowa: Development of a 270 megawatt compressed air energy storage project in midwest independent system operator: A study for the doe energy storage systems program,” Tech. Rep. SAND2012-0388, Sandia, 2012.
- [106] W. M. Bishop, “The economic impact of CAES on wind in tx, ok, and nm,” tech. rep., Ridge Energy Storage & Grid Services L.P., 2005.
- [107] A. A. Akhil, “DOE/EPRI 2013 electricity storage handbook in collaboration with nreca,” report, Sandia National Laboratory, 2013.
- [108] B. Mehta, “CAES geology,” *EPRI Journal*, vol. 17:7, pp. 38–41, 1992.
- [109] B. Battke, T. S. Schmidt, D. Grosspietsch, and V. H. Hoffman, “A review and probabilistic model of lifecycle costs of stationary batteries in multiple applications,” *Renewable and Sustainable Energy Reviews*, vol. 25, pp. 240–250, 2013.
- [110] E. E. Storage tech. rep., February 2013.
- [111] ISCCP, “Satellite history data.” <http://isccp.giss.nasa.gov/docs/sathist.html#default>. Accessed: 201307-30.
- [112] W. B. Rossow and R. A. Schiffer, “Advances in understanding clouds from ISCCP,” *Bulletin of the American Meteorological Society*, vol. 80, no. 11, pp. 2261–2287, 1999.
- [113] G. Recktenwald, B. Stoll, and M. Deinert, “A fast open source code for determining the intensity and angular distribution of radiation transmitted through homogenous cloud cover,” *Solar Energy*, vol. 108, 2014.

- [114] NOAA Earth System Research Laboratory, “Solar calculation details,” 2013.
- [115] T. Dickey, T. Granata, J. Marra, C. Langdon, J. Wiggert, Z. Chai-Jochner, M. Hamilton, J. Vazquez, M. Stramska, R. Bidigare, and D. Siegel, “Seasonal variability of bio-optical and physical properties in the sargasso sea,” *Journal of Geophysical Research*, vol. 98, pp. 865–898, 1993.
- [116] A. J. Plueddemann, R. A. Weller, M. Stramska, and T. D. Dickey, “Vertical structure of the upper ocean during the marine light-mixed layers experiment,” *Journal of Geophysical Research*, vol. 100, pp. 6605–6619, 1995.
- [117] C. H. Whitlock, J. E. Hay, D. A. Robinson, S. K. Cox, D. I. Wardle, and S. R. LeCroy, “Downward shortwave surface irradiance from 17 sites for the FIRE/SRB wisconsin experiment from october 12 through november 2, 1986,” tech. rep., NASA, 1990.
- [118] WRMC-BSRN, “Basic radiation and other radiation measurements,” 2013.
- [119] NCDC, “Integrated surface data (isd),” June 2014 2014.
- [120] ASTM International, “Standard test methods for electrical performance of nonconcentrator terrestrial photovoltaic modules and arrays using reference cells,” 2012.
- [121] EIA, “Annual energy review 2011,” tech. rep., U.S. EIA., 2012.
- [122] A. Townsend, *A Grid-Level Assessment of Compressed Air Energy Storage in ERCOT*. PhD thesis, The University of Texas at Austin, May 2013.
- [123] J. Garrison, *A Grid-Level Unit Commitment Assessment of High Wind Penetration and Utilization of Compressed Air Energy Storage in ERCOT*. PhD thesis, The University of Texas at Austin, May 2015.

- [124] M. R. Hudec and M. P. A. Jackson, “Terra infirma: Understanding salt tectonics,” *Earth-Science Reviews*, vol. 82, pp. 1–28, 2007.
- [125] Bloomberg Finance, L.P., “Sustainable energy in america 2013 factbook,” tech. rep., Business Council for Sustainable Energy, 2013.
- [126] S. B. Darling, F. You, T. Veselka, and A. Velosa, “Assumptions and the levelized cost of energy for photovoltaics,” *Energy & Environmental Science*, vol. 4, pp. 3133–3139, 2011.
- [127] SAIC Energy, Environment & Infrastructure, LLC, “Updated capital cost estimates for utility scale electricity generating plants,” tech. rep., EIA, 2013.
- [128] M. Mendelsohn, T. Lowder, and B. Canavan, “Utility-scale concentrating solar power and photovoltaics projects: A technology and market overview,” Tech. Rep. NREL/TP-6A20-51137, National Renewable Energy Lab, 2012.
- [129] K. Branker, M. Pathak, and J. M. Pearce, “A review of solar photovoltaic levelized cost of electricity,” *Renewable and Sustainable Energy Reviews*, vol. 15, pp. 4470–4482, 2011.
- [130] J. Coughlin and K. Cory, “Solar photovoltaic financing: Residential sector development,” Tech. Rep. NREL/TP-6A2-44853, National Renewable Energy Laboratory, 2009.
- [131] A. Evans, V. Strezov, and T. Evans, “Assessment of utility energy storage options for increased renewable energy penetration,” *Renewable and Sustainable Energy Reviews*, vol. 16, pp. 441–4147, 2012.

- [132] M. Nakhamkin, M. Chiruvolu, M. Patel, and S. Byrd, “Second generation of CAES technology- performance, operations, economics, renewable load management, green energy,” in *POWER-GEN International Conference*, 8-10 December 2009.
- [133] S. M. Schoenung and W. V. Hassenzahl, “Long -vs. short-term energy storage technologies analysis,” Tech. Rep. Sand2003-2783, Sandia National Laboratories, August, 2003 2003.
- [134] EIA, “U.S. natural gas electric power price,” 2013.
- [135] European Commission, “Quarterly report on European gas markets, market observation for energy,” tech. rep., 2013.
- [136] International Gas Union, “Wholesale gas price survey - 2014 edition,” 2014.
- [137] U.S. DOE, “Grid energy storage,” tech. rep., U.S. Department of Energy, 2013.
- [138] IRS, “Yearly average currency exchange rates,” 04-Dec-2014.
- [139] First Solar, “Phase i, Mohammed bin Rashid Al Maktoum solar park project datasheet,” tech. rep., First Solar, 2013.
- [140] First Solar, “Blythe solar project datasheet,” tech. rep., First Solar, 2011.
- [141] First Solar, “Southern Company and Ted Turner energize cimarron solar facility,” 2011.
- [142] “Copper mountain solar 1,” 2012.
- [143] Sempra U.S. Gas & Power, “Copper mountain solar 2 fact sheet,” tech. rep., Sempra U.S. Gas & Power, 2013.



- [144] First Solar, “AV solar ranch 1 solar power plant achieves 100 mw milestone,” 2013.
- [145] Sempra U.S. Gas & Power, “Mesquite solar 1 fact sheet,” tech. rep., Sempra U.S. Gas & Power, 2013.
- [146] Newsroom, SunPower, “Nrg energy, nrg yield and sunpower begin commercial operations at 250 mw california valley solar ranch,” 2013.
- [147] First Solar, “World’s largest operational solar PV project, agua caliente, achieves 250 megawatts of grid-connected power,” 2012.
- [148] First Solar, “Topaz solar farm project datasheet,” tech. rep., First Solar, 2012.
- [149] First Solar, “Desert Sunlight solar farm project overview,” 2014.
- [150] S. Anolabehere, J. Deutch, J. Driscoll, P. E. Holdren, P. L. Joskow, R. K. Lester, E. J. Moniz, N. E. Todreas, and E. S. Beckjord, “The future of nuclear power,” technical report, MIT, 2003 2003.
- [151] P. L. Joskow, “Comparing the costs of intermittent and dispatchable electricity generating technologies,” *The American Economic Review*, vol. 101, pp. 238–241, 2011.
- [152] L. Hirth, “The market value of variable renewables, the effect of solar wind power variability on their relative price,” *Energy Economics*, vol. 38, pp. 218–236, 2013.
- [153] ERCOT, “Historical RTM load zone and hub prices.” <http://mis.ercot.com/misapp/GetReports.do?reportTypeId=13061&reportTitle=Historical%20RTM%20Load%20Zone%20and%20Hub%20Prices&showHTMLView=&mimicKey>. Accessed: Aug. 8, 2014.

- [154] MISO, “Market reports: Historical LMP.” <https://www.misoenergy.org/Library/MarketReports/Pages/MarketReports.aspx>. Accessed: Aug. 12, 2014.
- [155] N. Y. ISO, “Pricing reports: Energy.” <http://mis.nyiso.com/public/P-3Alist.htm>. Accessed: Aug. 8, 2014.
- [156] ISO New England, “Real-time commitment LBMP - zonal.” <http://www.iso-ne.com/isoexpress/web/reports/pricing?category=Hourly>. Accessed: Aug. 9, 2014.
- [157] SPP, “SPP documents & filings: Historical LIP data.” <http://www.spp.org/section.asp?group=1524&pageID=27>. Accessed: Aug. 11, 2014.
- [158] PJM, “Data miner: Locational marginal pricing.” <https://dataminer.pjm.com/dataminerui/pages/public/lmp.jsf>. Accessed: Aug. 12, 2014.
- [159] The Texas Office of Public Utility Council, “ISO/RTO regions.” <http://www.opuc.texas.gov/ercot.html>.
- [160] LCG Consulting, “Industry data: CAISO actual load.” [http://www.energyonline.com/Data/GenericData.aspx?DataId=18&CAISO\\_\\_\\_Actual\\_Load](http://www.energyonline.com/Data/GenericData.aspx?DataId=18&CAISO___Actual_Load). Accessed: March 2, 2015.
- [161] ERCOT, “Hourly load data archives.” [http://www.ercot.com/gridinfo/load/load\\_hist/](http://www.ercot.com/gridinfo/load/load_hist/). Accessed: Dec. 9, 2014.
- [162] ISO New England, “Hourly real-time system demand.” <http://www.iso-ne.com/isoexpress/web/reports/load-and-demand>. Accessed: Dec. 9, 2014.
- [163] MISO, “Market reports: Historical regional forecast and actual load.” <https://www.misoenergy.org/Library/MarketReports/Pages/MarketReports.aspx>. Accessed: Jan. 21, 2014.

- [164] N. Y. ISO, “Real-time actual load.” <http://mis.nyiso.com/public/P-58Blist.htm>. Accessed: Dec. 9, 2014.
- [165] PJM, “Estimated hourly load.” <http://www.pjm.com/markets-and-operations/energy/real-time/loadhryr.aspx>. Accessed: Dec. 9, 2014.
- [166] SPP, “SPP load forecast.” <http://www.spp.org/LoadForecast/>. Accessed: Dec. 9, 2014.
- [167] O. A. Omitaomu, B. R. Blevins, W. C. Lochem, G. T. Mays, R. Belles, S. Hadley, T. J. Harrison, B. L. Bhaduri, B. S. Neish, and A. N. Rose, “Adapting a GIS-based multicriteria decision analysis approach for evaluating new power generating sites,” *Applied Energy*, vol. 96, pp. 292–301, 2012.
- [168] K. Tisza, S. Brame, and A. Anctil, “GIS based analysis for photovoltaic deployment in the southeast us,” in *Photovoltaic Specialist Conference (PVSC), 2014 IEEE 40th*, pp. 1001–1004, 8-13 June 2014.
- [169] S. J. Carver, “Integrating multi-criteria evaluation with geographical information systems,” *International Journal of Geographical Information Systems*, vol. 5, pp. 321–339, 1991.
- [170] J. Malczewski, “GIS-based multicriteria decision analysis: a survey of the literature,” *International Journal of Geographical Information Science*, vol. 20, pp. 703–726, 2006.
- [171] E. A. Grubert, A. S. Stillwell, and M. E. Webber, “Where does solar-aided seawater desalination make sense? A method for identifying sustainable sites,” *Desalination*, vol. 339, pp. 10–17, 2014.

- [172] M. Phua and M. Minowa, "A GIS-based multi-criteria decision making approach to forest conservation planning at a landscape scale: a case study in the Kinabalu Area, Sabah, Malaysia," *Landscape and Urban Planning*, vol. 71, pp. 207–222, 2005.
- [173] G. A. Kiker, T. S. Bridges, A. Varghese, T. P. Seager, and I. Linkov, "Application of multicriteria decision analysis in environmental decision making," *Integrated Environmental Assessment and Management*, vol. 1, pp. 95–108, 2005.
- [174] J. Wang, Y. Jing, C. Zhang, and J. Zhao, "Review on multi-criteria decision analysis aid in sustainable energy decision-making," *Renewable and Sustainable Energy Reviews*, vol. 13, pp. 2263–2278, 2009.
- [175] F. Joerin, "Using GIS and outranking multicriteria analysis for land-use suitability assessment," *International Journal of Geographical Information Science*, vol. 15, pp. 153–174, 2001.
- [176] World Bank Group, "Global economic prospects, vol. 9," tech. rep., World Bank Group, 2014.
- [177] C. Kirubi, A. Jacobson, D. M. Kammen, and A. Mills, "Community-based electric micro-grids can contribute to rural development: Evidence from Kenya," *World Development*, vol. 37, pp. 1208–1221, 2009.
- [178] A. Chaurey, M. Ranganathan, and P. Mohanty, "Electricity access for geographically disadvantaged rural communities - technology and policy insights," *Energy Policy*, vol. 32, pp. 1693–1705, 2004.
- [179] M. Kanagawa and T. Nakata, "Assessment of access to electricity and the socio-economic impacts in rural areas of developing countries," *Energy Policy*,

- vol. 36, pp. 2016–2029, 2008.
- [180] A. Lopez, B. Roberts, D. Heimiller, N. Blair, and G. Porro, “U.s. renewable energy technical potentials: A GIS-based analysis,” Tech. Rep. NREL/TP-6A20-51946, NREL, July 2012.
- [181] A. Jarvis, H. Reuter, A. Nelson, and E. Guevara, “Hole-filled SRTM for the globe version 4.” <http://srtm.csi.cgiar.org>, 2008. Available from the CGIAR-CSI SRTM 90m Database.
- [182] WWF, “Global lakes and wetlands database: Lakes and wetlands grid (level 3),” 2004.
- [183] B. Lehner and P. Doll, “Development and validation of a global database of lakes, reservoirs and wetlands,” *Journal of Hydrology*, vol. 296, pp. 1–22, 2004.
- [184] Center for International Earth Science Information Network - CIESIN - Columbia University and International Food Policy Research Institute - IFPRI and The World Bank and Centro Internacional de Agricultura Tropical - CIAT, “Global rural-urban mapping project, version 1 (grumpv1): Population density grid,” 2011.
- [185] Center for International Earth Science Information Network - CIESIN - Columbia University and International Food Policy Research Institute - IFPRI and The World Bank and Centro Internacional de Agricultura Tropical - CIAT, “Global rural-urban mapping project, version 1 (grumpv1): Population count grid,” 2011.
- [186] World Bank Group, “Electric power consumption (kwh per capita).” <http://data.worldbank.org/indicator/EG.USE.ELEC.KH.PC>. Accessed: Aug. 5,

- 2014.
- [187] World Bank Group, “World development indicators: Population total.” <http://databank.worldbank.org/data/views/reports/tableview.aspx>. Accessed: Feb. 25, 2015.
- [188] World Bank Group, “Health nutrition and population statistics: Population estimates and projections.” <http://data.worldbank.org/data-catalog/population-projection-tables>. Accessed: Feb. 24, 2015.
- [189] World Bank Group, “World development indicators: Access to electricity (population).” <http://data.worldbank.org/indicator/EG.ELC.ACCS.ZS/countries?display=default>. Accessed: March 1, 2015.
- [190] OSGeo Project, “GRASS GIS 7.0.0.” <http://grass.osgeo.org/>, 2015.
- [191] Center for International Earth Science Information Network - CIESIN - Columbia University and International Food Policy Research Institute - IFPRI and The World Bank and Centro Internacional de Agricultura Tropical - CIAT, “Global rural-urban mapping project, version 1 (grumpv1): National identifier grid, v1,” 2011.

# Vita

Brady Leigh Stoll was born in Dallas, Texas. After moving to Austin, Texas, she graduated from Dripping Springs High School and in 2006 entered the University of Texas at Austin as an undergraduate. She received the degrees of Bachelor of Science in Physics and Bachelor of the Arts in Plan II in 2010. Upon graduation she continued her education by re-entering the University of Texas at Austin as a graduate student in Mechanical Engineering. She earned her Master of Science in Engineering in 2012 and continued her work at UT during her Ph.D.

Permanent address: 705 Oakwood ln  
Dripping Springs, Texas 78620

This dissertation was typeset with L<sup>A</sup>T<sub>E</sub>X<sup>†</sup> by the author.

---

<sup>†</sup>L<sup>A</sup>T<sub>E</sub>X is a document preparation system developed by Leslie Lamport as a special version of Donald Knuth's T<sub>E</sub>X Program.